NEUTRINO FLAVOR SIGNATURES IN IN-ICE RADIO DETECTORS

Master's Thesis in Physics

Presented by

Janna Zoe Vischer

July 27, 2023

Erlangen Center for Astroparticle Physics
Friedrich-Alexander-Universität Erlangen-Nürnberg

Supervisor: Prof. Dr. Anna Nelles

Contents

Chapter 1

Introduction

High energetic (HE) astrophysical neutrinos with energies from TeV to 100 PeV and ultra-high energetic (UHE) neutrinos above 100 PeV are excellent probes to discover the fundamental mechanisms of our universe [1]. They play a leading role in addressing urgent issues in both particle and astrophysics: To further study the fundamental properties of high and ultra-high energy neutrinos, astrophysical neutrinos have to be investigated since neutrinos of such energies cannot be artificially produced in accelerators. However, rare naturally occurring UHE neutrinos from space can be used to address beyond standard model subjects like neutrino self-interaction, interactions with or production by dark matter or the question whether neutrinos are stable [2].

Neutrinos play a key role in multi-messenger astronomy, since they can traverse large distances undisturbed and thus follow a direct path from their sources. When they are created in the same environments as cosmic rays, they provide further information about the acceleration mechanisms of cosmic rays in the universe. Since UHE cosmic rays interact with the cosmic microwave background their energy is limited by the GZK cut-off. During this process neutrinos are created that can be used to study the behaviour of cosmic rays indirectly [3]. Possible origins are gamma ray bursts or active galactic nuclei, where matter is accreted around a supermassive black hole [4]. Recently, the first such neutrino was detected by the IceCube experiment from the blazar TXS 0506+056 [5]. The diffuse cosmic neutrino flux has been measured by IceCube up to PeV [6] but a possible cut-off energy has not been determined yet.

Neutrinos come in three flavors, which are subject to oscillation during propagation. The determination of the astrophysical neutrino flavor composition is thus of high interest to test neutrino oscillations at highest energies [4]. From the flavor composition of astrophysical neutrinos the production mechanisms of neutrinos and cosmic rays can be deduced [7].

The detection of the small flux of high energetic and ultra-high energetic neutrinos will become possible by the next generation of neutrino radio detectors. As a detection medium ice is used due to its large density, transmissivity of radio waves and abundance in the polar regions of the Earth. Neutrino induced particle showers emit radio waves via the Askaryan effect, which can be measured by antennas buried in ice. This method has the advantage of being affordable due to cost-effective detector parts and station spacing. While the precursor experiments ARA [8] and ARIANNA [9] were not able to detect any cosmic neutrinos yet, larger detector arrays are being built combining the technical ap-

proaches of the two. The Radio Neutrino Observatory in Greenland (RNO-G) is currently under construction, with seven out of 35 stations built [10]. As a part of the IceCube-Gen2 project at the South Pole a radio component is planned to complement the optical part of the detector using several hundred cubic kilometers of ice as a detection medium [11].

In this thesis the signatures of different neutrino flavors in radio neutrino detectors are studied with respect to their primary interaction, energy and incoming inclination. This is done by exploiting the characteristics of their secondary showers and particles. The theoretical aspects of neutrino interactions in ice and the operating principles are introduced in chapter 2. The study was performed on Monte Carlo simulated events using a simplified RNO-G station as detector setup. The event production is explained in chapter 3. With these simulations general observations are made considering the energy distribution of the created showers, the number of showers per initial neutrino interaction and the spatial detectability of the showers by the detector in chapter 4. These findings are then used to create a classification of muon neutrino events in those created by a charged current and neutral current interaction. To achieve such a separation of events two approaches are developed and assessed: The first approach developed in chapter 5 is based on the number of showers detected by a single detector station. Eight strategies to optimize the performance of the separation are designed and applied on the simulated events. Their performance of separating muon neutrinos created by charged current events from neutral current events is evaluated in chapter 6. The universality of these developed strategies is investigated for varied neutrino energies and inclinations. The feasibility to use this approach to separate muon neutrinos from electron neutrinos and tau neutrinos is surveyed. Additionally, the influence of thermal noise induced by the ambient temperature and electronics on the detected traces is investigated in a first approach. In a second attempt, in chapter 7, the multiplicity of triggered stations from multiple showers is used to select muon neutrinos from charged current interactions from neutral current ones. For this, simulations of a proposed IceCube-Gen2 Radio detector array are used. Finally, the results are summarized and evaluated in chapter 8.

Chapter 2

Theory

2.1 Astrophysical Neutrinos

The existence of the neutrino as an elementary particle was first postulated in 1930 by Pauli, due to missing energy in the electron spectrum of β-decay. Only 26 years later, in 1956 the first experimental evidence of neutrinos was discovered by Reines and Cowan utilizing the inverse β-decay. Their discovery was awarded the Nobel Prize in physics in 1995 [12, p.9 ff.]. Neutrinos are fermions and come in three flavors, one for each particle generation. They are named after the electrically charged lepton in their generation: electron neutrino ν_e, muon neutrino ν_μ and tau neutrino ν_τ. Since they neither interact strongly nor electromagnetically, they form the group of electrically neutral leptons. They are the lightest fermions. In fact, their mass is so small, that is has not yet been determined and only upper limits can be given [13]. Besides the immeasurable gravitational effects, neutrinos only participate in weak interactions. This makes them perfect messenger particles in astroparticle physics, since they are neither bent by magnetic fields like cosmic rays nor substantially attenuated due to interstellar matter when they propagate through the universe. On the downside the detection of neutrinos is rather difficult. Since they only interact weakly they can not be measured directly but only via the secondary particles produced in electromagnetic interactions that are created after the first weak interaction.

The flux of neutrinos reaching Earth decreases drastically with their energy. Figure 2.1 shows the spectrum of different neutrino sources. The neutrinos of lowest energies stem from the cosmic neutrino background. Neutrinos with higher energies stem from the fusion processes in the sun and from decays in the Earth's surface known as terrestrial neutrinos. Reactor neutrinos are factitious anti-neutrinos created by fission in nuclear reactors. Neutrinos from outside of the solar system, can be produced by supernovae. The lower line is the usual background from supernovae, the upper line is the flux that has been detected for a short time during the supernova burst of SN1987 A [14]. Cosmic rays interacting in the atmosphere produce particle showers as explained in the following section. When a π^+ decays into a muon an additional anti-muon neutrino is produced and vice versa for a π^-. The unstable muon decays into an electron accompanied by a muon-neutrino and anti-electron neutrino. The neutrinos produced on these processes are called atmospheric neutrinos. Neutrinos from active galactic nuclei (AGN) cover energies from 10^9 eV to 10^{17} eV. AGNs are some of the brightest sources in the universe, where matter accumulates around a black hole and gets accelerated. Two jets on opposite sides of the

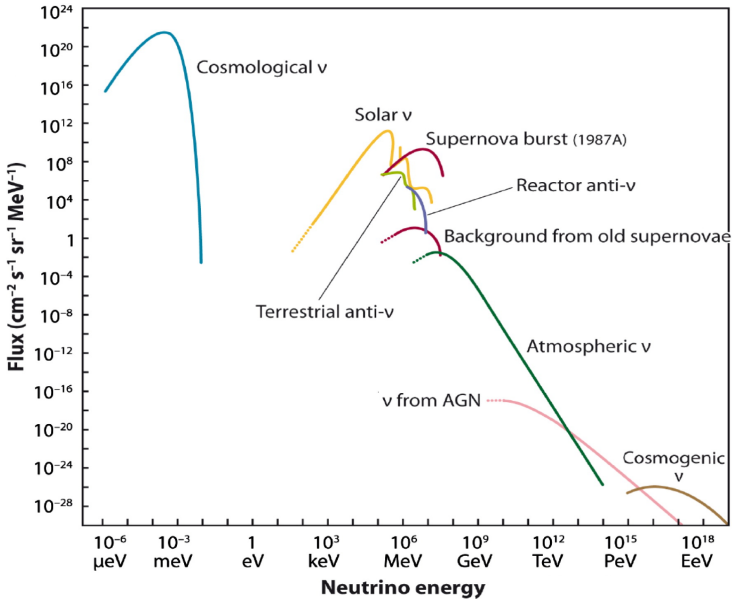

Figure 2.1: Neutrino Spectrum: On the x-axis the neutrino energy is shown and on the y-axis the flux, both on a logarithmic scale. Each line indicates the neutrino spectrum from a certain neutrino source. Figure from [17].

black hole emit the accelerated particles. High energetic protons and photons interact and produce pions in a process called photoproduction. These pions decay and thereby emit neutrinos [15]. Neutrinos with highest known energies are cosmogenic neutrinos, produced due to the cosmic rays interacting with the cosmic microwave background. This leads to a cut off of cosmic rays at high energies called GZK cut-off after Greisen, Zatsepin and Kuz'min. This interaction has a resonance at the energy of the Delta baryon, which leads to its production. The Delta barion is unstable and decays mainly into a pion and nucleon. By the decay of a charged pion high energetic neutrinos can be produced [13] [16] [15]. These neutrinos are very rare. Unlike Figure 2.1 is indicating, the neutrino flux at these scales is not yet determined.

There are two ways a neutrino ν_l with the flavor l can interact with a nucleon N, as shown in Figure 2.2. If the exchange particle between the neutrino and the nucleon is an electrically neutral Z boson, the interaction is called 'neutral current interaction' (NC). The corresponding Feynman diagram is depicted in Figure 2.2a. The outgoing particle is again an invisible neutrino of the same flavor accompanied by an outgoing hadronic cascade, indicated in red. In the case of a 'charged current interaction' (CC), the neutrino interacts with the nucleus by exchanging a W boson, shown in Figure 2.2b. In the case of normal-matter neutrinos, a normal-matter lepton of the same flavor as the neutrino, depicted in blue, is created additionally to the hadronic cascade in red. In the case of an antimatter neutrino, the lepton is the complementary anti-lepton. In the following the term neutrino refers to both neutrinos and anti neutrinos.

At high energies the cross-section σ of neutrinos with nucleons follows a power law. It can be approximated with

$$\sigma_{\nu N}^{CC} = 5.53 \cdot 10^{-36}\,\mathrm{cm}^2 \left(\frac{E_\nu}{1\,\mathrm{GeV}}\right)^{0.363} \tag{2.1}$$

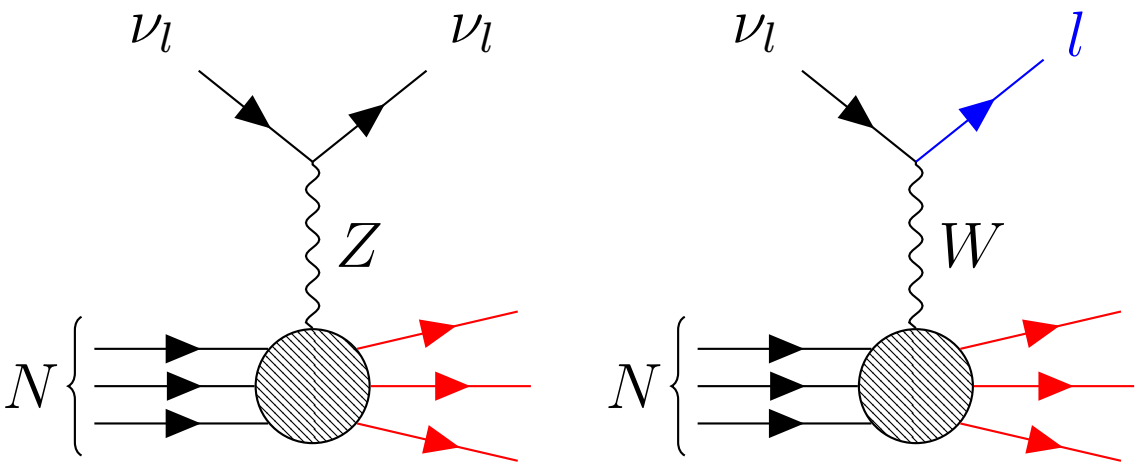

(a) (b)

Figure 2.2: A neutrino ν_l interacting with a nucleus N: Figure 2.2a shows the neutral current (NC) interaction with a Z boson as the messenger particle. Thereby another neutrino and a hadronic shower is emitted, indicated by three red lines. Figure 2.2b shows the charged current interaction (CC) via a W boson. Thereby a lepton l (blue) is created as well as another hadronic shower.

for CC interactions and with

$$\sigma_{\nu N}^{NC} = 2.31 \cdot 10^{-36}\,\mathrm{cm}^2 \left(\frac{E_\nu}{1\,\mathrm{GeV}}\right)^{0.363} \tag{2.2}$$

for NC interactions [18, eq.90, 91]. Except for energies around the Glashow resonance at 6.3 PeV, where W bosons are created, neutrino nucleon cross-sections are in general of orders of magnitudes larger than neutrino electron cross-sections [18]. In the scope of this thesis, neutrinos of energies between 10^{16} eV to 10^{19} eV are investigated, thus neutrino-electron interactions are not examined.

2.2 Properties of Secondary Leptons and Showers

The hadronic cascade and in the case of CC interaction the outgoing lepton are the starting points of the particle showers induced by the interacting neutrino: After the weak interaction the energy transferred to the nucleon induces QCD processes spawning hadrons. This hadronic cascade mostly consists of pions. π^0-mesons have a short lifetime and mostly decay into two photons [13]. $\pi^\pm$-mesons live longer and, in case of sufficient energy, can produce further pions while interacting with particles of the detection medium. Resulting $\pi^\pm$ possess less energy and at some point, they do not interact further and decay into muons and neutrinos. The produced π^0-mesons, decay further into photons. Since the created photons are high energetic, they produce electrons and positrons via pair production. These charged particles in turn emit photons via bremsstrahlung which again partake in pair production and so on. An electromagnetic particle shower emerges. Further pair production is not possible anymore, if the energy of the photon is not sufficient to create the mass of the electron and positron. Bremsstrahlung ceases at lower energies and is dominated by energy loss through ionization and excitation below a medium dependent critical energy [19]. The energy of the initial photon is hence spread

to some degree evenly over the sub particles. These electromagnetic sub-showers, which mostly consist of photons, electrons and positrons contain the majority of the energy of the initial hadronic cascade.

In the case of a CC interaction the outgoing lepton can produce additional showers. An interacting electron neutrino produces an electron, which receives a large fraction of the initial neutrino energy. The electron produces a pure electromagnetic particle shower via bremsstrahlung and pair production. Usually this electromagnetic shower is produced instantly. For high energetic electrons the start of the electromagnetic shower is delayed by the LPM effect: during a bremsstrahlung process, the electron is deflected by the nucleus of an atom in the atmosphere, emitting a photon. An additional virtual photon is exchanges between the electron and the nucleus. The momentum transfer in the direction of flight $q_{\parallel}$ of the electron is small and proportional to $\frac{E_\gamma}{E_e(E_e-E_\gamma)}$, where E_γ is the photon energy and E_e the electron energy. By the uncertainty principle, the distance over which this process takes place, called formation length L_f becomes larger and scales inversely: $L_f \approx \frac{E_e(E_e-E_\gamma)}{E_\gamma}$. For the bremsstrahlung process to happen, the electron needs to be undisturbed over this distance. If the electrons energy is high enough, such that the formation length spans over several atoms, additional interactions disturb the bremsstrahlung process and reduce the cross-section [20] [21]. Thus, the distance an electron travels before interacting is increased and several spatially displaced electromagnetic showers are created.

If a muon neutrino interacts via a CC interaction a muon is produced additionally to the hadronic cascade. Although muons are unstable particles and will decay further their lifetime is long on the scale of elementary processes. Additionally, high energetic muons are subject to relativistic effects and due to time dilation they live even longer in the reference frame of a resting observer. This allows them to travel a long distance of several kilometer before decaying and escaping the field of view of a detector. However, before decaying a high energetic muon looses some of its energy along its path of flight due to bremsstrahlung and photo nuclear interactions as well as electron pair production at highest energies [22] [23]. These energy losses induce further particle showers. At highest energies the LPM effect has to be considered for muons as well.

Concluding, a tau lepton will be produced if a tau neutrino interacts via a CC interaction. At high energies some of the energy loss is due to bremsstrahlung. The pair production along its path might also be energetic enough to create an electromagnetic showers [23]. Depending on its energy a high energy tau (e.g. $10^{16}\,\mathrm{eV}$) or ultra-high energy tau (e.g $10^{19}\,\mathrm{eV}$) can travel an average distance of a few hundred to few tens of kilometers through ice before decaying [4].

2.3 Radio Emission from Particle Showers

One way to successfully measure neutrinos is to use the so called Askaryan-effect: The produced particle showers are dominated by an electromagnetic component, which mainly consists of electrons, positrons and photons. When these particles propagate through a dense medium, the positrons annihilate with electrons in the medium. The ionized atoms are inert and stay behind the forward expanding shower and now negatively charged

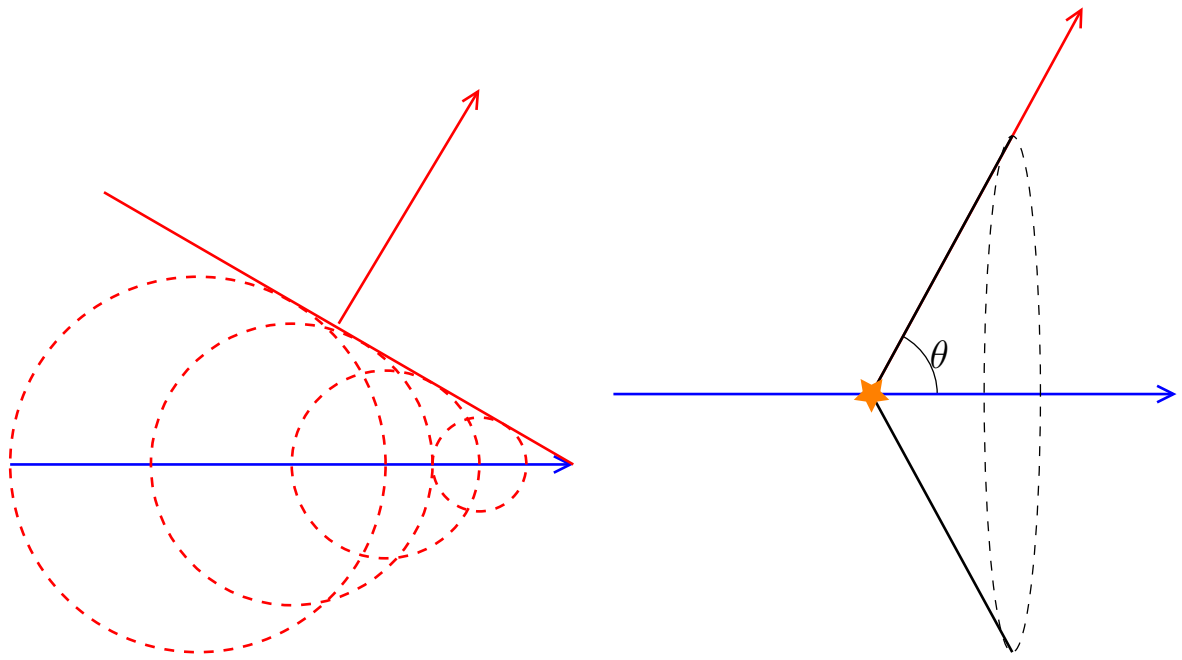

(a) (b)

Figure 2.3: Radio Emission of a particle shower (blue) in ice: Figure 2.3a shows a particle shower developing in horizontal direction. At each point along it way a radio wave (dashed red) is emitted uniformly, propagating slower that the shower itself. Along the radio wave front (red line) the emitted radio waves are coherent. With time the radio wave front propagates in the direction of the red arrow. Figure 2.3b shows the situation observed from afar, the shower is indicated by the orange star. The propagation direction of the radio wave front (red arrow) forms the Cherenkov angle θ with the propagation direction of the shower (blue arrow). The radio emission is rotationally symmetric around the shower axis forming the Cherenkov cone (black).

shower front. Additionally, in ice, the produced photons add electrons by ionizing atoms through Compton scattering and the photoelectric effect [24]. This time-varying separation of charge along the shower axis leads to the emission of a radio pulse. For the creation and further propagation of the radio pulse the medium needs to be a dielectric such as ice, which will be considered in the following as the interaction and propagation medium. The particles in the shower possess enough energy, that their velocity can be approximated with the speed of light in vacuum c. The propagation direction of a shower is shown in Figure 2.3a as a blue arrow. Along its path the shower emits radio signals. The propagation speed of the radio signal is limited by the index of refraction n of the ice and thus slower than the shower. In a snapshot, the emitted radio signals move away concentrically from their emission point and their maximum is located on the dashed circle. On the tangent across all these maxima, shown in red the radio signal is coherent. Over time this radio signal front propagates in the direction of the red arrow. The angle between the red and blue arrow is called the Cherenkov angle.

The length of a particle shower depends on its type and energy: While the elongation of a hadronic shower lies in the order of twenty meter in the relevant energy ranges, electromagnetic showers are more elongated due to the LPM effect and can span to up to 150 m at energies of 10 EeV [4, fig.5]. From further away, a shower can be approximated to be point-like. It is indicated by the yellow star in Figure 2.3b. The coherent radio

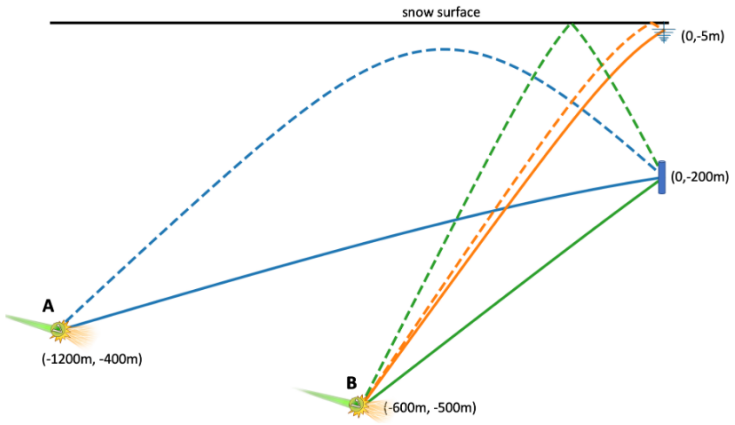

Figure 2.4: Possible radio ray paths from the point of interaction (A and B) to a Surface antenna or deep component antenna in ice with increasing density. Each interaction can arrive at an antenna via a direct path (solid lines) or an indirect path (dashed lines). An indirect path can be bend by the varying refraction index of the ice (blue dashed line) or by being reflected at the firn-air transition (dashed orange and green line). Figure from [4].

signal is emitted over all angles around the shower axis. This establishes the Cherenkov cone, shown in black, around the shower axis with the Cherenkov angle θ as the apex angle on which the amplitude of the signal is maximal. On this cone the Askaryan radio emission has the form of a narrow bipolar pulse and a duration of less than a ns. The wavelengths lie between 1 cm to 100 cm [24]. Deviations from the Cherenkov angle by only a few degrees, where the radio waves are not coherent anymore, prolong the radio pulse and reduce the amplitude since the waves no longer arrive simultaneously. This also leads to an elimination of higher frequencies in the radio spectrum [4].

2.4 Radio Waves in Ice

Ice is a unique detector material. It has a high mass density, which increases the neutrino cross-section. For the same reason other experiments like ANTARES [25], KM3NeT [26] or P-ONE [27] use water as an interaction medium for optical neutrino measurements. Additionally, water is abundantly available in the ocean and transparent to visible light in the Cherenkov spectrum. However, to exploit the Askaryan effect the material not only needs to be a dielectric, but also needs to be transparent to the created radio waves. In liquid water the molecules are free to align with the electric field shielding the radio wave. In ice, this cannot happen. An abundant amount of several cubic kilometers pure ice is available in Greenland and at the Antarctic in radio-quiet regions.

When a radio wave propagates through the ice sheet it gets attenuated. The attenuation length, i.e the distance over which the signal amplitude is reduced to $\frac{1}{e}$, is dependent on the chemical composition of the ice and its temperature. The warmer the ice, the less transparent it is to radio waves. Since the temperature increases with depth, the attenuation length decreases. The attenuation also increases for low frequencies. The Greenland ice sheet has an attenuation length of about 1 km [4]. This allows for a sparse spacing of detectors, reducing costs. The density of the ice is also depth dependent: New snow falls on the granular firn ice and compresses it with its weight. The firn gets therefore

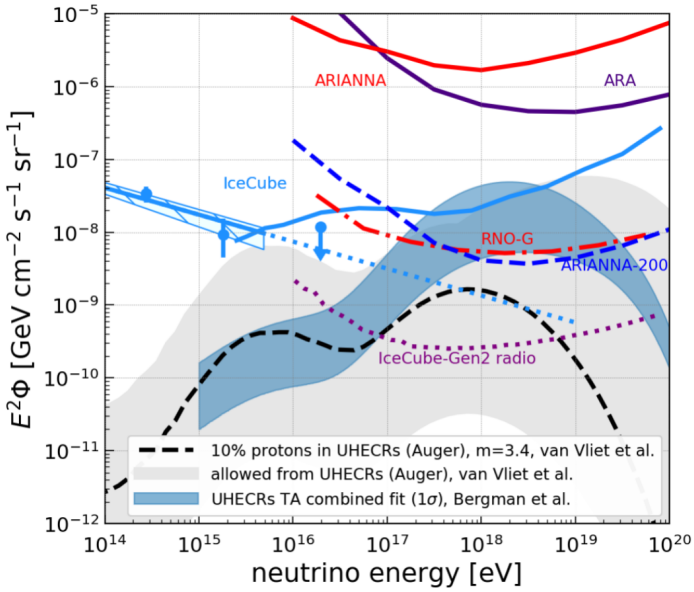

Figure 2.5: Neutrino flux on the y-axis in dependence of the neutrino energy. The sensitivity of IceCube is shown in light blue. The expected sensitivities of the radio neutrino experiments ARIANNA, ARA and the planned experiments RNO-G and IceCube-Gen2 Radio are sensitive to higher neutrino energies. The expected high energetic neutrino flux is estimated from the GZK cut-off of measured cosmic rays. These measurements stem from the Auger experiment (gray and black dashed line) and the Telescope Array (TA) (light blue band). Figure from [30]

slowly compressed into clear ice. The change of the density in the upper layers results in a change of the refractive index. Measurements in the antarctic ice sheet leads to a refraction index of about 1.3 and converges to values of 1.74 at depths below 150 m. A radio wave propagating upwards therefore follows a bend over path and is bend downwards as shown in Figure 2.4. Additionally, a radio wave that is not bend downwards, will reflect off the firn-air transition. In consequence a radio wave has two possible paths to arrive at a detector: the direct path and an indirect (bent-over or reflected) path. Below the 3 km thick Greenlandic ice sheet a non-reflective layer of bedrock is situated [10].

2.5 Detectors for Radio Emission of Neutrinos

The cross-section of neutrinos with nucleons increases with their energy. Thus, the mean distance of travel before interaction decreases. While a neutrino with an energy of 10^{17} eV has a mean free path of 2693 km in ice a neutrino with a neutrino energy of 10^{19} eV only has a mean free path of 581 km [4]. For an isotropic flux, the mean path of passing through Earth is $8.11 \cdot 10^3$ km, considering the inclination dependent path length and Earth's radius of 6371 km [28]. Additionally the mean density of the Earth is about five times larger than ice [29], further reducing the mean distance of travel of a neutrino. Thus, the Earth is opaque to ultra high energetic neutrinos. The influence of the atmosphere to neutrinos is small for vertically arriving neutrinos, since it is not very thick and not very dense. Only the number of shallowly arriving neutrinos is slightly decreased. Therefore Radio Neutrino Detectors detect neutrinos coming from above.

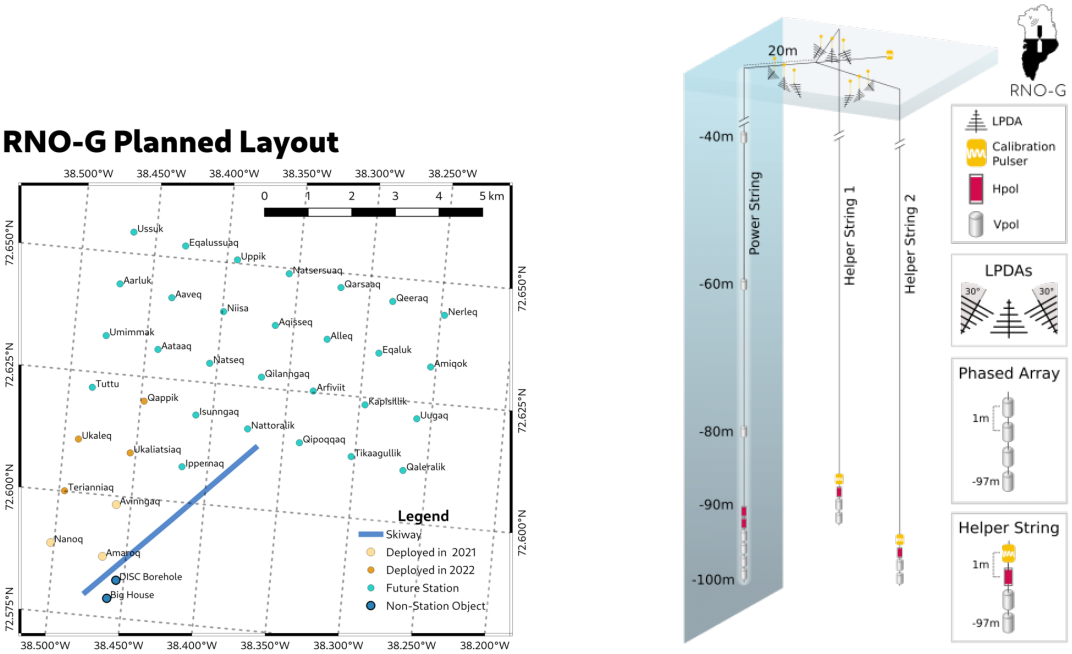

(a) (b)

Figure 2.6: RNO-G station layout: Figure 2.6a shows the layout of the 35 stations at Summit Station. The color of the station indicates the year of deployment, if already deployed. Figure 2.6b shows the schematics of a single RNO-G station, consisting of three sets of three LPDAs in the surface component and three strings equipped with Calibration Pulsers (yellow), Hpol (red) and Vpol antennas (gray). Figure from [31].

Despite several efforts so far no neutrino interaction has been detected via the Askaryan effect. Figure 2.5 shows the measurable neutrino flux of the optical neutrino detector IceCube as well as the limits from previous radio neutrino experiments and the expected measurable flux of the partly deployed Radio Neutrino Observatory Greenland (RNO-G) and the radio detector part of the planned neutrino detector expansion at the South Pole IceCube-Gen2 Radio. Both detectors will be able to decrease the lower limit of the measurable flux. While IceCube-Gen2 Radio leads to an improvement of another order of magnitude, both experiments are complementary due to their location on opposite hemispheres and covering different parts of the sky. The expected neutrino flux have been calculated from the cosmic ray fluxes measured by the Auger experiment (gray band) or the Telescope Array (blue band) and the expected interaction with the CMB.

The Radio Neutrino Observatory Greenland (RNO-G) is currently being build at Summit Station in Greenland. Its layout is a combination of proven antenna designs from ARIANNA and ARA and increased in size. The deployment started in 2021 and will consist of 35 stations 1.25 km apart in its final form. The spacing is maximized to optimize the total detection volume. Thus, each shower is usually only detected in one station. The layout of the stations is shown in Figure 2.6a where the color of the station indicates its year of deployment.

Each station consists of several antennas. The station layout is shown in Figure 2.6b. In the center a data acquisition box (DAQ-Box) is positioned together with communication antennas and solar panels for autonomous operation [32]. Two stations additionally are equipped with wind turbines as power generators [33]. The surface component of

RNO-G consists of three by three log-periodic dipole antennas (LPDA). At a distance of 11 m from the station center, they are buried about 2 m deep [32]. The three sets of three LPDAs each are arranged in a triangle around the center of the station. The three LPDAs of one set are rotated 120° against each other to be sensitive to all arriving polarizations of radio waves. Due to their large size, they do not fit in boreholes and therefore need to be buried manually. They are sensitive to a broad frequency range and can be used not only to detect showers in the ice, but also to veto and analyze cosmic-ray air showers [4].

The deep component of a station consists of three strings, on which several antennas are attached. Vertically polarized antennas (Vpol) are fat dipole design antennas. Due to their diameter of 12.7 cm, they fit into the borehole. Their response is rotationally symmetric around the cable. They are sensitive between 50 MHz and 600 MHz [32]. Additionally horizontally polarized antennas (Hpol) are used with a quadslot antenna design. Their performance is limited by the size of the borehole resulting in a diameter of 20.32 cm and a sensitivity range between 200 MHz and 400 MHz. The power string consists of four Vpol antennas in a depth of up to 100 m, which are used as a trigger [34]. The measured traces of these four antennas are added, resulting in signals to add up and noise to average out. The two above Hpol antennas are used for polarization reconstruction. Three additional Vpol antennas are placed at larger distances above. Two helper strings consist of two Vpol antennas and one Hpol antenna as well as a Calibration Pulser, which will be used for calibration [32].

With this setup RNO-G aims to measure neutrinos in an energy range of several PeV. One expects a neutrino event rate of neutrinos with energies above 10^{16} eV of several per decade [10].

Due to its location and functionality RNO-G will cover large parts of the northern hemisphere [4]. To complement these efforts, an expansion for the optical neutrino detector IceCube located at the South Pole is proposed. It includes a radio array targeting neutrinos, IceCube-Gen2 Radio. The setup is not finalized yet. It covers an area of about 500 km^2. While RNO-G consists of one type of stations, at IceCube-Gen2 Radio two types of stations are proposed to be used: shallow stations and hybrid stations. Hybrid stations involve several LPDAs close to the surface and three strings of Calibration Pulsers, Hpol and Vpol antennas. They are deployed to depths of up to 150 m [11]. The hybrid stations have a spacing of a few km. In between, shallow stations, consisting of LPDA antennas and Vpol antennas in depths of around 10 m are placed. Since the attenuation length of radio waves in the upper ice layers is shorter, additional shallow stations fill blind gaps. IceCube-Gen2 Radio will be sensitive to neutrinos with energies above $3 \cdot 10^{16}$ eV [35].

Chapter 3

Simulating Neutrinos

RNO-G is still in development and does not provide sufficient data to detect neutrinos yet. Also the flavor of a measured neutrino is naturally not known. Thus, simulations of neutrinos with fixed properties like flavor and energy are needed. The involved physics behind a neutrino interacting in ice, creating radio signals, which propagate on bent paths through ice and finally the detection and recording in an antenna have been implemented in NuRadio (Version 2.1.7). It contains the package NuRadioMC for Monte Carlo simulated events for a variety of antenna types, detection media and customizable detector layouts [36]. The package NuRadioReco can be used for the reconstruction of signals in a detector [37]. For the simulation of neutrino events in ice the package PROPOSAL (Version 7.4.2) is used by NuRadioMC to propagate secondary muons and taus [38].

3.1 Neutrino Induced Particle Showers in Ice

In a fist step neutrinos interacting in the ice are simulated. These simulations were computed on the woody cluster provided by the Erlangen National High Performance Computing Center. To do so, a shell script was used for job submission. It specifies the job parameters and the input parameters for the simulation such as the neutrino flavor, energy and the minimum zenith inclination angle of the simulated neutrinos. The angle is given in $\cos\theta$, where θ is the inclination angle of a value between 0 rad and π rad. Therefore $\cos(\theta)$ can take on values between -1 and 1, where an inclination of 0 is horizontal, negative values correspond to ascending and positive values to descending neutrinos. The simulation script also takes a job number, which is is set to the array task id. In this way, several jobs can be started at once and multiple simulation files can be produced with the same parameters simultaneously. Additionally, the interaction type can be set by `cc` for charged current, `nc` for neutral current or `ccnc` for mixed simulations.

In the simulation script the provided input parameters are read in and several parameters, which are not further varied, are set such as the inclination azimuth, which ranges from 0 to 2π, to cover a full sphere ring of possible arrival directions of neutrinos. The zenith arrival direction is ranging from the imported minimum zenith inclination angle to the minimum increased by 0.1. In a next step a volume for the interactions to happen in is defined. Depending on the keys of the volume dictionary a cylinder or cuboid can be defined. In the following a cylinder with a radius of 3 km is defined with a depth from 0 km to 2 km. A sketch of this fiducial volume is shown in Figure 3.1 placed at Summit Station. The red line indicates the detector string which will be introduced

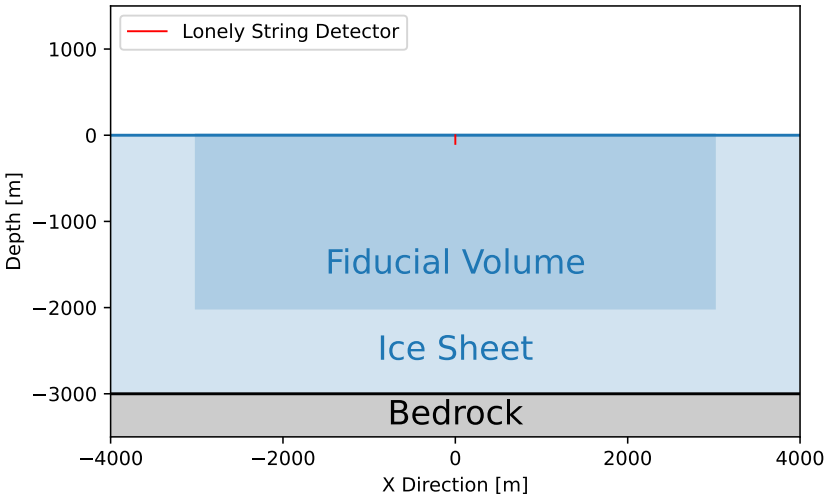

Figure 3.1: Vertical cross-section through the simulated Greenlandic ice sheet. The detector sting (red) is placed in depths down to −100 m. The fiducial volume is a virtual volume of ice, which is defined as a cylinder around the detector string. Simulated showers from neutrino interactions happening in the fiducial volume will be saved for further analysis. On the bottom the ice is confined by bedrock.

in subsection 3.2.1. Showers that happen inside this fiducial volume will be recorded for further investigations and simulations. Its size and shape are chosen such that it covers the volume of the ice in which the detector is able to record showers but not to simulate showers too far away from its field of view. It will be shown in section 4.3 that the chosen dimensions are reasonable for showers at an energy of 10^{19} eV. For the simulation the string to set the neutrino flavor are translated into the Particle Data Group numbering scheme [13], where electron neutrinos are indicated as 12, muon neutrinos as 14 and tau neutrinos as 16. The anti neutrinos are denoted by the respective negative number of their partner. If for example `e` is indicated as the neutrino flavor, a list of [-12, 12] will be used to simulate electron neutrinos and anti electron neutrinos in equal parts. Further, a minimum energy of 10^{-3} of the initial energy is set. Subshowers with smaller energies will not be further propagated in PROPOSAL, since lower energetic showers are more common but are rarely triggering the detector [39]. As number of events per job initially 2000 events were set to be simulated. This number needs to be adapted to the other parameters of the simulation, such that a high enough statistics for the following analysis is achieved. A start ID for the event ID is chosen. Each event is supposed to have a unique event ID.

All set parameters are handed over to the NuRadioMC function `generate_eventlist_cylinder`. For the prospective usage of PROPOSAL a PROPOSAL configuration file is set. In the following the configuration file of `Greenland` is used, which contains the definition of a spherical Earth, a 3 km thick ice sheet, confined by non-reflective bedrock at the bottom and air above [40]. Additional keyword arguments for the call of PROPOSAL are given by a dictionary containing the lower limit energy of particles and showers at which the propagation will not be continued further.

In a first step the defined fiducial volume V_{fiducial} is expanded and a volume V_{full} around it is defined. While the original neutrino interaction might not happen within the fiducial volume, the secondary interactions of these propagating leptons might happen close to

the detector. Thus, depending on the set maximum energy the 95% percentile of the propagation length of a tau of this energy is calculated and the detector radius expanded by this distance. Due to the increased volume, the number of simulated events gets increased by $\frac{V_{\text{full}}}{V_{\text{fiducial}}}$, such that the number of neutrinos interacting in the initially defined volume statistically stays the same. For a neutrino with an energy of 10^{19} eV, the radius gets increased by 76.2 km. Thus, instead of the initially set 2000 events, 1 392 540 events are simulated in the increased volume.

The vertex coordinates of the initial neutrino interactions are uniformly randomly distributed in the full volume. The arrival direction of the neutrinos are uniformly randomly distributed for the azimuth and for the zenith under consideration of the minimum and maximum values given in $\cos(\theta)$. By taking the cosine of the angle, the area of the spherical segment is the same for all zenith limits of $\cos(\theta)$ and $\cos(\theta) + 0.1$. The flavor for each event is chosen randomly from the provided list of flavor numbers. The energy is selected randomly between an upper and lower energy limit according to a spectrum model. In this case the neutrino energy is well defined, so the upper and lower limit are set to the same energy. In a next step the inelasticity, i.e. the fraction of energy absorbed by the stationary nucleon is calculated by drawing its value randomly from the expected distribution at ultra high energies.

Each neutrino-nucleon interaction contains one hadronic shower as explained in 2.1. Its energy is the energy absorbed by the nucleon i.e. the calculated inelasticity times the total energy of the initial neutrino. Its shower type is saved as `had` for hadronic.

In the case of electron neutrinos interacting via a charged current an electromagnetic shower is simply added with the leftover energy from the scattering, namely

$$(1 - \text{inelasticity}) \cdot E. \tag{3.1}$$

To simulate emerged muons and taus from CC events caused by muon and tau neutrinos, the package PROPOSAL is used. Just like the electromagnetic shower from the CC interaction of an electron neutrino, the resulting lepton obtains the leftover energy $(1 - \text{inelasticity}) \cdot E$. Due to the numbering of the particles the corresponding lepton to a neutrino can be calculated via $(N_{\text{neutrino}} - 1) \cdot \text{sgn}(N_{\text{neutrino}})$. A muon neutrino with number N_{neutrino} 14 will yield a muon with number 13. Since the volume has been expanded and the position and direction of the neutrino has been chosen randomly, the neutrino might interact but the shower and secondary particles will never cross the investigated volume V_{fiducial}. These events are discarded and not further simulated.

In the following the iteration over the individual events is started: if the initial neutrino interaction happens inside the initial volume it will be appended as one interaction. The parameters of the previously selected events where the secondary crosses the volume are fed into PROPOSAL. For the simulation of the muon and tau interactions in the ice the cross-sections predefined in NuRadioMCs `Greenland` proposal config file were used. The cross-sections σ are shown in Figure 3.2a for muons and in Figure 3.2b for taus in dependence of their energy E in ice. In general, the cross-section increases with the energy except for muons participating in bremsstrahlung, where the cross-section gets reduced at extreme energies due to the LPM effect. For muons the total cross-section is dominated by bremsstrahlung and photo nuclear interactions up to an energy of $4 \cdot 10^{15}$ eV. Above,

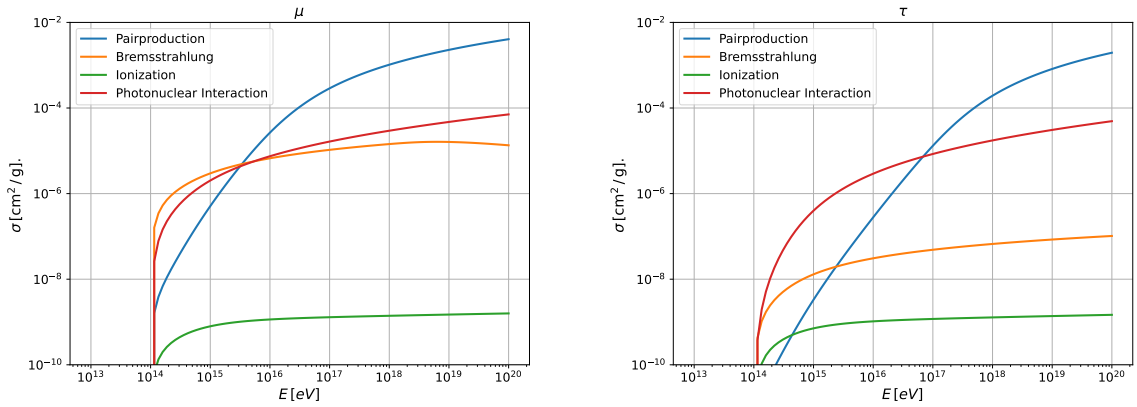

(a) (b)

Figure 3.2: Cross-sections for different interactions used by PROPOSAL. Figure 3.2a shows the cross-sections for muons and Figure 3.2b for taus in the dependence of the lepton energy.

the main energy loss is caused by pair production. For taus the cross-section is in general smaller than for muons. The bremsstrahlung is reduced due to the tau's larger mass and the energy loss is dominated by photo nuclear interactions up to energies of $6 \cdot 10^{16}$ eV. Beyond, pair production contributes the biggest share. The properties of the resulting secondary showers with energies above the set minimum energy are given back.

By iterating over all resulting decay products provided by PROPOSAL, and rejecting the ones outside of the fiducial volume, their parameters like the number of interaction, the parent and shower energy, the interaction and shower type as well as the position of the interaction and the time delay between the initial neutrino interaction and the shower interaction are obtained and saved.

If the option to use PROPOSAL is turned off, only the neutrino interaction in the initial volume is saved. The secondary muon or tau are treated as escaped.

Each saved shower obtains a `shower_id` which is consecutive over multiple events in one data set. Finally the events are saved as .h5 files. The produced simulation files are now ready to be processed further to compute which of the simulated showers will be seen by the detector.

3.2 Radio Signal Propagation and Simulation of Detector Operation

Due to the elaborate computing performance needed for the simulation the calculation was also performed on the HPC cluster. Therefor a shell script is needed for job submission. Besides the computing specifications energy, inclination and type of current are specified. From these parameters the name of the previously generated neutrino event file is put together and passed on to the python script handling the further simulation. Additionally the python script takes two file path for the two kinds of output files, namely a .nur file containing all information and a .hdf5 file with a reduced set of resulting parameters. .nur is a specific file format for NuRadio which contains the simulated traces and simulation

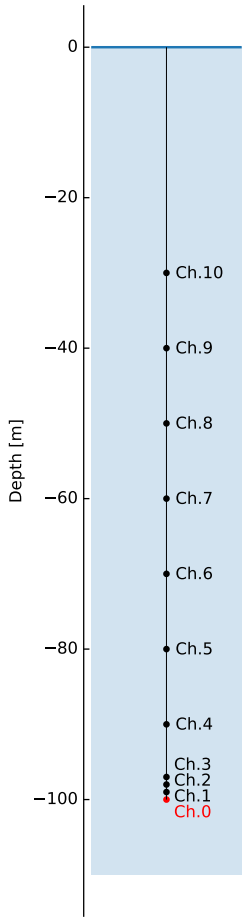

Figure 3.3: Detector layout of simplified station setup `Lonely String Detector`. The eleven channels consist of Vpol antennas, where the lowest antenna, Channel 0 (red) is used for triggering.

quantities. It has the advantage that the simulated events are saved successively during runtime [41]. For the further simulation the description of the detector is necessary and also provided at this point as a path to a detector file as well as a configuration file specifying further parameters of the simulation. The set parameters in the detector file and configuration file as well as the main python script will be discussed in the following.

3.2.1 Detector File

The detector is defined in a .json file, consisting of two parts: the configuration of the individual channels, i.e an individual antenna with its electronics and trigger and the configuration of the stations consisting of several channels, forming the whole detector. Each channel and station is defined by a set of keywords. The channel ID is unique in each station. And the station ID numbers the stations. In the definition of the channels it is used to define which channels will form a station together in case different station types are use as for example in the case of IceCube-Gen2 Radio. The detector description is explained through the example of the Lonely String Detector Configuration, which will be used for the simulation later on. It is shown in Figure 3.3. It is a simplified version of the power string in RNO-G, without the Hpol antennas, but an increased number of Vpol antennas.

Each channel is defined by an antenna type. For the Lonely String Detector Configuration RNO-G Vpol antennas centered in a borehole with an diameter of 5.75 inch are used. The index of refraction at the channel is 1.73 corresponding to the index of refraction at depths below the firn. The antenna type is predefined by NuRadioMC [42] including the antenna response, which depends on the index of refraction of the surrounding medium. The position of each channel is defined in Cartesian coordinates relative to the center of a station. In this simplified case, the center of the station is the position of the borehole. Negative Z values denote an antenna buried in the ice. The positions of the channels are shown in Figure 3.3. The deepest channel is placed at a depth of 100 m. Channel one to three are placed in 1 m distances above. Between a depth of 30 m and 90 m channels are placed with distances of 10 m. In total this station contains eleven channels. A defined antenna can be rotated. Therefor two axes are defined by two angles θ and ϕ. The orientation points in the direction of the antennas most sensitive direction. The rotation axis is orthogonal to it [43]. A cable delay can be defined for the individual channels. NuRadioReco provides a default RNO-G detector description in which realistic cable delays are predefined. Since the Lonely String Detector has additional channels the cable delay of the upper three channels was extrapolated linearly in dependence of the channel depth. The resulting relation between delay Δt and the channel depth z was determined to be:

$$\Delta t = -4.9349 \cdot z + 192.749. \tag{3.2}$$

The used amplifier is also defined by predefined keys. Here `iglu` (In-ice Gain with Low-power Unit) is used. For the analog to digital converter the sampling frequency is set to 3.2 GHz and the number of samples to 8192. This is four times as long as the currently implemented RNO-G readout length. A longer readout time was chosen to record more signals from created showers used for differentiating flavors. This also fixes the duration of the resulting trace to a length of 2560 ns. Additionally, the number of bits `nbits` is set to 8. The number of noise bits `noise_nbits` is set to 5. Thus an ADC value of 2^5 will correspond to the root mean squared voltage V_{RMS} of the noise, which will be specified in the configuration file. As a result the maximum voltage is also fixed and set by $V_{\mathrm{RMS}} * ((2^{\mathrm{nbits}}) - 1)/((2^{\mathrm{noise\_nbits}}) - 1)$.

The key "noiseless" specifies whether or not the simulated traces of the individual channels contain thermal noise from the electronics. For the Lonely String Detector Configuration a noiseless and a noisy version was used to investigate the influence of noise.

In general a detector array consists of several stations placed apart. For simplicity the Lonely String Detector Configuration only consists of one string, thus lonely. Nevertheless this one station needs to be defined. Each station possesses information about its commission and decommission time. For these simulation purposes this info is inconsequential, but might be helpful for detector arrays in development. Each Station has a position in eastern and northern direction specifying the position of the central point of the station to which the channels are placed relative to. The origin of these coordinates corresponds to the origin of the fiducial volume specified in the neutrino simulation script. Here the string is placed at (0,0). The altitude of the station can be specified and was set to zero. The station ID sets the individual ID of the station within the detector array.

The reference station number indicates, that all channels with this station ID are part of this station. Usually it corresponds to the lowest station number with this configuration.

3.2.2 Configuration File

In the configuration file additional, from the detector independent, simulation parameters are set. The configuration file is partly structured in sections for better oversight. Firstly, the parameters for the weights are set. The weights consider the attenuative effects of the Earth on the initial neutrino. This is important for neutrinos with inclinations < 0, surpassing the Earth. In the following only neutrinos with inclinations > 0 are simulated and investigated, where the weights can be neglected. The parameter `noise` defines whether or not noise is added onto the final trace. Its value needs to coincide with the set truth value in the detector simulation. Additionally a sampling rate for internal calculations is set in GHz, but the final trace will have the sampling rate specified in the detector file. The `split_event_time_diff` was set to 5000. It defines a time span in ns which is the minimal time in between two starting traces. It is chosen longer than the trace length resulting from the set parameters in the detector file, to not have the same signals in multiple traces, which would skew the final results. A seed was set for reproducibility to 1205. In the speedup section of the configuration file, the `minimal_weight_cut` is set to 10^{-5}. Events induced by initial particles with a weight of less than the set value are not further computed, since the probability for the initial particle to survive the passage through Earth is too small. A second termination condition is set with the `delta_C_cut`, which was set to $\cos(\alpha)$ of 0.349 corresponding to an angle of 20°. If the path between the shower vertex and antenna obtained by the ray tracer is off more than this angle from the Cherenkov angle introduced in 2.3 the event is excluded as well, since the signal does not coincide anymore and the resulting amplitude would be too low. Electric fields arriving at the antenna with low amplitudes compared to the noise, will not lead to useful results, since the signal will get lost. To exclude these events and save time by not simulating the detector response the minimal electric field amplitude can be set in multiples of the V_{RMS}. Here the value is set to 0.5. The maximum amplitude of the trace and its timing will be calculated and saved in the files, since `amp_per_ray_solution` is set to True. Next, parameters for the radio wave propagation in ice are defined. As an ice model `greenland_simple` was chosen, which provides the index of refraction. It is implemented in NuRadioMC as a keyword and calculates the index of refraction from the density profile obtained by [44]. As an attenuation model `GL1` for Greenland was used, which returns the attenuation length at 75 MHz as a function of depth. The measurements used therefore were provided by [45] as stated in the NuRadioMC documentation [46]. To be actually used `attenuation_in_ice` needs to be set to True. The module used for ray tracing between the shower vertex and the antenna position is `analytic`, since the ice model is simple and therefore an exponential refractive index is assumed [47]. The attenuation length is calculated for 25 frequencies and interpolated in between. Since the index of refraction is changing with depths the radio waves may bend which might lead to the focusing of the radio waves and change in the amplitude of the signal. This is considered since `focusing` is set to True and the `focusing_limit`, which gives the maximum amplification factor is set to two [36]. Since events in Greenland ice are simulated, which is confined at the bottom by non-reflective bedrock, `n_reflections`, which give the maximum number of reflections off the bottom layer, is set to zero.

In the signal section, the model which is used to receive the electric field strength from the input showers is specified. Here `ARZ2020` is used. A library of charge excess profiles for different kinds of showers at different energies is used. The electromagnetic potential A can be calculated from these charge excess profiles and the relative position to the shower. From A the electric field E can be calculated. The model also contains the LPM effect from the kind of shower and its energy. While the `ARZ2020` model is computing intensive it treats LPM effect realistically [36]. The `zerosignal` parameter can be set to True if only noisy traces without any neutrino signals should be created. Then the signal is just set to zero. This is used for an extra set of pseudo events to investigate the possibility to differentiate muon neutrinos from background noise. In the trigger section the noise temperature is defined. It stems from the ambient temperature as well as noise from the electronics. For this simulation it was set to 300 K. Due to the thermal jitter of electrons in the electronics, so called Johnson noise on the measured voltage trace is unavoidable. As a quantity for the noise on the final trace the root mean squared of the voltage V_{RMS} is used. It can be calculated from the temperature T by:

$$V_{RMS} = \sqrt{4Rk_BTG}, \tag{3.3}$$

where R is the resistance, k_B the Boltzmann constant and G the gain integrated over the band pass region [48]. In the ideal case, where the gain in the dedicated bandwidth is always 1, it can be replaced by the bandwidth of the channel Δf. In the implementation of NuRadioMC the value of $4R$ has been set to a value of 50. Finally the root mean squared of the voltage only depends on the temperature and the bandwidth

$$V_{RMS} = \sqrt{50\Omega \cdot k_BT\Delta f}. \tag{3.4}$$

Since Johnson noise is white noise with a normal amplitude distribution [49] V_{RMS} is equivalent to the standard deviation of the noise amplitude σ_V [10]. With the bandwidth of the filters defined in 3.2.3 one obtains $V_{RMS} = 0.0117\,\mathrm{V}$. In the output section it is specified if the measured channel traces should be saved. Additionally the electric field traces, that arrive at the antennas are saved individually as well. This could be turned off to save disk space.

3.2.3 Simulation Script

In the Python simulation script the filter and trigger parameter for each channel are defined. Since the Lonely String Detector Configuration only uses one type of antenna, all filters are the same. The time duration which will be recorded prior to the trigger reacting is set to 1000 ns. Thus signals in higher channels will still be visible in the traces even tho the pulse arrives earlier at the channel than at Channel 0, which solely will be used for triggering. The duration before the trigger does not influence the total length of the trace but rather shifts the recorded trace to the past. For the simulation two additional functions have to be defined for the simulation.simulation class: `_detector_simulation_filter_amp` and `_detector_simulation_trigger`. The first one applies the RNO-G hardware response that is implemented in NuRadioReco on to the simulated trace. The definition of `_detector_simulation_trigger` is more elaborate. First, bandpass filters are applied using Chebyshev filters. They are applied sequential on the ranges of 0 MHz to 220 MHz and 96 MHz to 100 000 MHz. Afterwards the trigger is defined. The trigger value is given in values of V_{RMS}. Here the threshold is set to

Initial Energy [log(eV)]	Inclination [cos(θ)]	Number of ν_e Events	Number of ν_μ Events	Number of ν_τ Events
Analysis Events		CC Interaction		
19.00	0.0 to 0.1	49788	139103	246932
19.00	0.4 to 0.5	50010	69590	65687
18.00	0.0 to 0.1	49989	144416	175974
18.00	0.4 to 0.5	49984	69457	65031
Analysis Events		NC Interaction		
19.00	0.0 to 0.1	49830	49706	50129
19.00	0.4 to 0.5	50212	50029	49842
18.00	0.0 to 0.1	49514	49909	50173
18.00	0.4 to 0.5	49799	50341	50199
Template Construction		CC Interaction		
19.00	0.0 to 0.1	-	139301	-

Table 3.1: Number of simulated neutrino events for varied energy and inclination range for each flavor and interaction type. An additional set of muon neutrino events has been simulated for the determination of the template in section 5.3.

2 V_{RMS} to record the trace if the signal surpasses this value. It is applied only on the deepest channel: Channel 0, indicated in Figure 3.3 in red. The script makes sure the requested output paths exist and defined an instance of the just fully defined simulation class. Finally, the simulation is started. The further simulation will not be explained in detail and is treated as a black box. After the simulation has been fully conducted two types of files are exported: one hdf5 file with array like storage of main quantities, but without traces and several .nur files, tha custom data output format of NuRadioMC.

3.3 Simulation Set

Concluding, an overview of the generated events in the scope of this work is given. For the event simulation 25 jobs with initially 2000 neutrino events were computed per flavor, energy, inclination and interaction. For each of the three neutrino flavors events with an energy of 10^{19} eV and 10^{18} eV were simulated with inclinations in ranges of 0.0 and 0.1 and 0.4 and 0.5. For all combinations pure NC and CC interactions have been simulated. Additionally, a second set of events for muon neutrinos at 10^{19} eV with inclinations of 0.0 and 0.1 for CC interactions has been simulated to use in section 5.3 to obtain an unbiased template for convolution. In total $25_{\text{jobs}} \cdot (3_{\text{flavor}} \cdot 2_{\text{energy}} \cdot 2_{\text{inclination}} \cdot 2_{\text{interaction}} + 1) = 625$ event files have been created. The number of events is shown in Table 3.1. The numbers vary around the set value of 50000 for electron neutrinos and NC events, due to the increase of the simulation volume. For CC interacting muon and tau neutrinos more events have been simulated due to events where the initial neutrino interaction lies outside of the fiducial volume and the detector is triggered by the showers of the produced secondary lepton.

The detector simulation was computed with and without added thermal noise. For the noiseless simulations all previously mentioned event files were used. The noisy simulations were only performed for energy of 10^{19} eV. Lastly, a set of noise only events was created using the initial event files of the muon neutrino at 10^{19} eV at inclinations of 0.0

Initial Energy [log(eV)]	Inclination [cos(θ)]	Number of ν_e Events	Number of ν_μ Events	Number of ν_τ Events
Noiseless Traces		NC Interaction		
19.00	0.0 to 0.1	1563	1533	1548
19.00	0.4 to 0.5	1962	1918	1865
18.00	0.0 to 0.1	214	184	199
18.00	0.4 to 0.5	268	285	289
Noisy Traces		NC Interaction		
19.00	0.0 to 0.1	2112	2091	2116
19.00	0.4 to 0.5	2338	2304	2230
Noiseless Traces		CC Interaction		
19.00	0.0 to 0.1	3383	4816	4938
19.00	0.4 to 0.5	3581	3882	2592
18.00	0.0 to 0.1	638	362	321
18.00	0.4 to 0.5	806	378	308
Noisy Traces		CC Interaction		
19.00	0.0 to 0.1	4047	11446	14784
19.00	0.4 to 0.5	4004	5968	3800
Noise only Traces				
19.00	0.0 to 0.1	-	2095	-
Template Construction		CC Interaction		
19.00	0.0 to 0.1	-	4864	-

Table 3.2: Number of triggered events in the Lonely String Detector resulting from the simulated neutrinos in 3.1. The detector response was simulated without noise for two different energies and inclinations, while for the simulation including noise only the inclination was varied.

and 0.1 and CC interactions. Since for these simulation `zerosignal` was set to True, the used event file is irrelevant. Table 3.2 shows the number of resulting events after the detector simulation. For CC interactions more events are detected as for NC events due to a higher number of simulated neutrinos. A higher energy results in more events as well. The simulation of events with noise on the traces also yields more events as for noiseless traces. For the simulation of noise only events the input file of CC interacting muon neutrinos of an energy of 10^{19} eV was used. Since the arriving signal was set to zero before triggering on the noise, this input file is not substantial. It is to note, that for the simulation of traces with thermal noise for muon neutrinos with inclinations of 0.0 to 0.1 the simulation did not finish due to limited memory and computing time. A possible fix would have been to divide the event files into smaller batches. Since the number of simulated events is sufficient and the hitherto simulated events have been saved in .nur files the only penalty is not to have obtained the final .hdf5 files. Conveniently, they are not mandatory for the following analyses. In the case of traces with thermal noise from charged current interactions of muon and tau neutrinos the event numbers are not necessarily unique, since a channel can be triggered a second time additionally at random from noise.

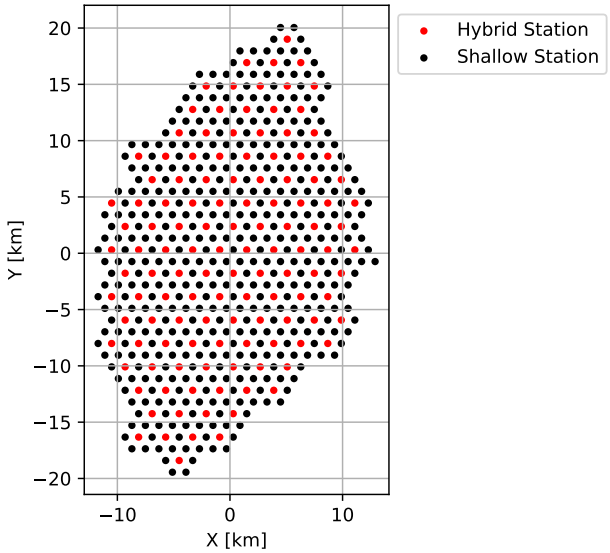

Figure 3.4: Map of the proposed IceCube-Gen2 Radio layout used for the analysis of the multiplicity in chapter 7. In black, shallow stations, consisting of shallowly deployed LPDAs, are shown. The hybrid stations shown in red consist of a shallow and a deep component as explained in 3.4.

3.4 IceCube-Gen2 Radio Simulations

In chapter 7 the approach of distinguishing muon neutrino events by the number of triggered stations in a detector array is investigated. Therefor the Lonely String Detector Configuration is, as the name suggests, unsuitable, since it only consists of one station. For this purpose a set of simulated events was provided by S. Hallmann. These simulations were performed with NuRadioMC (Version 2.1.6) and Proposal Version (6.1.6). A suggested IceCube-Gen2 Radio Detector Layout is used as described in 2.5 with a station distance of 1.2 km. A sketch of the station layout is shown in Figure 3.4. For the shallow component consisting of the LPDAs, the trigger checks for the coincidence of two of the four stations. The deep component uses a phased array trigger shifting and adding the traces of four channels to amplify signals and to average out the noise [34]. In both cases the threshold is selected such that an application of the trigger to pure noise would yield a trigger rate of 100 Hz.

The inclinations were also set to a $\cos(\theta)$ range of 0.1. Where the maximum investigated inclination range was 0.9 to 0.1, i.e. vertically from above. The minimum investigated inclination range depends on the initial neutrino energy: at 17 log(eV) the minimum inclination range was -0.6 to -0.5, at 17.5 log(eV) -0.5 to -0.4, at 18 log(eV) -0.4 to -0.3 ant at energies of at 18.5 log(eV) -0.3 to -0.2. These ranges were chosen since for higher energetic particles the probability to surpass the Earth decreases. Therefore inclinations with long traverses through Earth are rare and not of substantial interest. For these combinations all three neutrino flavors for NC and CC interactions were simulated separately.

Chapter 4

General Event Characteristics for Different Neutrino Interactions

In this chapter the simulated events are investigated with regard to how different parameters manifest themselves in the spatial and energetic characteristics of the events. Neutral current (NC) and Charged current (CC) interactions as well as different neutrino flavors, initial energies and inclinations are compared. At first, the energy spectra of the simulated showers in the detector volume are investigated. The number of induced showers per event are evaluated to estimate how promising a separation of neutrino flavors by the number of recorded particles showers is. Finally, the spatial distribution of triggered showers around a single detector string is visualized to judge the range of vision in dependence of the event parameters. From these characteristics approaches to differentiate neutrino flavors can be deduced and used later to justify an explain the feasibility of different flavor differentiation techniques.

4.1 Energy Spectrum of Simulated Showers

First, the neutrino files produced in section 3.1 are analyzed, before the detector response is considered. Figure 4.1 shows the energy spectrum of the simulated showers. Figure 4.1a and Figure 4.1b show the distributions for neutrinos with an initial energy of 10^{18} eV and an inclination between 0.0 and 0.1 and 0.4 and 0.5, respectively. Figure 4.1c and Figure 4.1c show the distributions for initial neutrino energies of 10^{19} eV for the same two inclination ranges. The energy on the x-axis as well as the amount of showers within an energy bin on the y-axis are shown on a logarithmic scale. In each plot four distributions are shown: the results from NC interactions are blue. Here, NC events from all three simulated neutrino flavor interactions were used together, since the flavor does not influence the results of NC simulations. The CC events with an initial electron neutrino are shown in orange, CC induced showers from muon neutrinos in red and from tau neutrinos in purple.

The shape of the NC shower spectrum is determined by the inelasticity distribution. For ultra height energetic neutrinos this distribution is energy dependent. The inelasticity is then multiplied by the initial neutrino energy. Thus, the NC shower distribution has the same shape for the simulated 10^{18} eV and 10^{19} eV data set, but is shifted by on order of magnitude towards lower energies for 10^{18} eV events. Since the inelasticity is independent from the inclination the NC distributions look the same in both investigated inclinations.

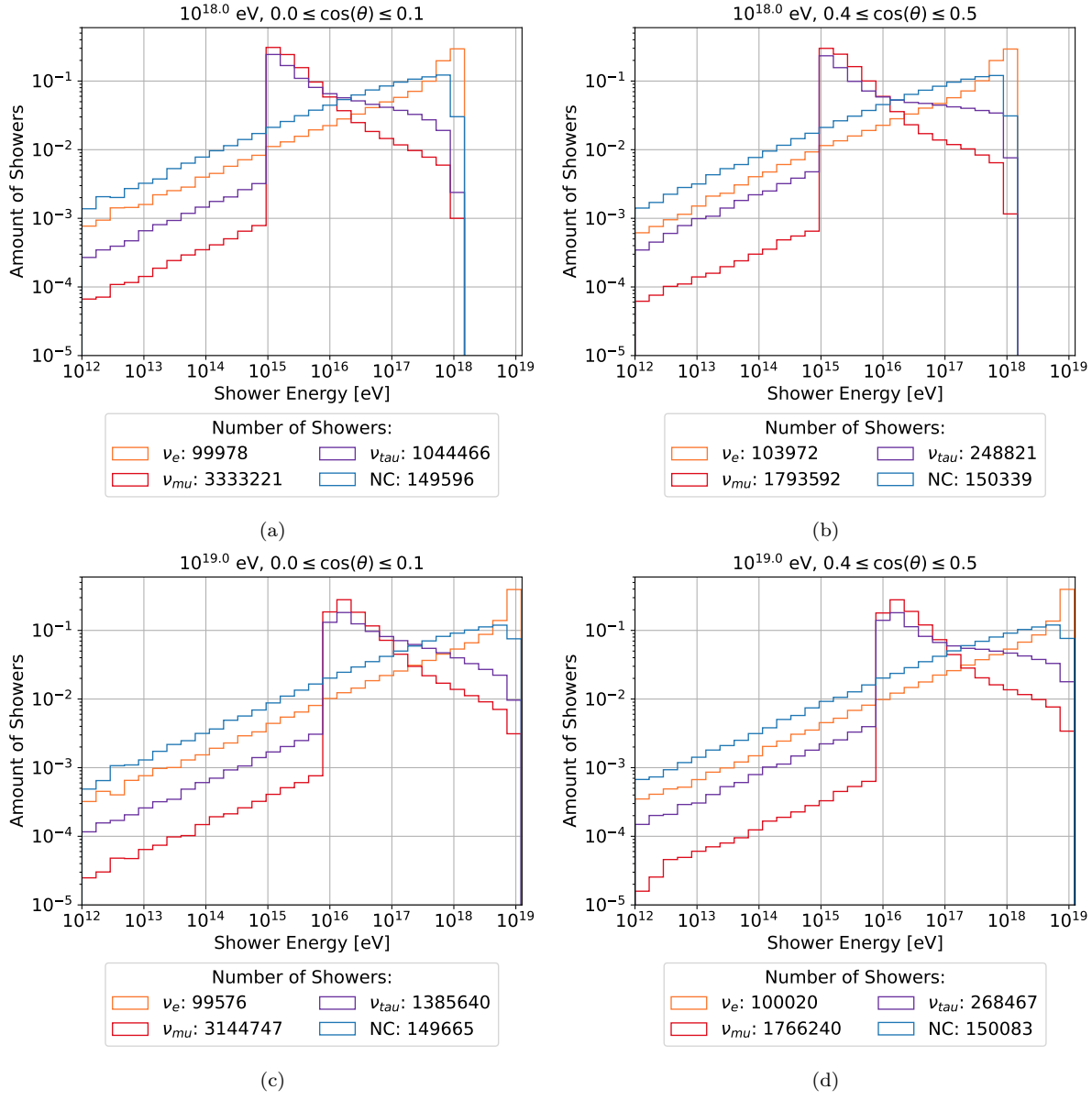

Figure 4.1: Energy spectrum for simulated showers following a neutrino interaction as explained in section 3.1. Each plot contains the spectrum of showers induced by NC interactions of all three neutrino flavors (blue) and the spectrum for showers produced by an initial CC interaction from an electron neutrino (orange), muon neutrino (red) or tau neutrino (purple). The plots in the upper row show the distributions resulting from initial energies of 10^{18} eV and the lower row of 10^{19} eV. The left plots show showers resulting from neutrinos with an inclination between 0.0 and 0.1, while the right plots stem from neutrinos with a more vertical inclination between 0.4 and 0.5.

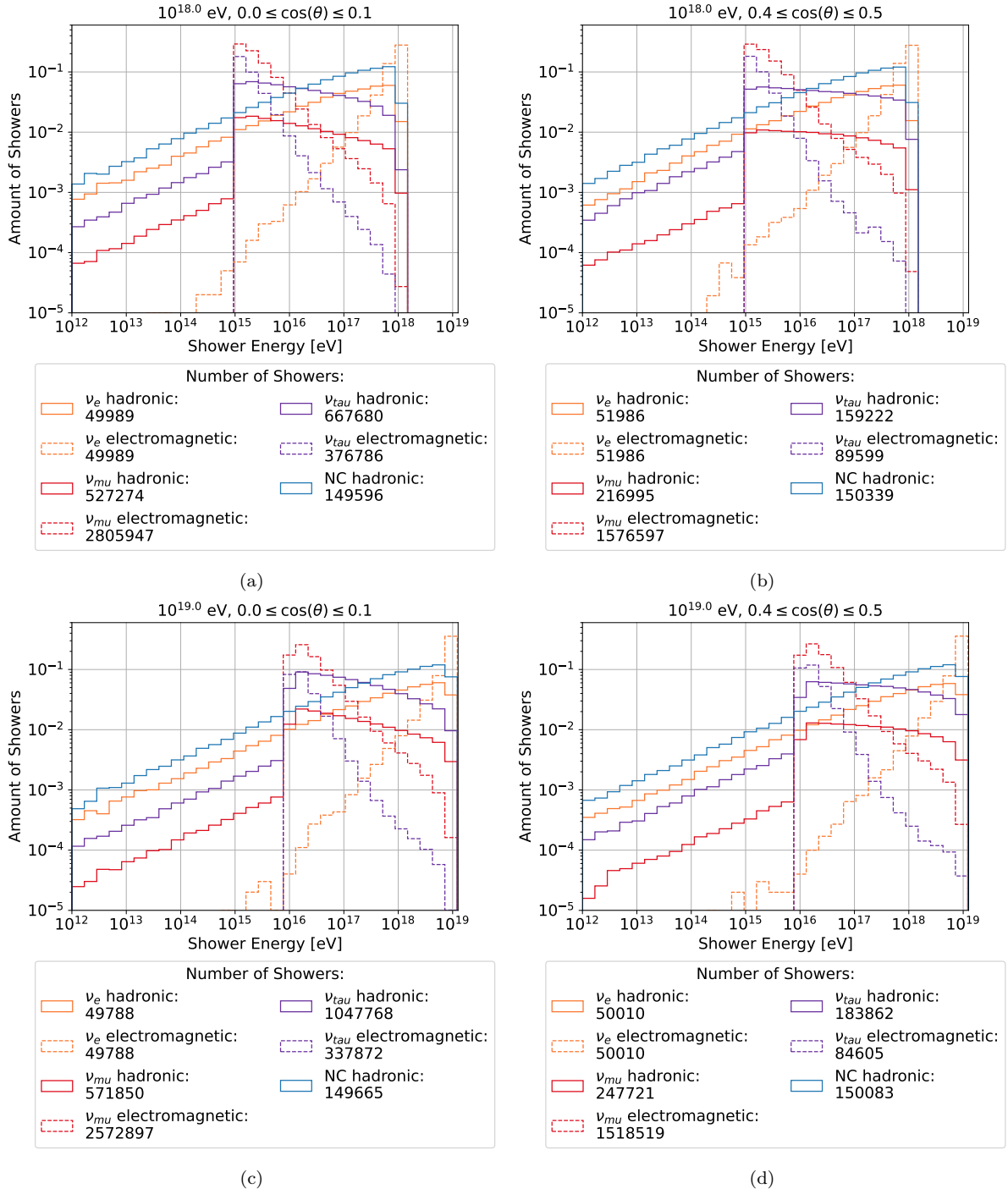

Figure 4.2: Energy spectrum for simulated showers following a neutrino interaction as explained in section 3.1 broken down in electromagnetic and hadronic showers. Each plot contains the spectrum of showers induced by NC interactions of all three neutrino flavors (blue) and the spectrum for showers produced by an initial CC interaction from an electron neutrino (orange), muon neutrino (red) or tau neutrino (purple). The plots in the upper row show the distributions resulting from initial energies of 10^{18} eV and the lower row of 10^{19} eV. The left plots show showers resulting from neutrinos with an inclination between 0.0 and 0.1, while the right plots stem from neutrinos with a more vertical inclination between 0.4 and 0.5.

For an initial electron neutrino an electromagnetic shower caused by the secondary electron is created additionally to the hadronic shower. While the energy distribution flattens at the high energies for NC interactions the CC interaction electron neutrino events peak at the highest energies. In the case of NC interactions a fraction of the initial neutrino energy gets carried away by the secondary neutrino,but in case of a CC event the secondary electron obtains this fraction of energy which results in an electromagnetic particle shower. The energy of the hadronic and electromagnetic shower in each event is the whole initial energy of the electron neutrino.

Figure 4.2 shows the energy distribution of the showers separated by shower type: solid lined histograms indicate the spectrum of hadronic showers and dashed lines the spectrum of the electromagnetic showers, both normalized to the total number of showers. The NC events only contain hadronic showers. The hadronic component of the electron neutrino showers follows the shape of the NC shower distribution, but is only half as high due to the additional amount of electromagnetic showers. The electromagnetic component peaks at the maximum energy. However, it will never obtain the full neutrino energy. Since the energy of the electromagnetic shower also only depends on the inelasticity, the spectrum does not changes for different inclinations and for different energies the spectrum is simply shifted as well.

By investigating the energy spectrum of the showers induced by muon neutrinos and tau neutrinos the sharp edge at 10^{15} eV for initial energies of 10^{18} eV and at 10^{16} eV for initial energies of 10^{19} eV originates from the minimum energy of saved simulated PROPOSAL showers as explained in section 3.1. This edge does not have any physical meaning since it stems from the simulation settings, that showers with less than one thousandths of the initial energy shall not be saved, since their energy is not sufficient to create measurable radio signals [39]. Therefore at the lowest energies only the hadronic showers stemming from the initial CC interaction are present. Though, they are not crucial due to their small amount and energy. Above the edge the relative amount of showers reduces with increasing energy. The energy loss of a muon with energy E can be described as:

$$dE/dx = a(E) + b(E)E \tag{4.1}$$

[13]. As a comparative value the energy loss rate b(E) in standard rock for muons and taus is given in [50]: The higher the muon energy, the higher the relative energy loss b(E). The decline in the plot is steeper for muon neutrino interactions than for tau neutrino interactions, which coincides with the literature values for standard rock.

Regarding the composition of these showers shown in Figure 4.2 the hadronic component not only contains the showers from the initial CC interaction but also from secondary showers simulated by PROPOSAL recognizable at the steep increase at the corresponding energy. Additional hadronic showers stem from photo nuclear interaction and, depending on the decay channel, tau decays [23]. The latter only happens in initial tau neutrino events and photo nuclear interactions dominate the energy loss of taus to energies up to $7 \cdot 10^{16}$ eV as shown in Figure 3.2. This explains the higher amount of hadronic showers of tau neutrino events compared to muon neutrino events. Consequently, the amount of electromagnetic showers is larger for muon neutrino events, since the muon energy loss mainly stems from electron positron pairs. The energy spectrum of muon neutrino and

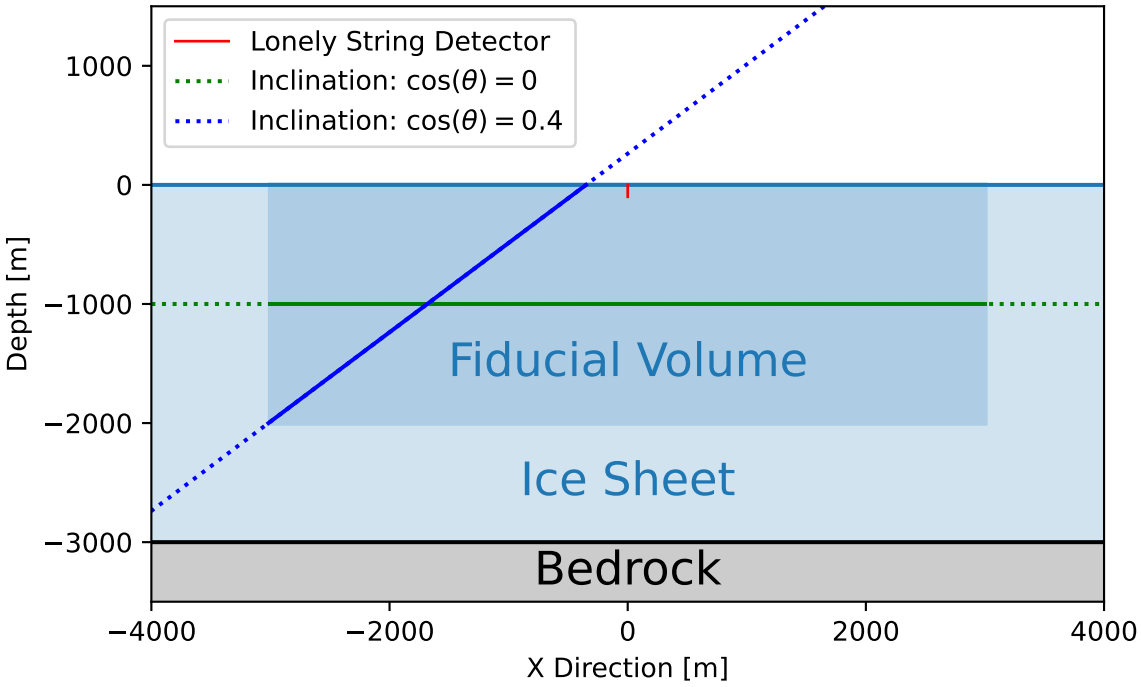

Figure 4.3: Cross-section thought the fiducial volume used for simulations. Only showers occurring in the fiducial volume are saved for further analysis by NuRadioMC. The green line shows the path of a particle with an inclination of 0 though the fiducial volume. The blue line shows the path of a particle with an inclination from ±0.4 depending on its direction of flight.

tau neutrino interactions broken up in the single interaction types simulated by proposal are shown in Appendix B. The mean number of showers per event is shown in Table 4.1. When comparing the effects of different inclinations, one essential change is the reduced total number of showers. The investigated fiducial volume is a disk cylinder with a diameter larger than its height. Figure 4.3 shows a vertical cross-section through it. The path through the cylinder for a larger inclination shown in blue is shorter than for a shallow inclination shown in green. Along this longer path more energy losses can happen, thus more showers will be saved.

4.2 Number of Showers per Event

Additionally to the energy per shower it is necessary to consider the total number of showers induced by one initial neutrino, i.e the number of showers per event. These distributions are shown in Figure 4.4. Each bin has a width of one, but to fully comprehend the number of showers for muon neutrinos and tau neutrinos the number of showers are plotted on a logarithmic axis. In the case of NC events the number of showers per event is trivial and always one, since there is only the hadronic shower from the initial interaction. Similarly, from CC interactions with an electron neutrino always two showers are obtained: the hadronic and the electromagnetic one.

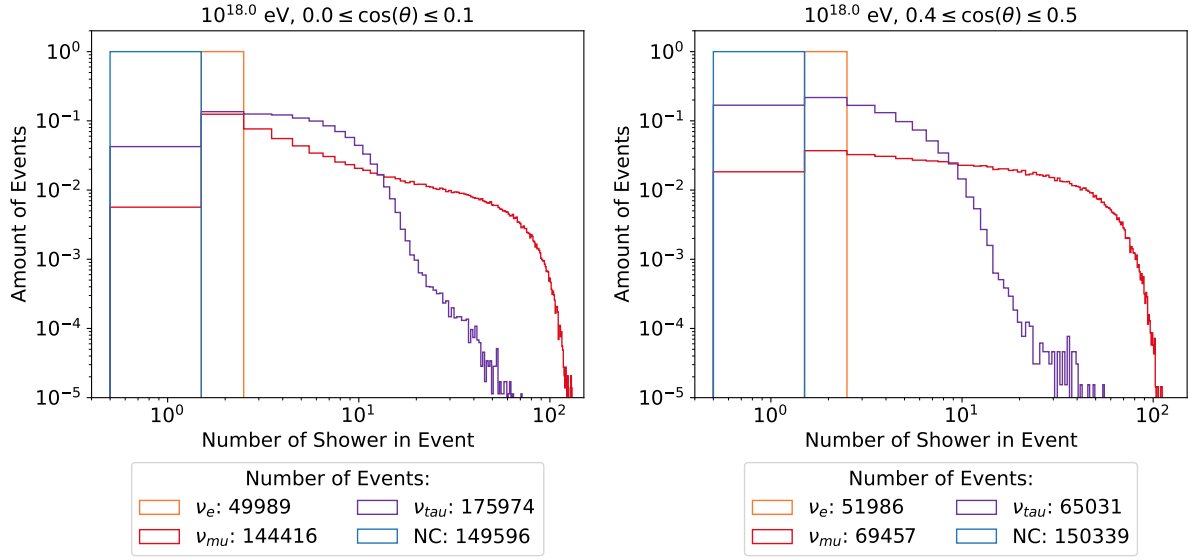

(a)

(b)

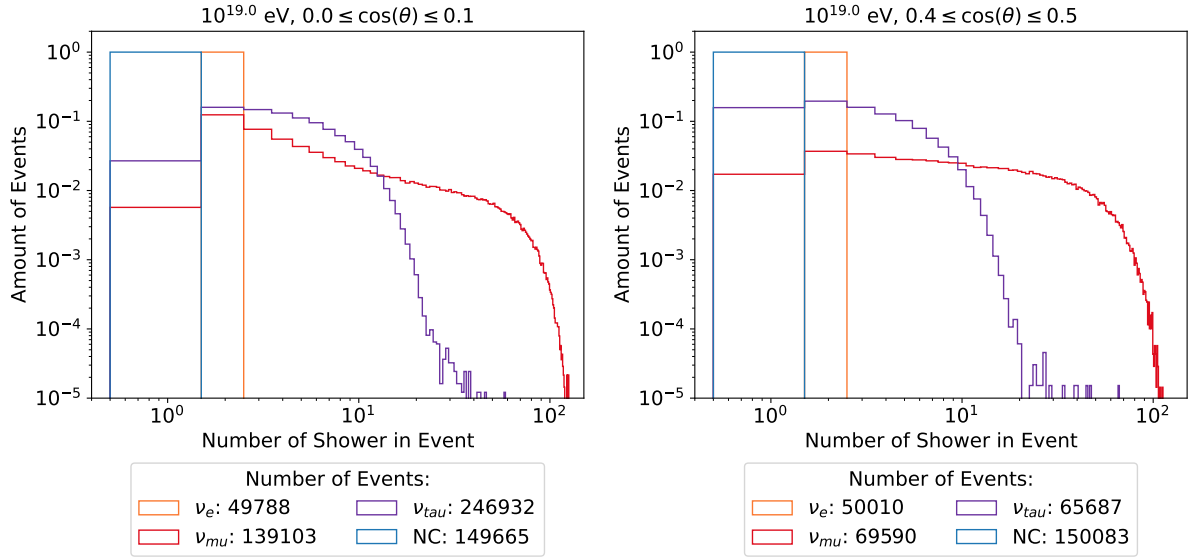

(c)

(d)

Figure 4.4: Histograms of the number of showers in each event for different neutrino properties. Each histogram bin has a width of one but due to the logarithmic x-axis the are depicted thinned for higher numbers of showers. The number of total investigated events is shown in the legend. The upper two plots show initial energies of 10^{18} eV and the lower plot initial energies of 10^{19} eV. The inclination range lies between 0.0 and 0.1 for the plots on the left and between 0.4 and 0.5 for the plots on the right. In blue the number of showers per event for mixed-flavor NC events is shown.

Initial Energy [log(eV)]	Inclination [cos(θ)]	Mean Showers per Event ν_μ	Mean Showers per Event ν_τ
19.0	0.0 to 0.1	22.61	5.611
19.0	0.4 to 0.5	25.38	4.087
18.0	0.0 to 0.1	23.08	5.935
18.0	0.4 to 0.5	25.82	3.826

Table 4.1: Mean number of showers per event for muon neutrino and tau neutrino CC interactions for the investigated energies of 10^{18} eV and 10^{19} eV and inclinations from 0.0 to 0.1 and 0.4 to 0.5

Due to the enhanced simulation of propagating muons and taus using Proposal the number of showers can exceed two. Events induced by tau neutrinos tend to have less showers than events induced by muon neutrinos due to the smaller energy loss rate.

If there is only one shower, it always stems from the initial CC interaction, where the secondary lepton escaped the fiducial volume. This happens less often for muon neutrino interactions than tau neutrino interactions . In events from steeper inclined neutrinos shown in Figure 4.4b and Figure 4.4d compared to more shallow inclinations shown in Figure 4.4a and Figure 4.4c it also happens more often to only obtain one hadronic shower. This again can be explained with the simulation volume geometry and the mean path of the secondary particles through this volume. Thus it is less likely for the secondary particle to interact during surpassing this shorter path.

When comparing the distribution of the number of showers per events at different energies, the spectrum for initial muon neutrinos does not change recognizably. The mean number of showers per event does decrease for muon neutrinos at higher energies. The distribution for the different energies at inclinations between 0.4 and 0.5 stays the same for tau neutrinos as well. Though, at more horizontal inclinations the amount of events with more than 20 showers decreases as well as events with only one event. . While the mean number of showers increases with the energy from 3.83 to 4.09 for the steeper investigated inclinations they are slightly reduced from 5.94 at 10^{18} eV to 5.6114 at 10^{19} eV at horizontal inclinations.

For the more horizontal events not only the total number of showers increases but also the number of events, that are saved increase at least a factor of two. This can be explained by the longer mean path length through the fiducial volume as shown in Figure 4.3. The mean number of showers per events increases for muon neutrinos for steeper inclinations but decreases for tau neutrinos. Comparing the number of shower distribution of the two inclinations at the respective energies, its form does slightly change: there are less events with more than 60 showers per event. Between 9 and 60 showers per event the relative amount increased but is again smaller for events with less than 9 showers. This happens for both investigated initial neutrino energies.

For tau neutrinos the distribution also changes with different inclinations: With steeper inclinations the distribution shifts to lower numbers of showers per events. This can be seen in the distribution and in the mean numbers of showers per event.

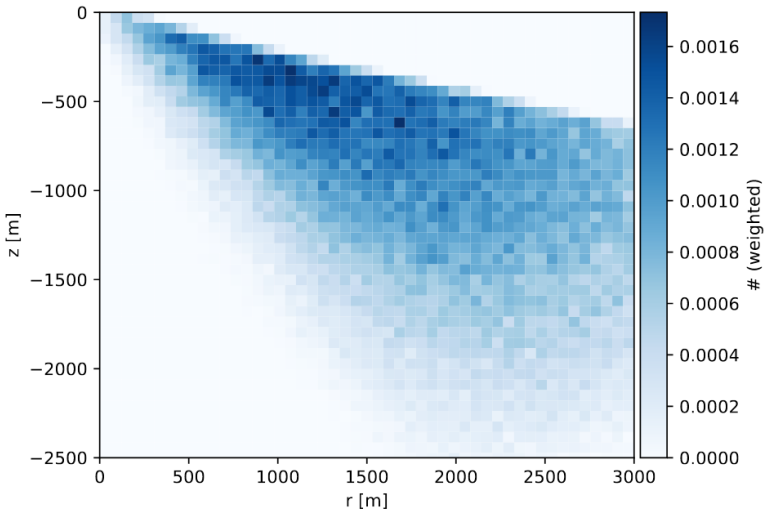

Figure 4.5: Vertex distribution of primary vertex neutrino interactions as seen by a 100 m deep dipole antenna with a 1.5σ trigger for neutrinos from all zenith and azimuth directions. The investigated neutrinos have energies between $1.2 \cdot 10^{18}$ eV to $2.3 \cdot 10^{18}$ eV. Figure from [23].

In the following the possibility of differentiating muon neutrinos from other events will be investigated. The task to differentiate muon neutrino CC events seems most promising due to the feature of large number of showers per event. The feasibility will be analyzed comparing to the three types of neutrino events: NC, electron neutrino CC and tau neutrino CC events.

4.3 Spatial Shower Distribution

In a next step the position of the detected showers relative to the detector station is investigated. Figure 4.5 shows the vertex distribution of initial neutrino interaction as seen by a dipole antenna at a depth of 100 m and a 1.5σ trigger. The investigated neutrinos have an energy between $1.2 \cdot 10^{18}$ eV to $2.3 \cdot 10^{18}$ eV and come from all directions [23]. The plot shows a 2D histogram of the positions of showers which were recognized the antenna. The x-axis shows the radial distance from the detector. The y-axis depicts the height. Negative values correspond to positions below the ice. The histogram is normalized to the total number of showers, but does not take into account, that the corresponding volume in which a shower can be of each pixel increases for higher radii. Such spatial distributions are investigated in the following for varying inclination, energy, neutrino flavor and interaction type. However, the triggering Channel 0 is a Vpol antenna at a depth of 100 m and uses a 2σ trigger, as described in chapter 3. Figure 4.6a shows the spatial shower distribution for muon neutrino CC interactions. The inclination of the incoming neutrinos is in the range from 0.0 to 0.1. As an initial energy of the neutrino 10^{19} eV is used. It can be observed, that the showers only can be seen in a certain angle range from the detector. If the angle between the shower, channel and surface is small, the radio wave has no possible path to arrive at the channel since it is bent downwards due to the gradient in the index of refraction in the ice. This region is called the 'shadow

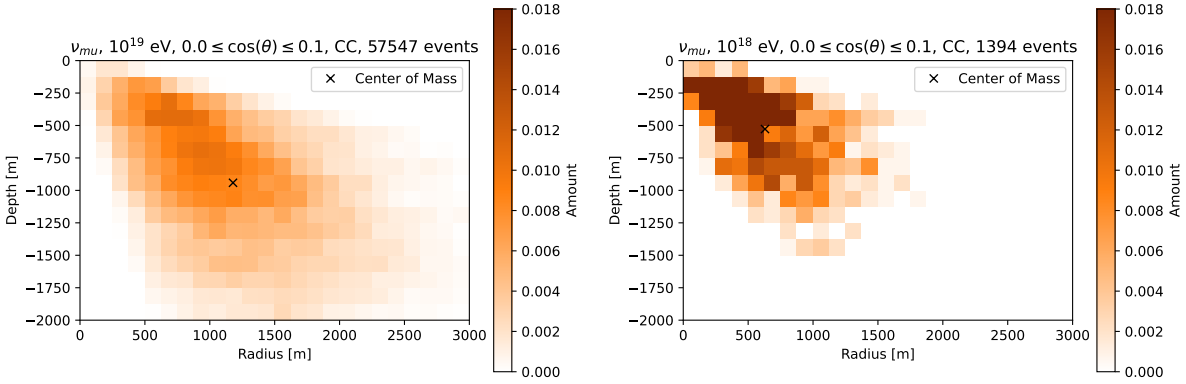

(a) (b)

Figure 4.6: Spatial distribution of all induced showers that are seen by Channel 0 of the Lonely String Detector. Initial neutrinos are interaction via the CC interaction and have an inclination between 0.0 and 0.1. Figure 4.6a shows the spatial shower distribution of showers originating from a muon neutrino with an initial energy of 10^{19} eV. Figure 4.6b shows the distribution of the showers induced by a 10^{18} eV muon neutrino. The blue cross in each plot shows the balance point of all detected showers.

zone' [51] [36]. Very close to the detector only very few shower are seen, due to the small volume compared to pixels further away. The maximum of the distribution lies a few hundred meters away from the detector. The mean position of the showers is indicated as a blue cross. With increasing distance less and less showers are observed. This is reasonable, since the distance between the shower and the antenna increases, leading to a reduction in the amplitude of the measured trace. It is to note, that the reduction does not follow a simple $1/\text{distance}^2$ law, since the ray path is bent and not solely the distance but the length of the path needs to be considered. Additionally the amplitude gets reduced due to the attenuation in the ice caused by impurities.

In comparison Figure 4.6b shows the spatial shower distribution for muon neutrinos interacting via CC interaction in the same inclination range, but at lower energies of 10^{18} eV. The mean position of the detected showers lies closer to the antenna. Due to the smaller initial energy of the neutrino, the resulting showers are less energetic, as discussed in section 4.1. This leads to a reduction of the charge excess in the shower. Thus, the amplitude of the emitted radio wave is smaller. Again due to a large distance and attenuation showers further away cannot be detected anymore at smaller energies. Figure 4.7 shows the shower distribution at energies of 10^{19} eV but at steeper inclinations in the range of 0.4 to 0.5. The zenith angle in which showers are seen is smaller for the steeper inclination. The area at which no showers are seen is increased for large inclination angles. The reason is shown in Figure 4.8: A cross-section through the ice is shown with the detector string indicated in red. Figure 4.8a shows an interaction with an inclination of the parent particle of $\cos(\theta) = 0$ and Figure 4.8b of $\cos(\theta) = 0.4$. The direction of the propagating paricle is shown as a dotted line from left to right. The shower position on the path, indicated by a yellow star at x=-333 m and z=-500 m is at the same position relative to the detector in both cases. The blue dashed lines, originating from the interaction point, indicate the Cherenkov cone section corresponding to the solid lines in Figure 2.3b. The colored triangles around $\pm 20°$ of the Cherenkov cone indicate the opening angle around the Cherenkov cone in which signals are still simulated by NuRadioMC as defined in subsection 3.2.2. If the ray tracing solution yields a viewing angle too far off of the Cherenkov cone the signal

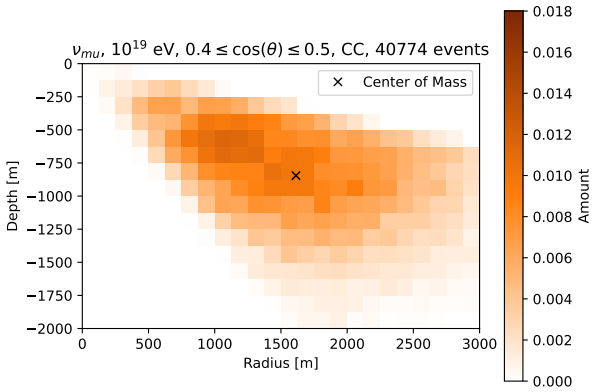

Figure 4.7: Spatial distribution of all induced showers that are seen by Channel 0 of the Lonely String Detector. Initial neutrinos are interaction via the CC interaction and have an inclination between 0.4 and 0.5. Showers are only visible in a smaller zenith angle range compared to incoming neutrinos with a steeper angle. The blue cross in each plot shows the balance point of all detected showers.

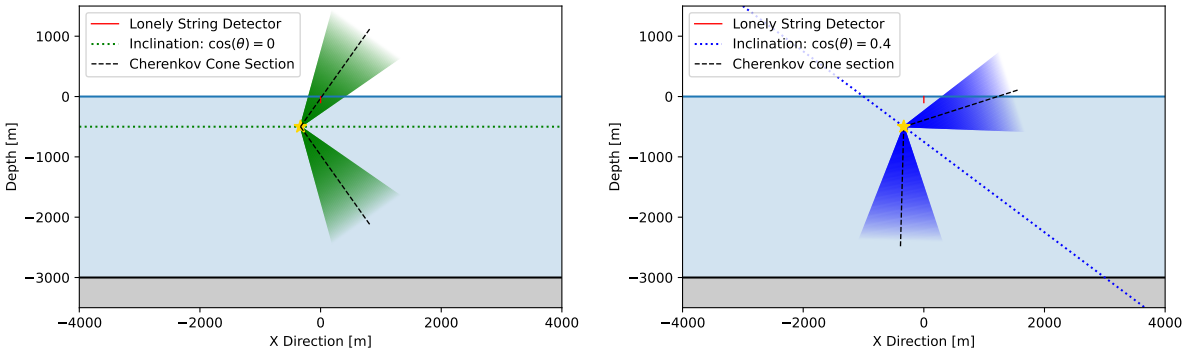

(a) (b)

Figure 4.8: Illustration of a shower position which leads to a detectable signal in the antenna in the case of a shallow inclination of 0.0 (4.8a), but not in the case of a steeper inclination of 0.4 (4.8b). In light blue the ice sheet is shown confined by bedrock on the bottom (gray) and the atmosphere on the top (white). The Lonely String Detector is shown in red. The orange star indicated the position of particle shower induced by a particle propagating in the direction of the dotted line from left to right. The particle shower has in bot cases the same relative position to the detector string. The Cherenkov cone is depicted as a black dotted line. The colored angles indicate the aperture angle symmetric around the Cherenkov angle in which range the signal is still simulated by NuRadioMC.

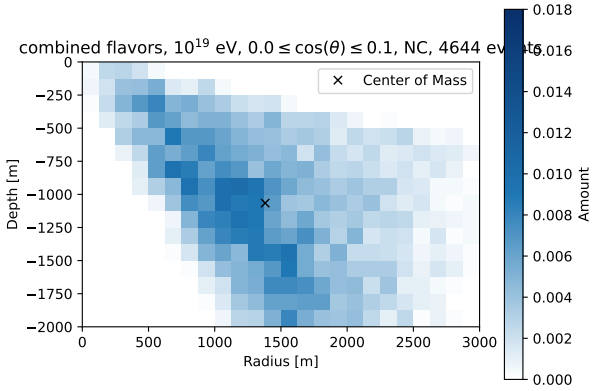

Figure 4.9: Spatial distribution of the primary showers from neutrino NC interactions of differnt flavors that are seen by Channel 0 of the Lonely String Detector. The initial neutrinos have an inclination between 0.0 and 0.1.

is no longer simulated since its amplitude is decreased, since it is no longer coherent. The further away from the cone the weaker the radio signal [4]. It is to note, that this line of argument does not account for ray bending due to the change in the index of refraction. For the indicated vertex position the Cherenkov cone hits the detector string for an inclination of 0.0. Leading to a potentially measurable signal. For the inclination of 0.4 the channels do not even coincide with the $\pm 20°$ angle range. Thus, no rays propagating from the vertex to the channels will be simulated and no showers can be measured at this angle.

Figure 4.9 shows the shower distribution at 10^{19} eV for a combination of electron, muon and tau neutrinos interacting via a NC interaction. Their inclination is set to a range from 0.0 to 0.1. In comparison to CC interactions in Figure 4.6a the center of mass of the showers shifts further away from the antenna. This can be explained by the energy distribution of the showers shown in section 4.1. Since the showers of NC events tend to a higher energy, they can be detected further away.

The difference of the spatial shower distribution in different flavors also mainly stem from different shower energies and shower types. Figure 4.10a shows the spatial shower distribution of electron neutrinos with the same initial energy and inclination interacting via the CC. The center of mass of the position of the showers is even further away from the station for electron neutrinos, since the whole energy of the lepton is put into one shower. These showers with high energies can then be seen from further away.

The spatial distribution for tau neutrinos is shown in Figure 4.10b. Since the showers originating from tau neutrino interactions tend to have higher energies than the showers from muon neutrino interactions the center of mass of the shower distribution is also slightly further away from the detector than for muon neutrinos.

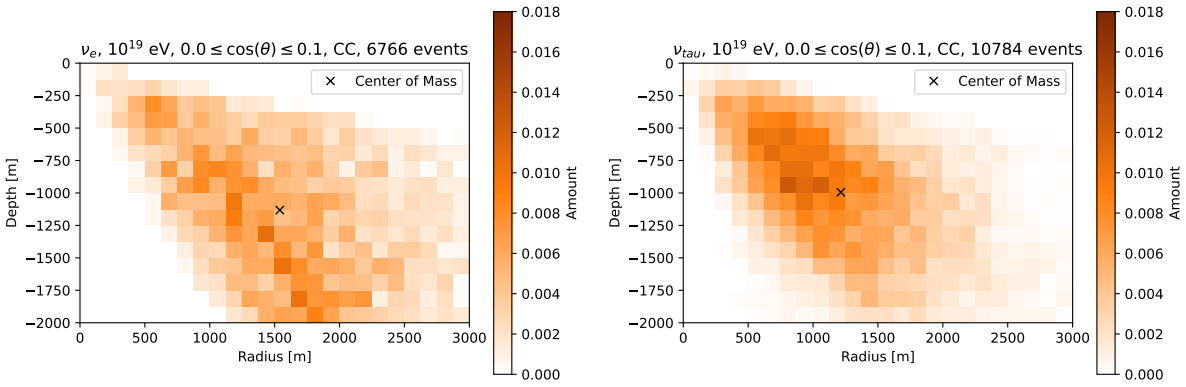

(a) (b)

Figure 4.10: Spatial distribution of the induced showers from neutrino CC interactions that are seen by Channel 0 of the Lonely String Detector. The initial neutrinos have an initial energy of 10^{19} eV and an inclination between 0.0 and 0.1. Figure 4.10a shows the distribution for electron neutrinos and Figure 4.10b for tau neutrinos. The blue cross indicates the balance point of the detected showers.

Chapter 5

Method Development for Flavor Separation

In order to develop a first approach of differentiating neutrino flavors it can be concluded from the previous chapter that the number of of showers in each event can be utilized a possible characteristic. The differentiation between charged current (CC) interaction muon neutrinos and neutral current (NC) interacting neutrinos in general is most promising, since the number of showers shows the largest difference. An energy value of 10^{19} eV is chosen to enhance the observed disparities. In this chapter eight strategies are developed to count the number of signals, induced by the particle showers on the trace. From the number of found peaks, one can conclude back to the number of showers. The strategies are developed on noiseless traces. Figure 5.1 shows two example traces. Figure 5.1a shows a trace of a NC event and Figure 5.1b shows the trace of a CC event. Each plot shows the trace, recorded by the respective channel. In Channel 0, in both cases a relatively large signal at around 1000 ns is present. These are the peaks that triggered the event to be saved. The 1000 ns delay stems from the readout window before the trigger. In doing so, signals that arrive before the triggered on signal are still present in the trace and not cut off. In the less deeper channels the signal arrives earlier. This effect mainly stems from the different cable delays set in the detector file introduced in subsection 3.2.1, resulting in the signals from deeper channels to arrive later. In the NC traces are two signals present in all channels. This is caused by the radio signal from the hadronic shower arriving at the antenna via a direct path and a reflected or refracted path as explained in section 2.4. Since the higher channels are closer to the surface the difference in time of flight decreases which reduces the time difference of those signals until they almost arrive simultaneously in the uppermost channel. In this example in the traces of the CC event three signals are apparent in channel 0 to 9 and two signals in channel 10. Since additional showers are produced by secondary leptons in CC interactions more than two peaks can be measured. This feature can now be used: By counting the number of signals, one can try to distinguish between NC and CC events. To obtain a more robust parameter, the number of found peaks in the traces can then be summed up and compared against a cut value to select CC from NC events.

In the following different strategies to identify and count the signals in the trace will be explained and discussed. The method was developed and optimized on the simulated data set of muon neutrinos with an energy of 10^{19} eV and an inclination of $\cos(\theta)$ between 0.0 and 0.1. All presented plots in this chapter show these parameters.

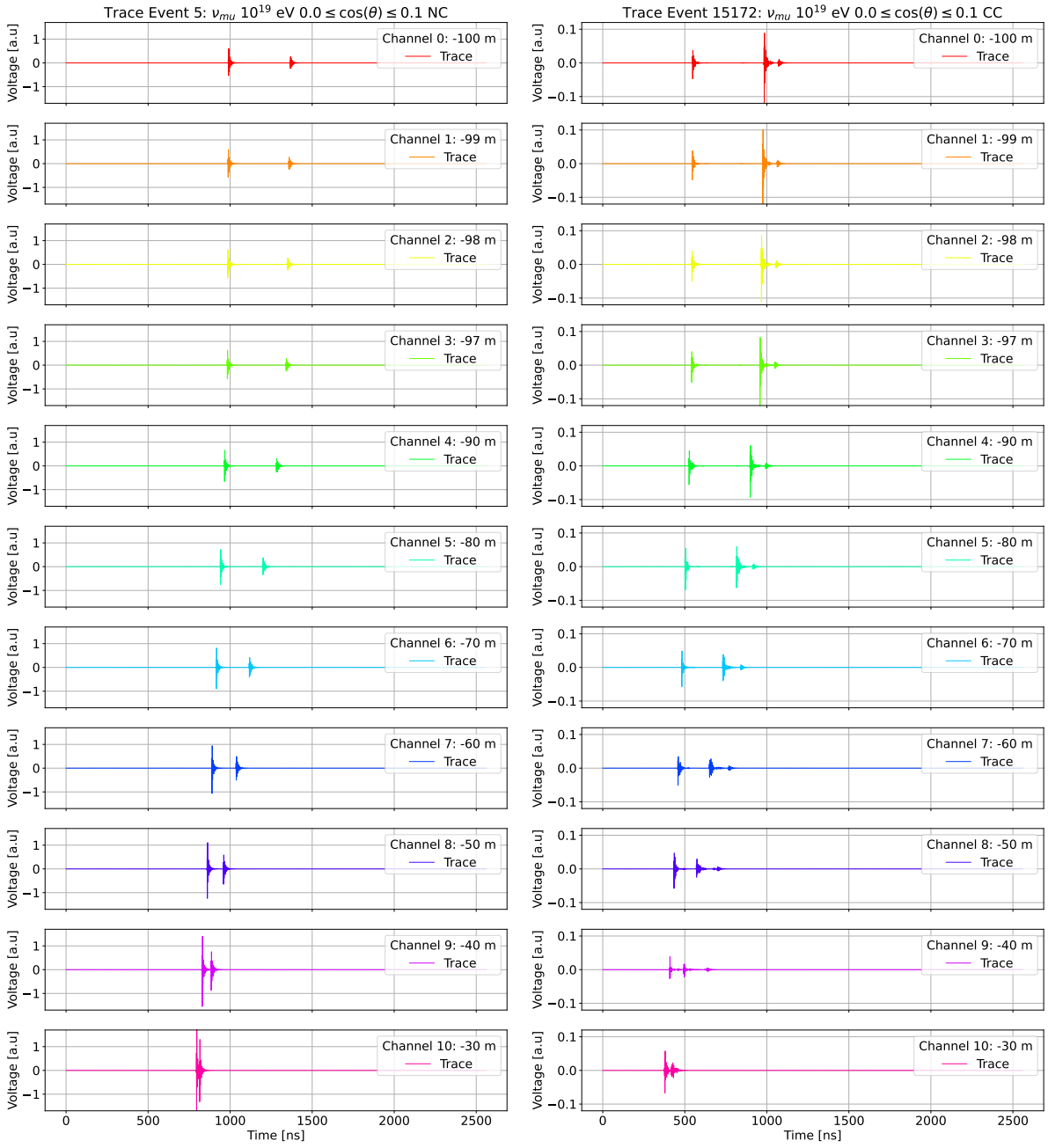

(a) (b)

Figure 5.1: Example traces in the eleven simulated channels of an interacting muon neutrino. No noise was simulated on these traces and several distinct signals are visible in each trace. Figure 5.1a shows traces of a noiseless NC event, where exactly two signals are present in each channel. In Figure 5.1b the traces of a noiseless CC event have more than two signals per trace.

.

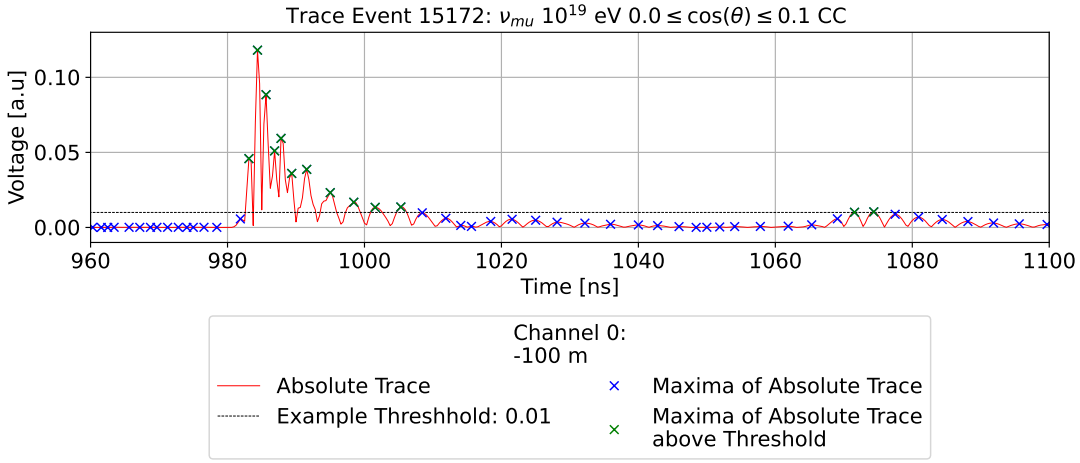

Figure 5.2: Example of Strategy 1 to detect peaks on the trace. The absolute value of the trace is shown in red. The maxima on the trace were determined (blue crosses). The height of the maxima are compared against a threshold, shown as a black dotted line. Consecutive maxima above the threshold, shown in green are counted as a found peak. On this trace two peaks were found.

5.1 Strategy 1: Simple Peak Detection

Figure 5.2 shows a zoomed-in section of the CC event trace in Channel 0 shown in Figure 5.1b. Here the absolute of the trace is shown. This part contains two signals. One with a maximum at around 985 ns and a smaller one at 1070 ns. The oscillating part of the signal manifests itself in the bumpy structure of the signal. In a first attempt to identify a peak to count it as an individual signal a threshold of 0.01 is defined, shown in Figure 5.2 as a black dashed line. Due to the periodic nature of the signal, some sampling points of the trace undercut the threshold, even when the local maxima still succeed the threshold. This is why the Peak-finding algorithm implemented in the python package SciPy [52] scipy.find_peaks was used to detect local maxima of the absolute trace. The found local maxima are indicated as crosses. Maxima indicated in blue lie below the threshold and maxima indicated in green above. Consecutive peaks above the threshold compose one signal. Here, there are two.

The number of detected signals depends on the selected value of the threshold. If the threshold is chosen to high, small signals will not surpass it. If the threshold is chosen too low, individual sampling points might surpass it and distort the final count. Additionally, close signals might be counted as one. The choice of the threshold is therefore elementary for obtaining the correct amount of peaks to be able to distinguish NC from CC events. Unfortunately, there is no way to determine the threshold a priori. For this reason, a threshold scan for values between 10^{-4} and 1 in arbitrary voltage units on a logarithmic scale has been performed. In the following the threshold is shown in multiples of sigma noise corresponding to $V_{RMS} = 0.0117$ of the noise as calculated in chapter 3. This is useful to compare the trigger values with regards to thermal noise on the trace. Strategy 1 was applied on both muon neutrino data sets. Figure 5.3 shows the distribution of number of found peaks for each investigated threshold as a heat map. Figure 5.3a shows the distribution for the NC events and Figure 5.3b for the CC events. On the x-axis the threshold is given in multiples of sigma noise over four orders of magnitude on a logarithmic scale. On the y-axis the number of detected peaks with Strategy 1 is shown.

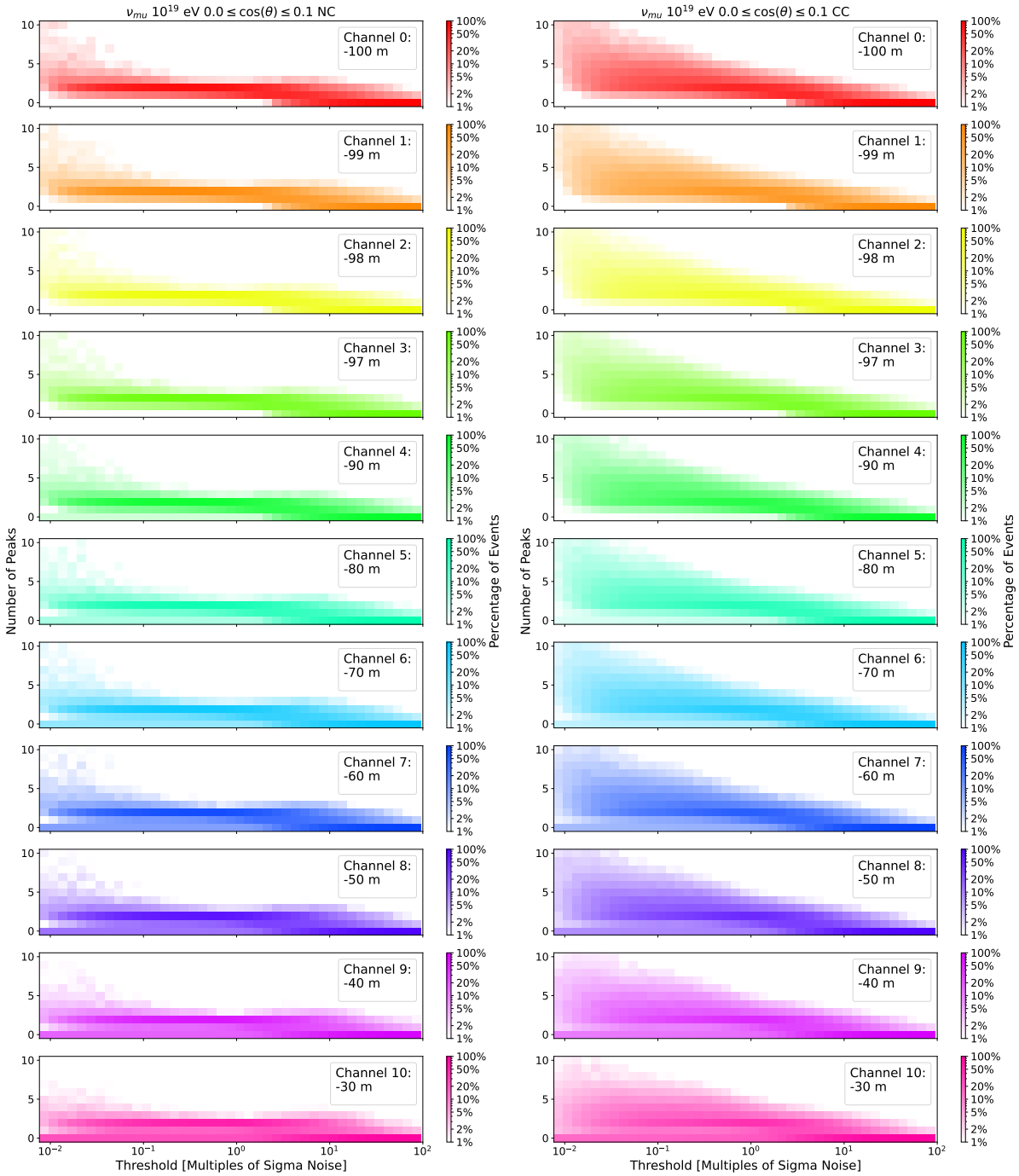

(a) (b)

Figure 5.3: Heat map of the distribution of the number of identified peaks on the y-axis. On the x-axis several investigated thresholds are shown on a logarithmic scale. The color intensity corresponds to the amount of events with this number of found peaks on a logarithmic scale for better visibility of the important features. Figure 5.3a shows the distribution for NC events, where only rarely more than two peaks are identified. Figure 5.3b shows the the same distribution for CC events, where with decreasing threshold more events with several found peaks exist.

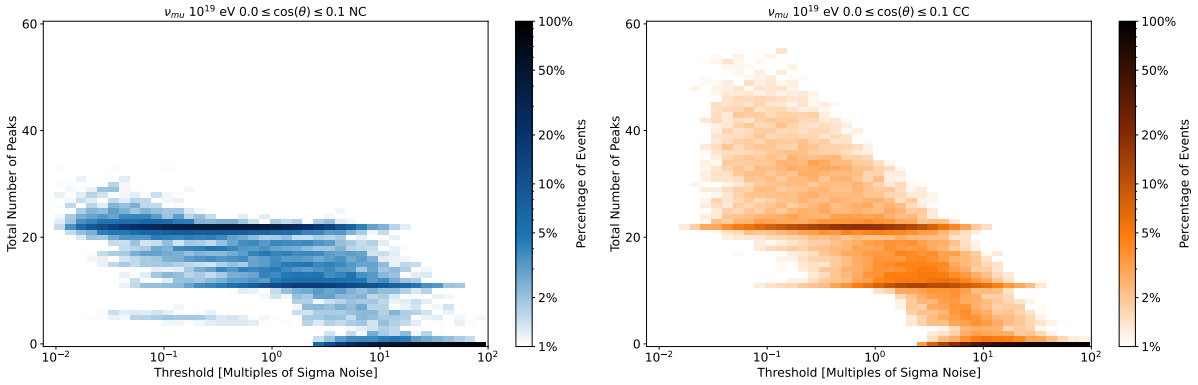

(a) (b)

Figure 5.4: Heat maps showing the distribution of the total number of found peaks in all eleven traces of an event. On the x-axis the threshold is shown logarithmically and on the x-axis the number of total found peaks. The color bar is again shown on a logarithmic scale to visualize important features of the distributions. Figure 5.4a shows the distribution for NC events, where only rarely events with more than 22 peaks are detected. Figure 5.4b shows the distribution of CC events, where several events show more than 22 peaks at medium investigated thresholds.

The color intensity indicates the fraction of events in this bin. For a better visibility of the important features the color intensity is on a logarithmic scale. The sum over one column of the color plot is supposed to be 100% but the range of shown number of peaks is limited. At high thresholds, only very rarely a peak get detected: The number of peaks is mostly 0 in all channels for both NC and CC interactions. When the threshold is decreased single peaks are recorded more often and the distribution shifts to one and two peaks. For the NC events the distribution plateaus at two with rare occurrences of three peaks for medium thresholds, while the CC events show a more broader distribution over higher number of peaks. At the smallest thresholds the distribution is so widespread, that it seems to fade due to the low number of entries in each bin. At this point the number of detected peaks is arbitrary due to the noise introduced by the limited sampling rate. In Channel 0, at thresholds smaller then two times the sigma noise,there will always be at least one detected peak, namely the one the event was triggered on. For higher channels the distribution is tilted towards less peaks: it becomes more likely, that no peaks are found. The signal of an interaction reaching Channel 0 does not necessarily reaches the upper channels as well. The further away a channel is placed from Channel 0 the less likely it is to also see the signal. The number of found peaks can now be summed up for each event over the eleven channels. Figure 5.4 shows the distributions of the total number of peaks for NC events in Figure 5.4a and for CC events in Figure 5.4b. Conspicuous are the three dominant lines where zero, eleven and 22 peaks were detected. This stems from the fact, that the signals in the different channels are similar in amplitude and are usually present in all eleven channels as can be seen in Figure 5.1. If a lowered threshold intersects with a signal in one channel, it will most likely do so in the other channels as well. Therefore the number of total peaks gets increased by eleven.

When comparing the distribution of the NC and CC events above the 22 bins, the distribution of the CC events is wider spread to higher bins, while 22 is a harder limit for NC events at medium thresholds. Only for the lowest thresholds the NC events also provide a prominent amount of summed peaks over 22. Each shower in an event produces up to two signals in the trace: one arriving via the direct and one via the indirect path. An

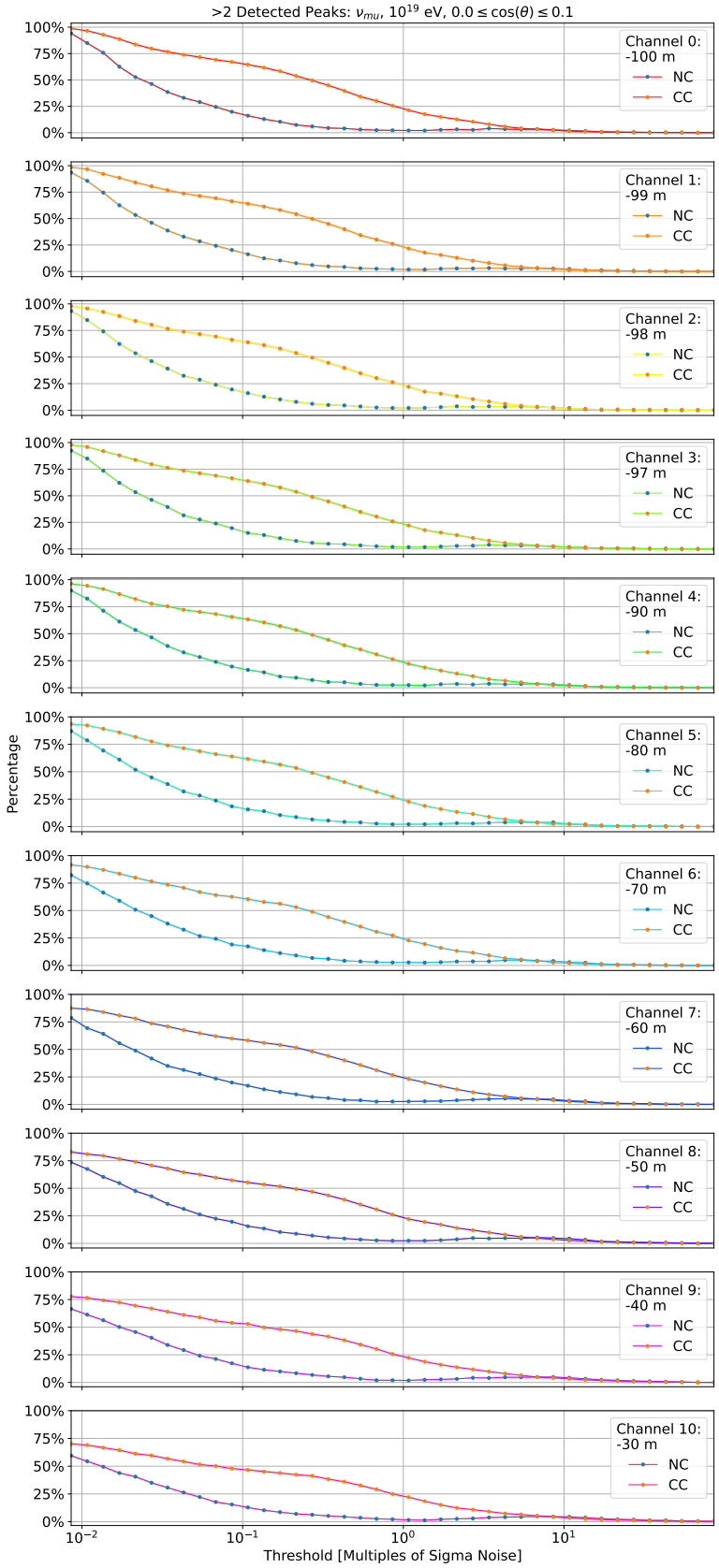

Figure 5.5: Amount of events where more than two peaks were found on the trace for each of the eleven channels with Strategy 1. In blue the percentage of the NC events and in orange the percentage of the CC events are shown with an 1σ confidence band.

event with N showers results in up to $2 \cdot 11 \cdot N$ showers, assuming a ray tracing solution was found from each shower to each channel. Thus the sum of all peaks found in an event with more than one shower would be more than 22.

To compare the classification capabilities of this method, Figure 5.5 shows the percentage of events that fulfill the condition of more than two detected peaks. In blue the NC events and in orange the CC events are shown over the respective threshold. We denote N_j as the total number of investigated events in a channel j. N_j is the same for all channels. The value is given in Table 3.2. $N_{j,>2}$ is the number of events in channel j where more than two peaks were found. Figure 5.5 shows the percentage of events with more than two peaks $\frac{N_{j,>2}}{N_j}$. Since each event either has more than two peaks or not, the value of $N_{j,>2}$ for a certain threshold follows a binomial distribution. Thus, the standard deviation of $N_{j,>2}$ is [53]:

$$\sigma_{N_{j,>2}} = \sqrt{N_j \cdot \frac{N_{j,>2}}{N_j} \cdot (1 - \frac{N_{j,>2}}{N_j})} \tag{5.1}$$

Using Gaussian error propagation, the standard deviation of the proportion is $\frac{\sigma_{N_{j,>2}}}{N_j}$ and shown in Figure 5.5 as a confidence band.

For high thresholds this fraction is zero, since no peaks are found. When the threshold decreases, more and more peaks are found. At first the percentage of NC and CC events rise similarly up until about 10%. The percentage of the NC events decreases again and stays below 25%, even for small thresholds of 10^{-1} multiples of sigma noise, before rising up to 100% at the smallest thresholds. The local maximum at high thresholds is more pronounced in higher channels, where the NC events even surpass the NC events. In comparison the percentage of CC events rise faster with declining threshold and approaches a fraction of 100% more shallowly. The curve characteristics are overall very similar in all eleven channels: At a threshold of 1 multiples of sigma noise around 25% of muon neutrino CC events get correctly classified as such, while less than 5% of the NC events are falsely identified as CC muon neutrinos.

Figure 5.6 shows the percentage of events with more than 22 total peaks over the threshold, but for the sum of found peaks. The amount of more than 22 peaks stays near zero for high thresholds. For lower thresholds the percentage rises both in NC and CC events. The NC process has a local maximum of $(7.8 \pm 0.7)\,\%$ at 3.41 multiples of sigma noise. At 0.86 multiples of sigma noise it reaches a local minima of $(5.2 \pm 0.6)\,\%$, before steeply increasing to almost 100%. The local maximum and minimum are not present in the progression of the CC events. At a threshold of 2.2 multiples of sigma noise, which is close to the expected $2\sigma_{noise}$ trigger efficiency of RNO-G [10], $(21.1 \pm 0.6)\,\%$ of the events are correctly identified as charged current events, but $(6.7 \pm 0.7)\,\%$ of the NC events are wrongly identified as CC events.

To improve on this method NC event where more than two peaks were detected were investigated. It is observable, that in some cases single maxima lie below the threshold and thus interrupting the sequence of consecutive maxima of one signal which leads to a single signal being counted as two. An example of this is shown in Figure 5.7, where a found maximum at 1607 ns undershoots the threshold. The third found peak is located

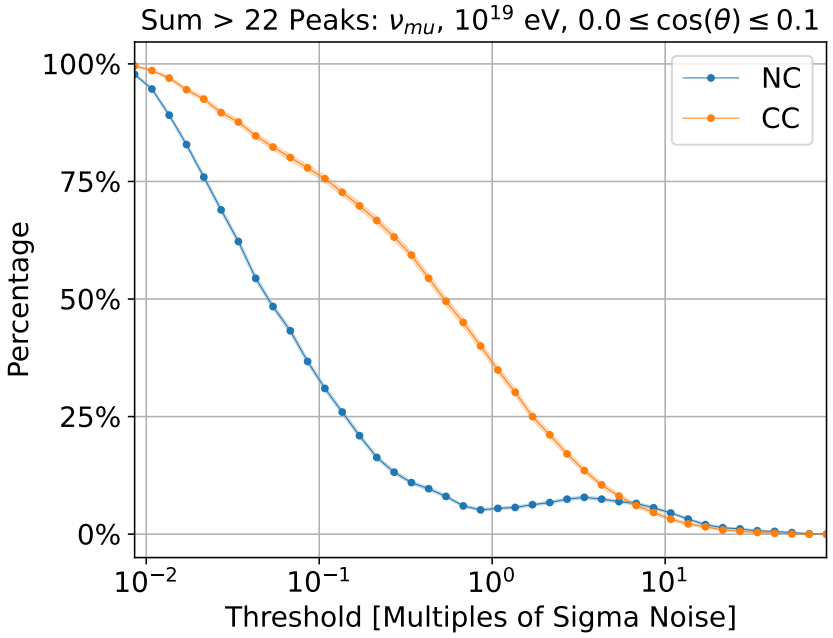

Figure 5.6: Amount of events, where the total number of found events with Strategy 1 in all traces is greater than 22. In blue the results of the NC events and in orange the results of the CC events are shown with their 1σ confidence band.

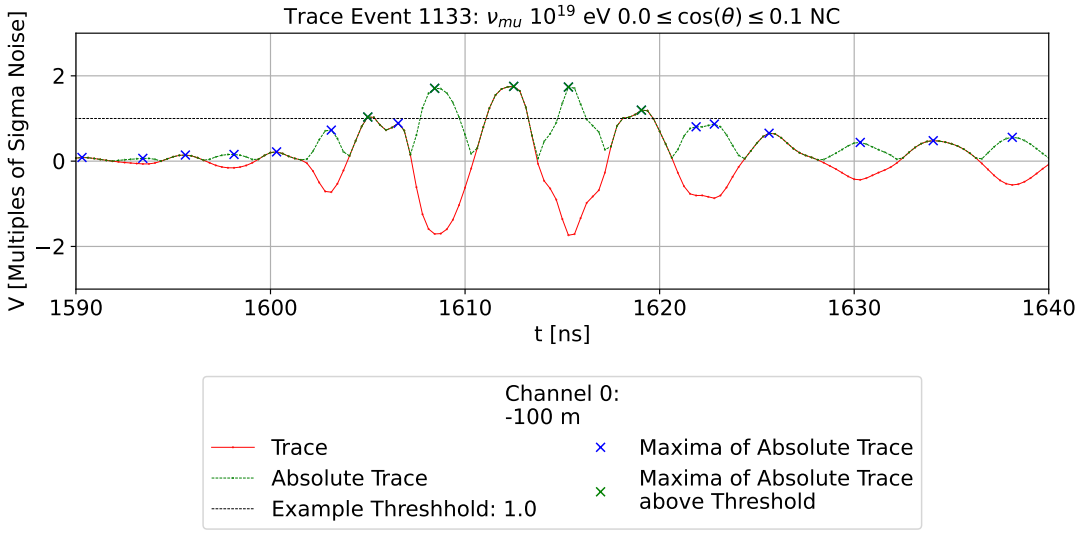

Figure 5.7: Example of a trace, where Strategy 1 lead to unwanted results. The trace is shown in red and its absolute as a dashed green line. The found maxima on the absolute of the trace are shown as crosses. Some of them surpassing the threshold shown as a black dotted line shown in green. Since the found maximum at 1607 ns undercuts the threshold this signal is falsely counted as two peaks.

outside of the plotted area. This happens due to phase shifts of the trace. In the example trace this is visible at 1607 ns , 1615 ns and also at 1622 ns. This explains the local maxima for the NC events in Figure 5.6. If the threshold in Figure 5.7 would be higher the maximum at 1605 ns would not make the cut and only one peak would be counted in the shown range. If the threshold would be lower, at some point all consecutive maxima lie above it and again only one peak is counted. For thresholds in between the counting is off. This also happens for CC events, but since the total amount of events with more than 22 peaks is increasing due to the additional found signals, a local maximum does not manifest in Figure 5.6 but disperses in the steep inclination.

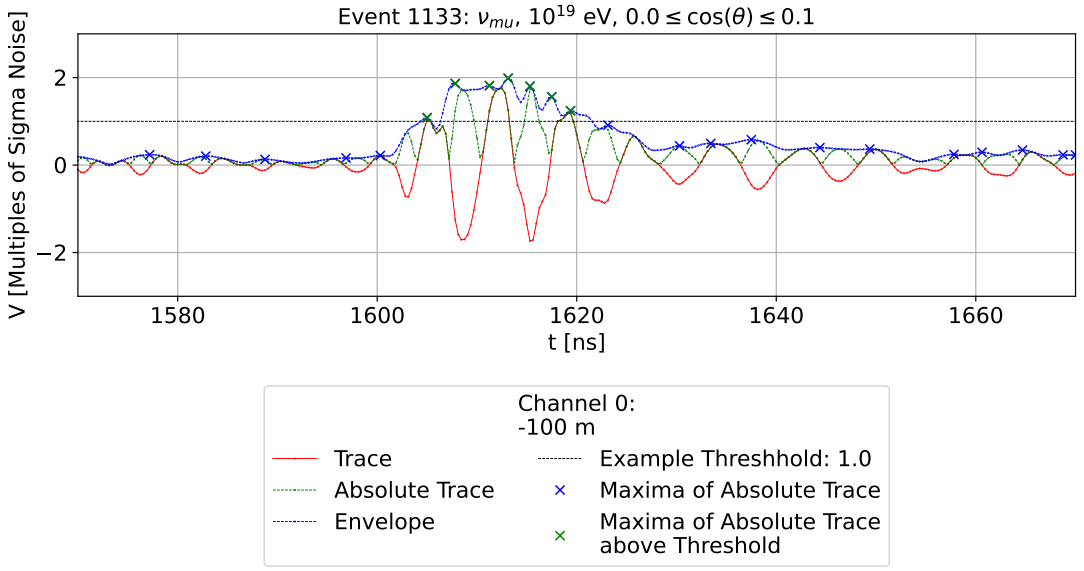

Figure 5.8: Strategy 2.1 applied to the trace shown previously in Figure 5.7. Additionally, to the trace (red), the absolute trace (dotted green) and threshold line (dashed black), the envelope of the absolute trace is shown as a dashed blue line. The maxima of the envelope are indicated as crosses.

5.2 Strategy 2: Peak Detection on Envelope

5.2.1 Strategy 2.1

To tackle the issue of single trace maxima undercutting the threshold, in Strategy 2 the absolute envelope of the signal is used. Therefor the Scipy function scipy.hilbert [52] was used to calculate the Hilbert envelope. In Strategy 2.1 the maxima of the envelope were determined as for the trace in Strategy 1 using scipy.find_peaks. Figure 5.8 shows the same event as Figure 5.7 but with Strategy 2.1 applied to it. The additional local maxima below the threshold at 1507 ns disappears and the maxima are consecutive over the whole signal resulting in one found peak. Figure Figure 5.9 shows the percentage of events having more than 22 found peaks with Strategy 2.1. Comparing it to Figure 5.6, the local maximum of the NC events at high thresholds disappeared. At a threshold of 2.2 multiples of sigma noise the correct classified CC events are at $(4.9 \pm 0.4)\,\%$ and $(0.3 \pm 0.2)\,\%$ of the NC events are classified as CC events. This strategy is therefore an improvement to obtain an ideally pure muon neutrino selection. The percentage of selected CC events is also slightly reduced at these thresholds compared to Figure 5.6. This is reasonable, since the same effect of twofold counted signals happens for CC events

While further investigating NC events where more than two signals were detected, small deviations in the envelope still lead to some maxima undercutting the threshold or accordingly some maxima exceeding the threshold. An example is shown in Figure 5.10, where at 1027 ns a single maximum undercuts the threshold. These effects mainly happen during the decay of the signal.

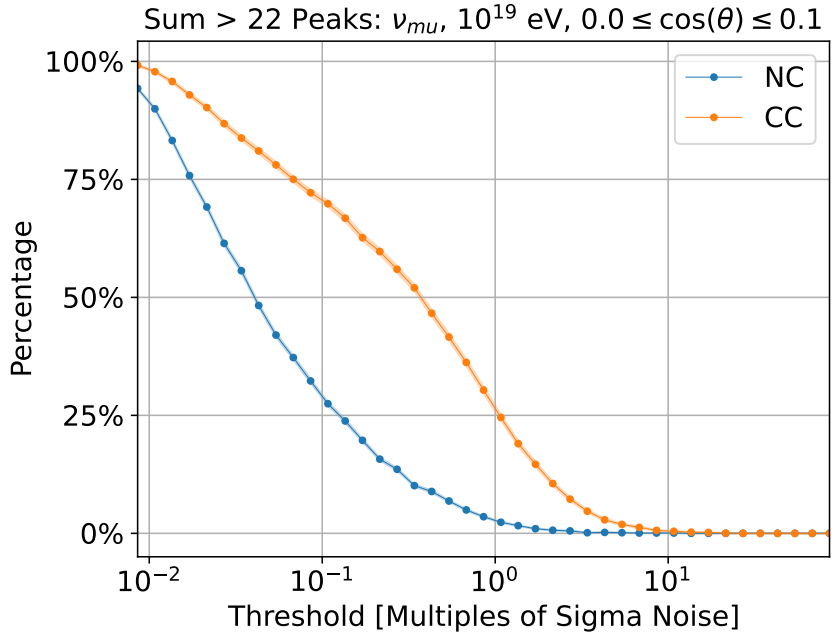

Figure 5.9: Amount of events, where the total number of found events with Strategy 2.1 in all traces is greater than 22. In blue the results of the NC events and in orange the results of the CC events are shown with their 1σ confidence band.

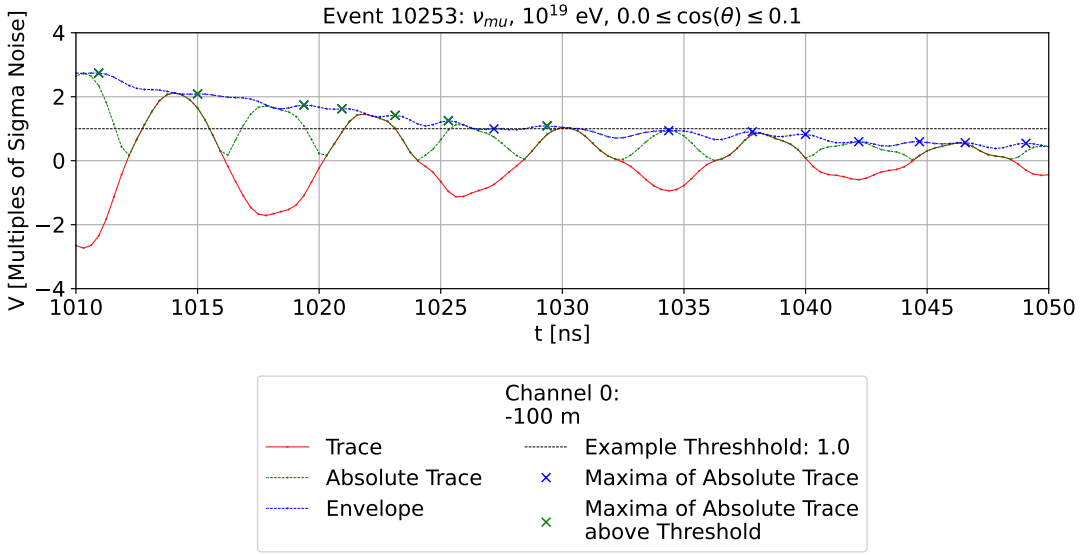

Figure 5.10: Example of trace where Strategy 2.1 leads to unwanted results. In red a section of a trace recorded in Channel 0 is shown. Its absolute value is shown as a green dashed line and the envelope is shown as a blue dashed line. Crosses indicate the found maxima on the envelope. The maximum at 1027 ns undercuts the threshold shown as a black dashed line, while both its neighboring maxima are larger. Thus, two peaks are counted.

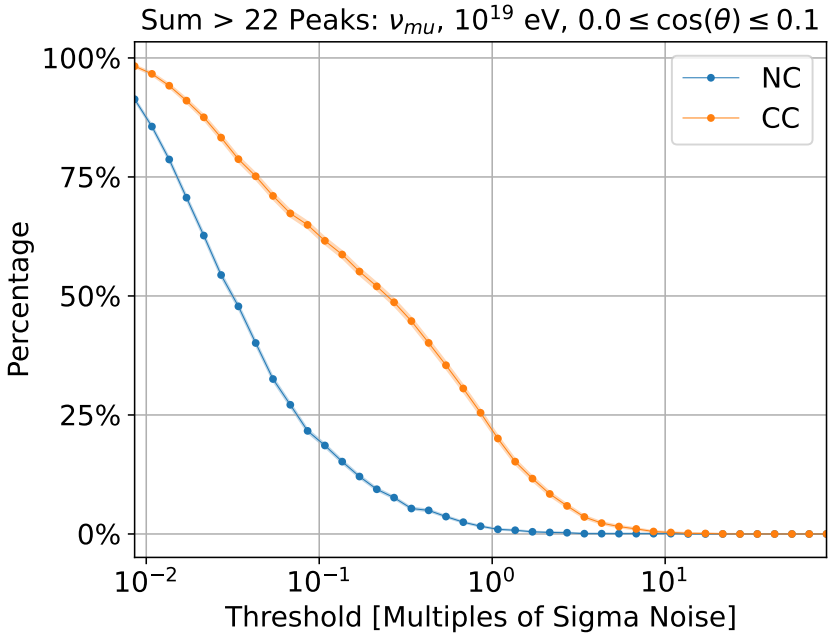

Figure 5.11: Amount of events, where the total number of found events with Strategy 2.2 in all traces is greater than 22. In blue the results of the NC events and in orange the results of the CC events are shown with their 1σ confidence band.

5.2.2 Strategy 2.2

Strategy 2.2 tries to improve on this technique by demanding at least two maxima below the threshold before counting an interrupted series of maxima as two peaks. The trace shown in Figure 5.10 therefore contains only one peak, when Strategy 2.2 is applied to it. Figure 5.11 shows the percentage of events with in total more than 22 detected peaks over the threshold. Compared to Figure 5.9 in both NC and CC events less events fulfill this criterion. At a threshold of 2.2 multiples of sigma noise the NC events decreased to $(0.1 \pm 0.1)\,\%$, while the CC events dropped to $(3.9 \pm 0.3)\,\%$. Strategy 2.2 thus leads to a more pure selection of muon neutrino CC events, but with the trade off of even less efficiency. The performance of the different strategies will be compared and discussed in chapter 6 in detail. Unfortunately, this strategy also rejects some of the CC events, where three peaks are present. This is shown in Figure 5.12, where the third signal is located outside of the plotted area. Here, only one maxima, which is located at 981 ns, lies between two individual signals, thus both signals being counted as one peak.

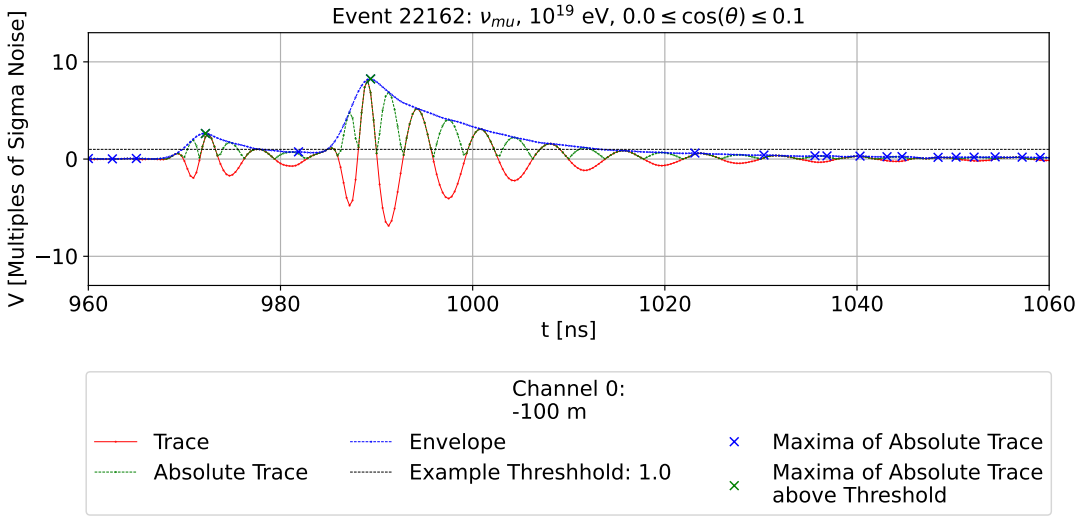

Figure 5.12: Example of a trace where Strategy 2.2 does lead to unwanted results. In red the trace of an event in Channel 0 is shown. Its absolute value is shown as a green dashed line and the envelope of the trace is shown as a blue dashed line. The trace shows two apparent signals. On the envelope two corresponding maxima at 972 ns and 989 ns are found. In between only one maxima at 981 ns is present, leading to Strategy 2.2 interpreting the two signals as one peak.

5.2.3 Strategy 2.3

In a next step the maximum amplitude of the traces is investigated. Figure 5.13 shows the distribution of the maximum amplitude of the investigated events, i.e the amplitude of the highest signal. The distribution is shown for each of the eleven channels in a separate plot. In blue the distribution of the NC events and in orange the distribution for the CC events is shown. The uncertainty for each bin i of the channel j showing the percentage $p_{j,i} = \frac{N_{j,i}}{N_j}$ of all events in the channel N_j in the respective amplitude range has been calculated. The standard deviation of number of events can be calculated analogous to Equation 5.1, yielding

$$\sigma_{p_{j,i}} = \frac{\sigma_{N_{i,j}}}{N_j} = \frac{\sqrt{p_{j,i}^2 N_j (1 - p_{j,i}^2)}}{N_j}. \tag{5.2}$$

The shape of the distribution is similar in NC and CC events in each channel. In Channel 0 the distribution is sharply cut at 2 multiples of sigma noise, since this is the trigger threshold and signals with less amplitude are rejected. The vertical line indicates the mean amplitude in each channel, which does not change noticably for the CC events. The upper the channel the broader the distribution, spreading over several orders of magnitudes. This makes it difficult to find one threshold, which is able to count small signals and avoid counting two close high amplitude signals. This provokes the idea the normalize the trace to its maximum value. Assuming, the ratio between peak heights is less spread. For Figure 5.14 peaks were detected using Strategy 2.1 with a threshold of 1 multiples of sigma noise. The maximum of the Hilbert envelope of each detected peak was determined. The solid bar plots show the fraction of the second largest found peak to the largest found peak for the NC events in blue and CC events in orange. For the CC events the third largest peak was determined as well if it is present. Its ratio to the largest peak is shown as an orange dashed line. The distribution is normalized to the total number of events, resulting in a cumulative sum of < 1, if no second or third largest peaks was found. Thus, the histogram of the third largest to largest peak is in total lower, since not for all events a third peak has been found.

While it looks promising that in all cases over 90 % of the ratios lie in between less than two orders of magnitude, that in only about 65 % of the events a second peak was detected. If the maximum amplitude is determined to be 1 multiples of sigma noise the second largest peak will not be fount with a threshold of this value skewing the results. It is therefore not possible to assess the benefits of this method deductively. However it is worth noting, that the maximum of the distribution shift to higher values for higher channels. This could be explained with a lower maximum amplitude, but that would contradict the findings in Figure 5.14, where the mean amplitude stays the same for all channels. The other explanation is the second largest signal having a higher amplitude in higher channels compared to the ones in the lower channels. This scenario is more plausible since, in the case of NC events, both signals stem from the same shower. The second signal stems from the indirect path of the radio waves propagating through the ice as shown in Figure 2.4. For the upper channel the difference in propagation distance between the direct and the indirect path is smaller, thus the attenuation though the ice is generally less different and the signals are more similar in height.

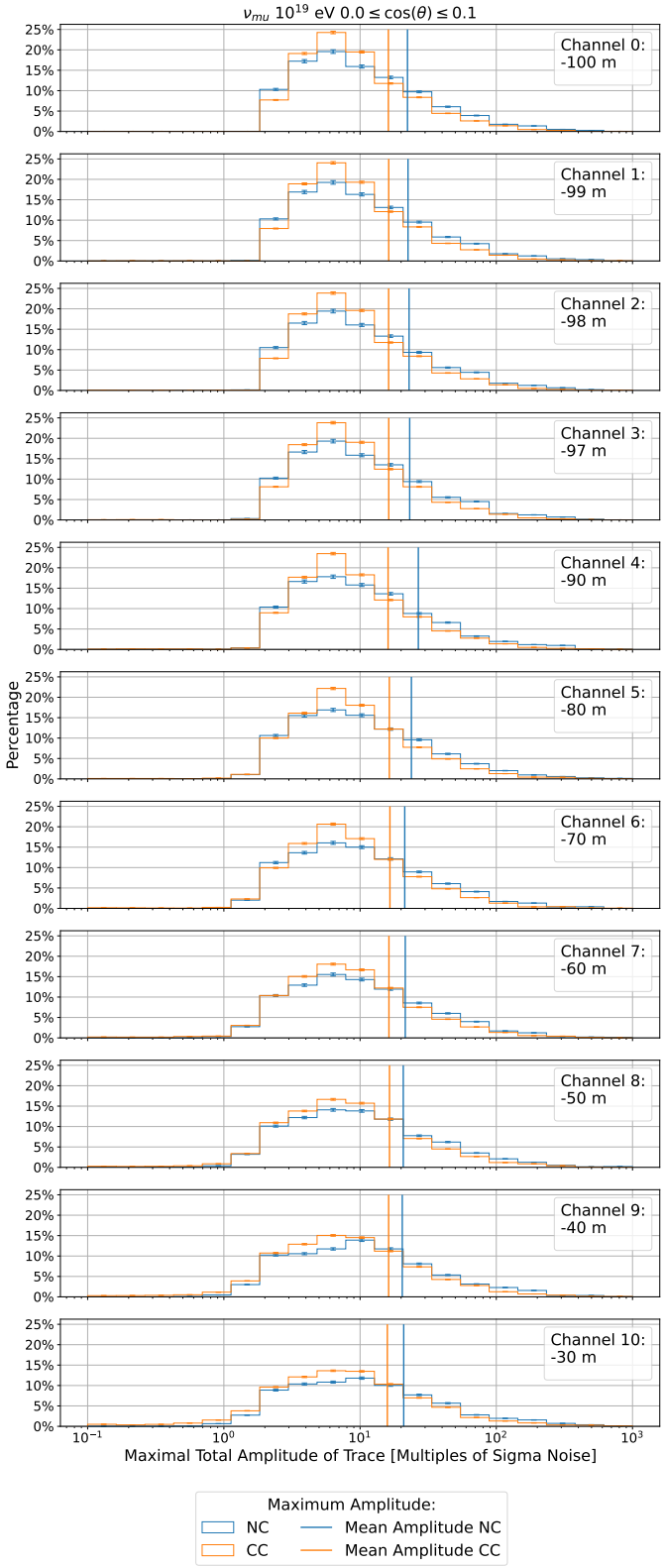

Figure 5.13: Histogram of the maximum amplitude value in the traces for each channel. On the x-axis the amplitude of the maximum amplitude is shown. On the y-axis the percentage of events in each bin is shown. In blue the distribution for NC events and in orange the one for CC events are shown. The error bars on the bars of the histogram show 1σ uncertainties. In each plot, two vertical lines indicate the mean maximum amplitude for NC events in blue and for CC events in orange.

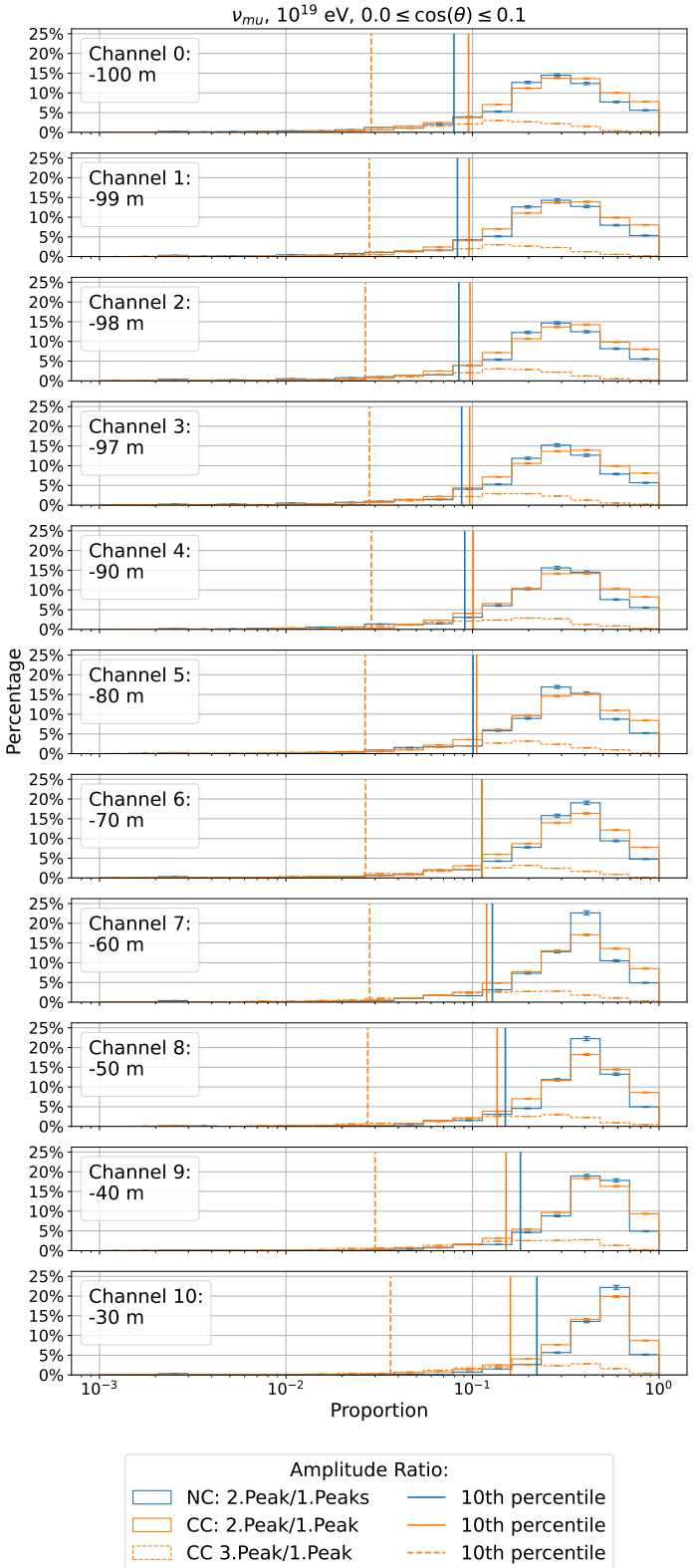

Figure 5.14: Histogram of the ratio between the second largest found peak to the largest found peak as solid lines and third largest to largest peak as a dashed line for all eleven channels. The peaks were detected using Strategy 2.1 with a threshold of 1 multiples of sigma noise. The error bars indicate the 1σ uncertainties. In blue the results of the NC event and in orange the results of the CC events are shown. The vertical lines in the plot indicate the tenth percentile of the histogram.

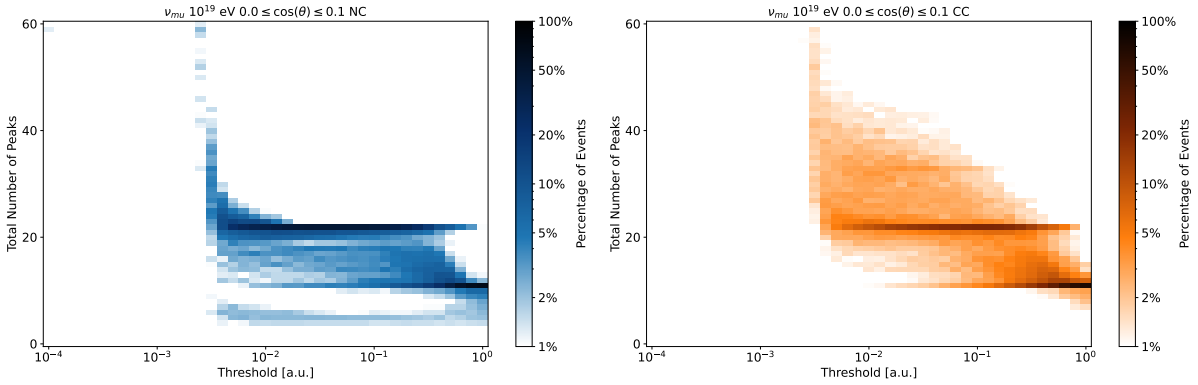

(a) (b)

Figure 5.15: Heat map of the total number of found peaks with Strategy 2.3 summed over all eleven channels for different investigated thresholds shown on the logarithmic x-axis. The y-axis shows the total number of found peaks. The color bar is shown on a logarithmic scale to visualize the important features of the distribution. Figure 5.15a shows the heat map for NC events and Figure 5.15b for CC events.

For Strategy 2.3 before applying the Hilbert envelope and the peak finding algorithm, the trace is normalized to its maximum amplitude. The required maxima undercutting the threshold to separate two peaks is specified to one again. The threshold no longer corresponds to multiples of sigma noise, since the normalization is different for every trace. It is now given in arbitrary units between 10^{-4} and 1.

Figure 5.15 shows the distribution of total number of peaks over the threshold for Strategy 2.3 as shown before for previous strategies. One would expect, to obtain at least one peak in each channel, since the trace is normalized to its maximum and the threshold is $<= 1$. Apparently, this is not the case. For individual events the sum of found peaks is below 11. That is because in rare cases the upper channels do not detect any showers and the simulated trace is 0 over the whole trace. Thus, the normalization of the the trace fails and no peaks are detected. The difference in the NC and CC distributions above 22 peaks is clearly visible. For the CC events additionally to the pronounced concentration at eleven and 22 events a faint accumulation can be seen even at 33 events, where in all eleven traces three peaks were found. In contrast to Figure 5.4, where the distribution is fading for small thresholds since the total number of events is spread out, in this case the total number of events is spread out, but still visible. Since the peaks are normalized, not only the maximum peak height is the same for all events, but also the reverberations of the signal are of similar size, leading to a similar increase of number of events, resulting in a steep visible increase of numbers of events for smaller thresholds. Below a threshold of 10^{-3} the number of events are rather outside of the plotted range than spread out below visible percentages. The performance of Strategy 2.3 is shown in Figure 5.16. Characteristic for this method is the low amount of misclassified NC events at high thresholds, steeply increasing for lower thresholds. The number of events with more than 22 peaks increases steadily with decreasing threshold for CC events. At a threshold of 0.32 multiples of sigma noise $(11.6 \pm 0.5)\,\%$ of the CC events have more than 22 detected peaks and $(0.1 \pm 0.1)\,\%$ of the NC events. Compared to Strategy 2.2 at the same amount of falsely identified NC events the true positive rate increased from $(3.9 \pm 0.3)\,\%$ to $(11.6 \pm 0.5)\,\%$.

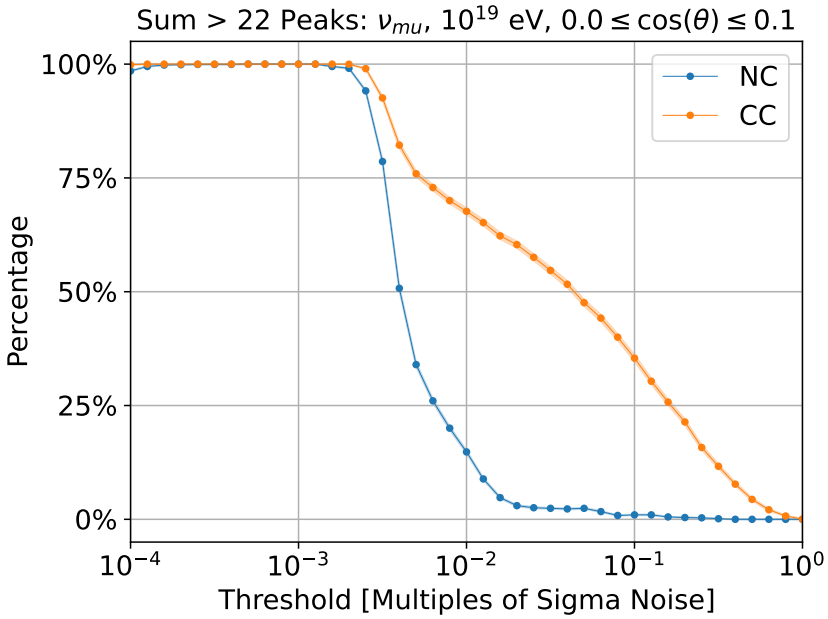

Figure 5.16: Amount of events, where the total number of found events with Strategy 2.3 in all traces is greater than 22. In blue the results of the NC events and in orange the results of the CC events are shown with their 1σ confidence band.

5.3 Strategy 3: Peak Detection on Convolution

In reality the measured traces will contain noise from the surrounding environment and electronics as explained in subsection 3.2.1 and subsection 3.2.2. The effects of noise are shown in Figure 5.17. In the first plot the noiseless trace of a CC event is shown. The trace of the same event with simulated thermal noise on it is shown in the third plot. In total three peaks of different amplitudes are present: at 1000 ns, 1430 ns and 1460 ns. While the largest signal is still visible in the noisy trace, the second largest peak disappears in the noise and can not be identified by its amplitude alone. The second and fourth plot show, the in the following developed, Strategy 3.1 on it. They will be discussed later. To address this issue the whole waveform can be used to identify the signals. The characteristics of the waveforms as seen for example in Figure 5.12 can be described by an sinusiodial osciallation with decreasing frequency, with a poissonian-shaped envelope. This form is rather complicated to approximate and stems from the response of the detector, due to the antenna response, filters and amplification. Instead of approximating this signal shape directly, the incoming electric field traces arriving at the channels are investigated, approximated and then used to obtain a one-fits-all signal shape, that can be used further to filter signals by convolution.

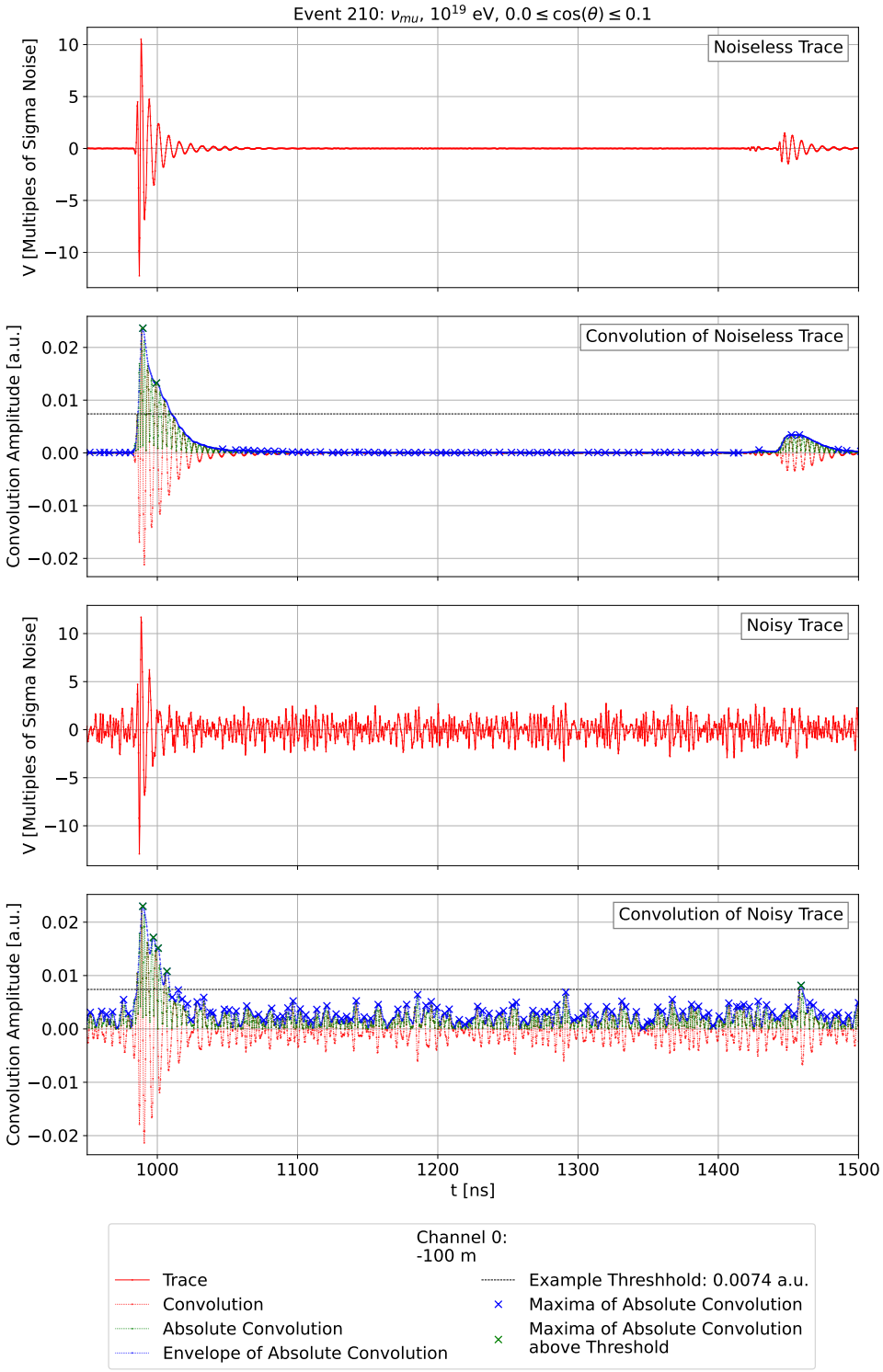

Figure 5.17: Example of a trace in Channel 0 with three peaks. The upper plot shows the noiseless trace of a CC event. The second plot shows the convolution of the determined template with the noiseless trace as a red dashed line. The absolute convolutions is shown as a green dashed line and the envelope of the convolution is shown in blue. The maxima of the envelope are shown as crosses. At the shown threshold of 0.0074 in black only the first signal is identified as a peak. The third plot shows the trace of the same event but with thermal noise applied to it. The lowest plot shows the convolution of the determined template with the the noisy trace. At the set threshold of 0.0074 shown in black, the two largest signals are detected as peaks.

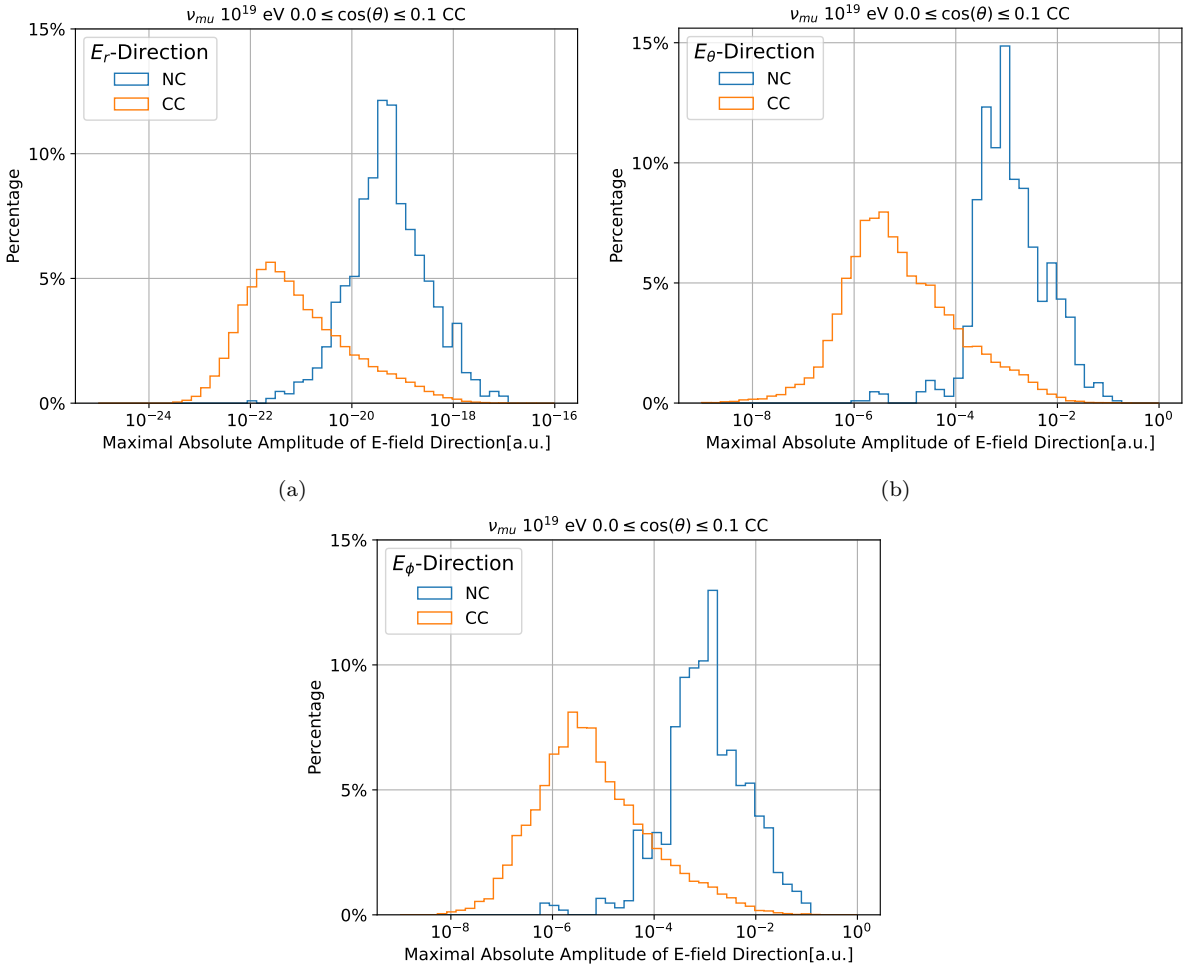

Figure 5.18: Maximum Amplitude distribution of the electric field traces arriving at all channels in R(5.18a) ,θ (5.18b) and ϕ(5.18c) direction as described in the text. Each plot shows the distribution for electric field traces stemming from showers originating from an initial NC interaction (blue) or CC interaction (orange).

In a fist step the electric field traces, that arrive at the channels is investigated. Therefor an independent simulation set of muon neutrinos with an energy of 10^{19} eV and an inclination of $0.0 \leq \cos(\theta) < 0.1$ was used as mentioned in section 3.3 to avoid later overfitting of the data. NuRadioReco [37] simulates the electric field trace from an arriving shower at each channel. Each shower has a component in R, θ and ϕ direction of the shower, where R is the direction between the antenna and the shower maximum. The θ component gives the amplitude of the electric field perpendicular to the R component, and lies in the plane defined by the shower axis and the antenna. The ϕ component goes in the direction of the cross product of R and θ. Despite the naming, the electric field is not given in spherical coordinates [54].

Figure 5.18 shows the distribution of the maximum amplitude of the electric field traces over all channels. We will use one template for all channels, since the antennas and electronic are technically equivalent and the arriving electric pulses are similar over all channels, which will be verified later. Each plot shows the maximum amplitude distribution in either R-, θ- or ϕ-direction. The more energy a shower has, the more secondary

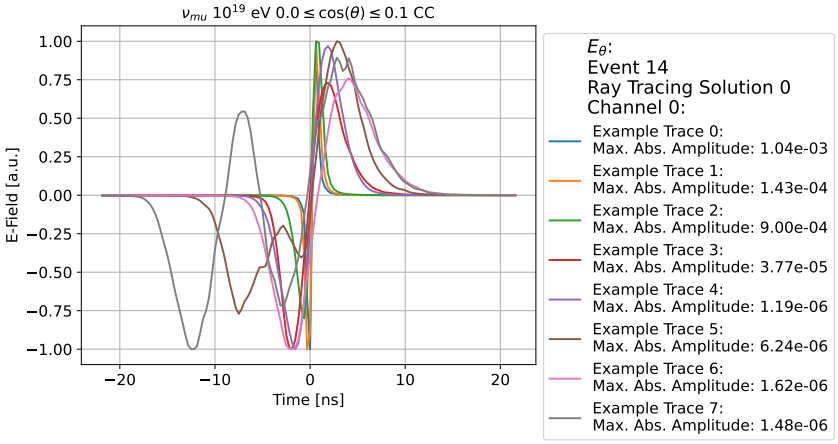

Figure 5.19: Examples of electric field traces in θ-direction in Channel 0. For better visibility the maximum of the trace is normalized to one and they are synchronized in time by plotting the steepest increase at t=0 ns. If the slope was negative, the trace is shown inverted.

particles are produced as explained in section 2.2. This leads to more charges participating in the charge separation of the shower leading to a stronger radio emission. The amplitude of the electric field trace arriving at the antenna is additionally dependent on the distance of the propagated path and the attenuation along it. The energy of a shower and the distance of travel are independent from each other. The maximum electric field amplitude of the NC events is generally larger, since the hadronic shower tends to receive a relatively large amount of the initial neutrino energy. Since in the case of the CC events each event has several showers, the energy of the muon is distributed over several showers, shifting the distribution to lower energies as shown in section 4.1 in Figure 4.1c. Additionally, traces of all showers and channels where the 2σ-trigger of Channel 0 sets off are saved for further processing. A single low-energy shower in an an NC event might not be sufficient to trigger, whereas low-energy showers in CC events, accompanying higher energetic showers that set off the trigger, are saved as well. The amplitude of the electric field in R-direction is several orders of magnitude smaller than in θ- and ϕ- direction. This is reasonable, neglecting the bending of the radio waves, R is the direction of of wave propagation, where the electric field is always zero. Additional ray bending leads to a non-zero R component. Some electric field traces are constant zero due to impreciseness of the calculations. Due to the logarithmic axis they are not considered in the plot. This mostly happens in the case for traces in R-direction, which is why the distribution is lower.

Figure 5.19 shows the electric field traces in θ-direction of several showers in channel 0 from one event. They have been synchronized at $t = 0$ ns by determining the steepest point of the trace by finding the maximum of the absolute difference to the next sampling point. If the gradient at this point is negative, the whole trace is inverted. The plotted electric field traces are additionally normalized to their maximum for better visibility. Their maximum amplitudes are given in the legend. The general shape of the electric field trace can be described by a bipolar pulse: a dip and peak with a similar amplitude. The width of the signal varies. The three traces shown in brown, pink and gray differ slightly from this description, due to the smaller original amplitude. A more extreme example of a low amplitude trace with disturbances is shown in Figure 5.20, where the original trace in black can not be shifted to zero by calculating the absolute difference between

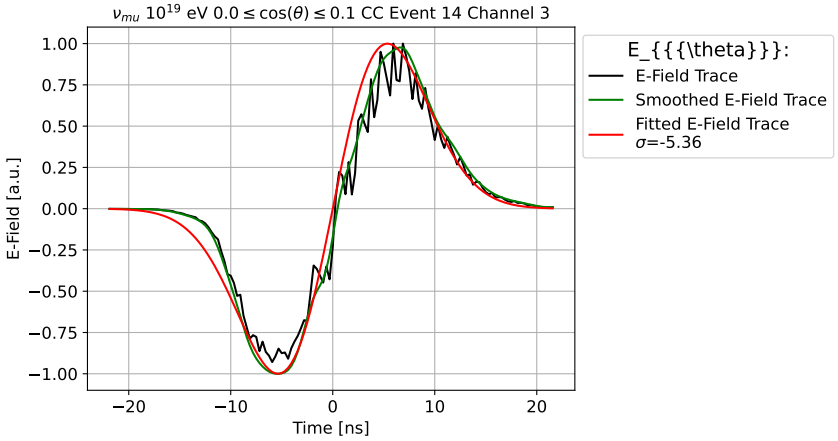

Figure 5.20: Example of a normalized unsteady electric field trace, shown in black, where the steepest gradient can not be directly identified, to center the bipolar pulse at 0 ns. A smoothed version of the electric field trace is shown in green. The red line shows the fit of the smoothed trace.

neighboring sample points. Thus, all traces are smoothed using a Butterworth filter of third order with a critical frequency of 0.2 on a trace with sampling rate of 3.2 GHz. This was implemented using Scipy [52] by defining the Butterworth filter using scipy.signal.butter and filtering the signal using scipy.signal.filtfilt. The smoothed signal is shown in Figure 5.20 in green. The original trace in black was aligned using the determined shift of the smoothed trace.

To approximate the shape of the electric field a function of the form

$$f(t) = -a\sqrt{2\pi}\sigma^2 \exp\left(\frac{1}{2}\right) \frac{\exp\left(\frac{-t^2}{2\sigma^2}\right) \cdot t}{\sqrt{2\pi}\sigma^3} \tag{5.3}$$

was chosen. t is the time. $t = 0$, is the zeros crossing. The width of the signal σ is in the following fitted to the traces. Therefor trace is normalized and the amplitude a is set to 1. This is advantageous, since only one parameter has to be fitted. The maximal amplitudes span over several orders of magnitude as shown in Figure 5.18, which would challenge the fitting algorithm. The fit was performed over 70 sampling points before and after the steepest slope, hence 43.75 ns in total. The fitted function is shown in red in Figure 5.20. This fit was determined for 43 246 electric field traces. The resulting values for σ in R, θ and ϕ direction are shown in Figures 5.21a, 5.21b and 5.21c. σ is in the same order of magnitude for all three directions. It is determined to be zero, when there are no fit solutions found, which is the case when the trace is constant zero. This is the case in about one third of electric field traces in R-direction.

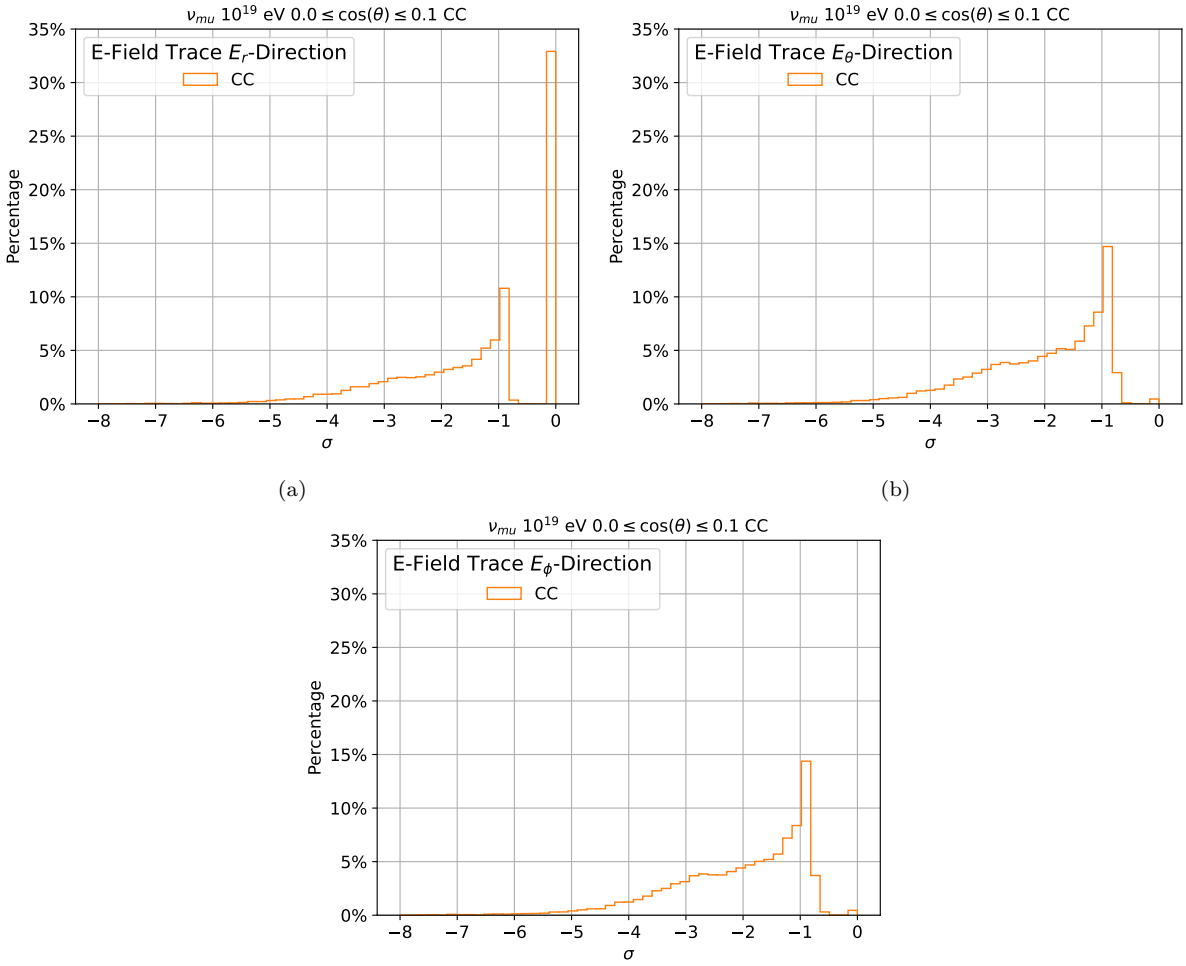

Figure 5.21: Distribution of the determined fit parameter σ to approximate electric field traces in R(5.21a), θ(5.21b), and ϕ(5.21c) directions. On the x-axis σ is shown on a linear scale. On the y-axis the percentage of all investigated traces in each bin is shown.

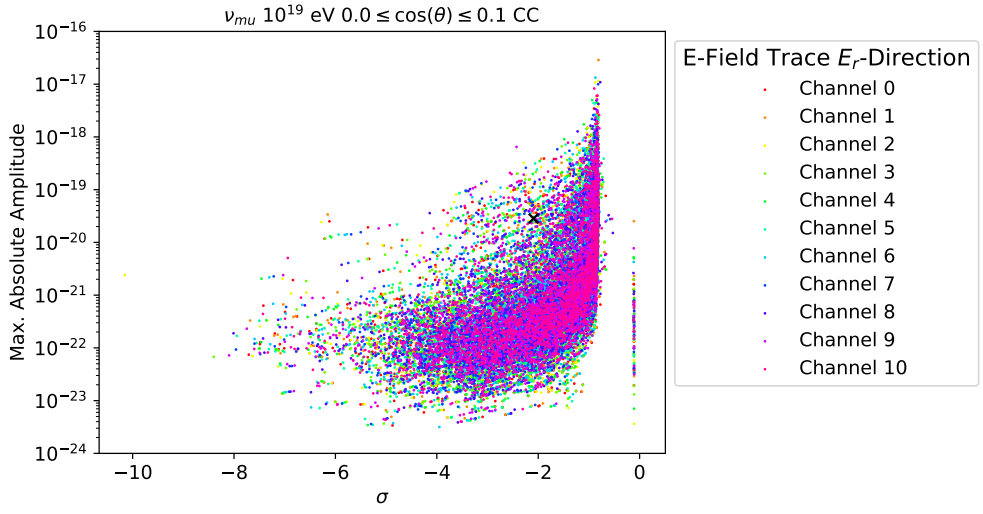

(a)

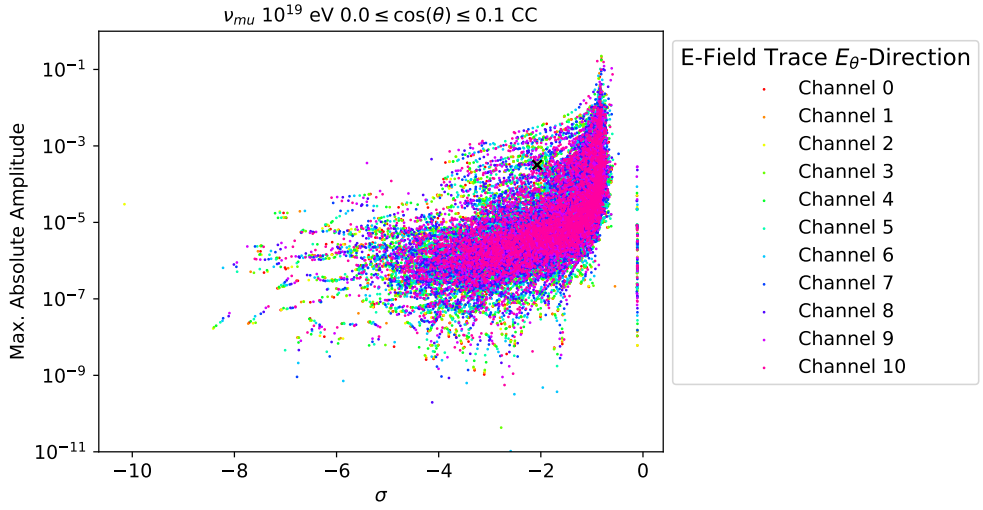

(b)

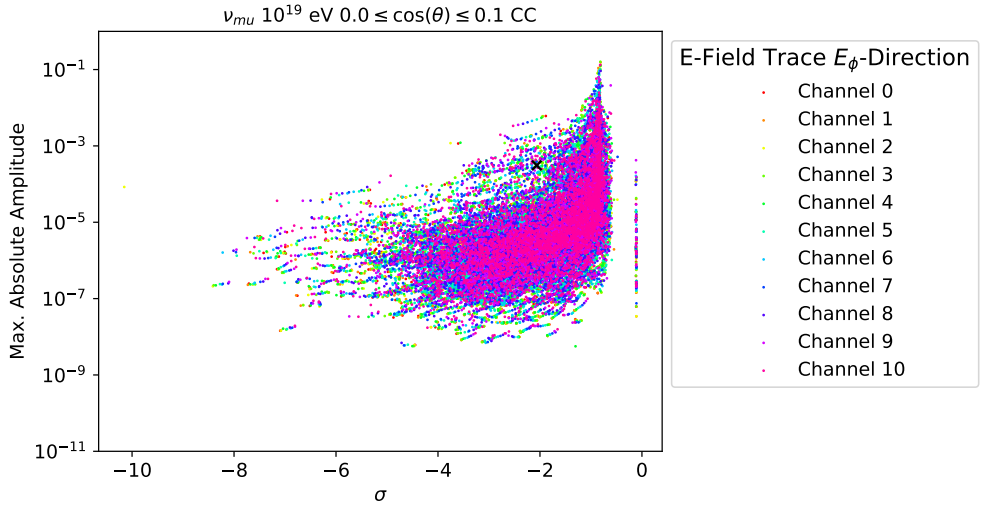

(c)

Figure 5.22: Scatter plots of the determined parameter combination amplitude a and σ in R(5.22a) ,θ(5.22b) and ϕ(5.22c)-direction to approximate the shapes of the electric field trace shapes. a is shown on the y-axis on a logarithmic scale and σ on the x-axis on a linear scale. Each color indicates a different channel number. Each plot also contain a black cross, where the mean of the parameter a and σ are located.

Direction i	Pulse Width $\sigma_{opt,i}$	$s(\sigma_{opt,i})$	Amplitude $a_{opt,i}$	$s(a_{opt,i})$
R	-2.091	1.173	1.913e-20	2.301e-19
θ	-2.071	1.160	3.205e-4	3.196e-3
ϕ	-2.063	1.163	3.090e-4	3.030e-3

Table 5.1: Determined parameters $a_{opt,i}$ and $\sigma_{opt,i}$ for electric field traces in direction i: R, θ and ϕ together with the standard deviation of the values $s(a_{opt,i})$ and $s(\sigma_{opt,i})$.

The determined signal widths σ and maximum amplitudes a are shown in figure Figure 5.22 as a scatter plot. The color of the points indicates the channel. The maximum amplitude is shown on a logarithmic scale and σ on a linear scale. From this plot we can confirm, that there is no noticeable difference between channels, and that they provide an alike distribution. In the fringe regions some clusters of aligned data points are visible. Such a cluster can be seen in Figure 5.22c around $\sigma = -7$ and $a = 1e - 8$. The cluster consists of data points from different channels. These aligned clusters stem from one shower as seen in different channels. These correlations in principle influence the results, but due to the high total number of showers this effect can be ignored. The data points form a large cluster. While events with a smaller determined σ tend to a higher maximum amplitude, there is no evident relation. In all three directions the values form a widespread cluster of similar shape. At $\sigma = 0$ some data points spread over different maximum amplitudes. In these cases σ was set to zero due to the fit not converging and aborting.

To determine the parameters to obtain the detector response trace the mean of the maximum amplitudes was used as the parameter a_{opt} and the mean of the determined fit parameters σ_{opt}. For these calculations traces with a constant value of 0 or where no fitting parameter σ was found were ignored. The determined points are shown in Figure 5.22 as black crosses. Due to the logarithmic y-axis they seem shifted to the data points. The determined values are shown together with the calculated standard deviation $s(\sigma_{opt})$ and $s(a_{opt})$ in Table 5.1. The determined standard deviations are huge. For σ the standard deviation lies in the same order of magnitude than the value itself, while for the amplitude a the standard deviation is one order of magnitude larger due to the logarithmic spread. For this reason uncertainties on σ from fitting were not factored in. In retrospective, overfitting is not a limiting factor, and the same simulated events could have been used for determining the form of the electric field trace than for the final performance testing.

From the determined parameters $\sigma_{opt,i}$ and $a_{opt,i}$ a mean electric field trace $E(t)_i$ in direction i is determined:

$$E(t)_i = -a_{opt,i}\sqrt{2\pi}\sigma^2_{opt,i} \exp\left(\frac{1}{2}\right) \frac{\exp\left(\frac{-t^2}{2\sigma^2_{opt,i}}\right) \cdot t}{\sqrt{2\pi}\sigma^3_{opt,i}}. \tag{5.4}$$

This electric field trace can now be used as an input for the detector. NuRadioReco [37] is then used to determine the resulting trace likewise to how it is done in the simulation of events. The resulting trace is shown in Figure 5.23 where the sample points are shown as crosses. This trace will in the following be used as a template for a convolution with the simulated signal traces.

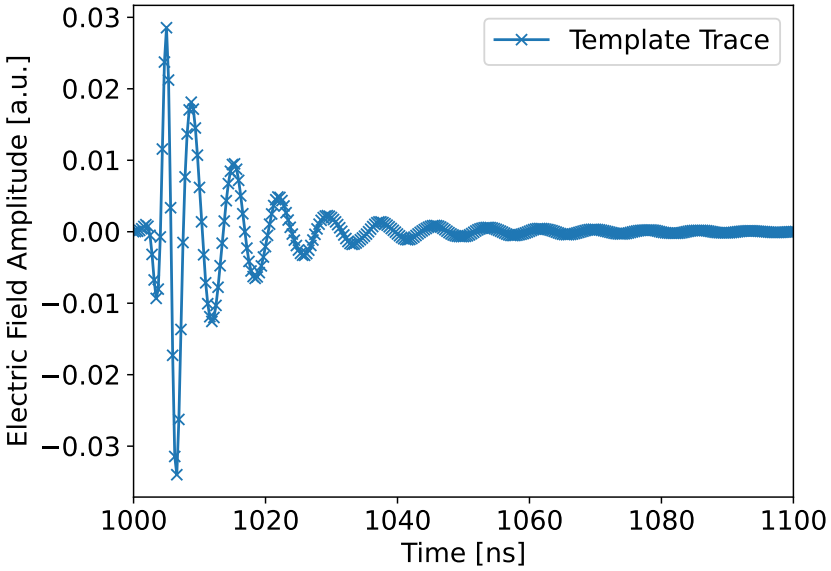

Figure 5.23: Resulting template to approximate the shape of a signal on the trace. It was obtained from the detector response of the used antenna and electronics when inputted the determined parameters to approximate the shape of the electric field traces. The crosses indicate the sampling points.

The convolution of a template $g(t)$ with a trace $f(t)$ of length T is defined as

$$(f * g)(t) = \int_0^T f(\tau)g(t-\tau)d\tau. \tag{5.5}$$

The domain of the template is extended with an amplitude of zero to be defined at a sufficiently large range. The second plot in Figure 5.17 shows the convolution of the trace in the first plot with the determined template as a red dotted line. When the values of $f(\tau)$ and $g(t-\tau)$ match, i.e their forms are the same they multiply constructively. For all values of τ is $f(\tau)g(t-\tau)$positive and the value of the convolution at this point t is high. Since the signal and trace are periodic, a shift of one wavelength additionally leads to a relatively high convolution value. In case of a half wavelength shift f and g have opposite signs leading to a negative extreme of the convolution. If $f(\tau)$ only consists of noise, their random height and value balances out and the absolute convolution value is small.

5.3.1 Strategy 3.1

The amplitude of the convolution of the determined template with the simulated traces can be used to identify and count peaks. Therefor the Hilbert envelope of the absolute convolution is calculated. The most upper plot in Figure 5.17 shows a part of a noiseless simulated trace in red, with three different sized signals. The second plot shows the convolution of the template with the trace and the Hilbert envelope of the absolute convolution. As done in previously introduced Strategies, the maxima on the Hilbert envelope are determined and compared to a threshold. In the following the threshold applied to the convolution is given in arbitrary units. In this example only the highest peak will be counted.

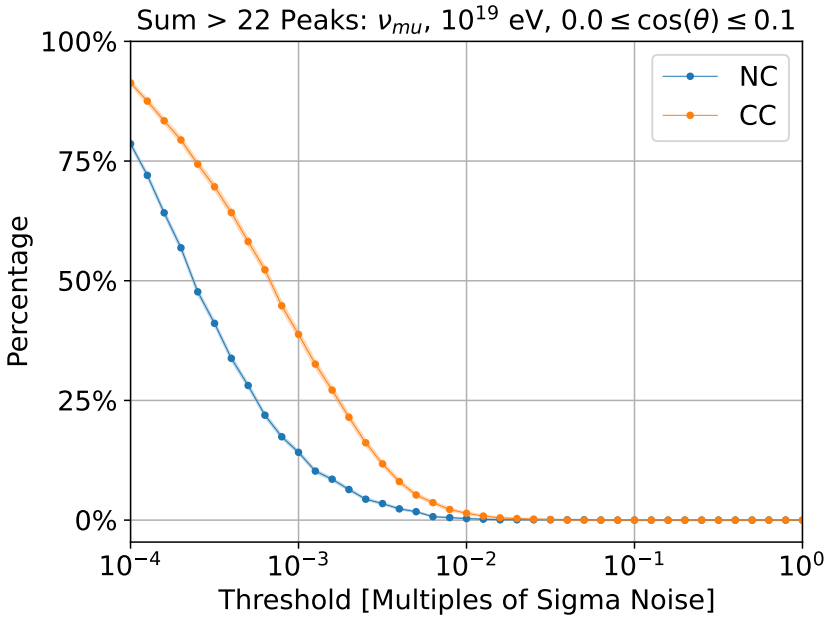

Figure 5.24: Amount of events, where the total number of found events with Strategy 3.1 in all traces is greater than 22. In blue the results of the NC events and in orange the results of the CC events are shown with their 1σ confidence band.

The advantage of Strategy 3.1 is illustrated with the third plot in Figure 5.17. It shows the trace of Channel 0 of the same event than in the most upper plot, but with additional thermal noise. While the highest signal is still apparent, the medium and small sized signals are not visible by bare eye. The lowest plot, shows the convolution of the template with the noisy trace. The threshold is chosen to obtain the highest and medium high peak. Compared to the convolution of the noiseless trace the necessary threshold to select both signals is higher for the noisy trace. Additionally the scale of the convolution depends on the amplitude and form of the template. Therefore caution has to be exercised, when comparing results of convolutions. The smallest peak, will neither be found definite in the noiseless nor in the noisy convolution. In the noiseless convolution, even for a low enough threshold no additional maximum is present between the small and medium signal, counting them as one. In the noisy convolution a threshold low enough to count the maximum at the position of the smallest signal will already count several maxima emerging from the noise. While the noiseless trace only has two found maxima at the first signal in the range of several tenths of ns in the same range at the convolution of the noisy trace several more peaks are present. The performance of distinguishing NC from CC events by selecting on the total number of found peaks in all traces on noiseless traces is shown on Figure 5.24. Compared to Strategy 2.3 shown in Figure 5.24 this is a clear deterioration. The two lines lie closer to each other making the selection less efficient and less pure. An quantitative analysis of the efficiency and purity will follow in section 6.2 as well an investigation of the performance noisy traces in section 6.6.

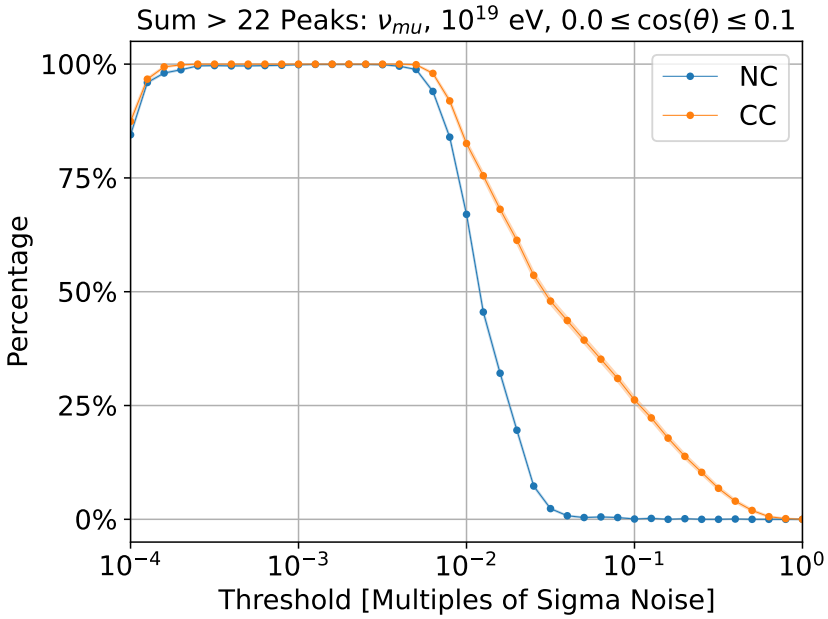

Figure 5.25: Amount of events, where the total number of found events with Strategy 3.2 in all traces is greater than 22. In blue the results of the NC events and in orange the results of the CC events are shown with their 1σ confidence band.

5.3.2 Strategy 3.2

Meanwhile similar approaches as for Strategy 2 can be applied to Strategy 3. Strategy 3.2 normalizes the envelope to its maximum before searching for maxima and applying the threshold. In Figure 5.25 a similar improvement of Strategy 3.2 against Strategy 3.1 can be observed in comparison to Strategy 2.3 against Strategy 2.1: The misclassification of NC events is drastically reduced for high thresholds. At small thresholds all events are classified as CC events.

5.3.3 Strategy 3.3

Strategy 3.3 tackles the issue, discussed in subsection 5.3.1, of an increased number of found maxima on the envelope due to the noise in the range of a signal compared to the noiseless trace. Here, the envelope is not normalized to its maximum for comparison reasons. The demanded number of maxima between two peaks is again two. While this approach was not improving the results on noiseless traces when applied on the envelope of the trace itself, it is worth investigating later for noisy traces. For completeness Figure 5.26 shows the performance of Strategy 3.3 on noiseless traces. Compared to Strategy 3.1 in Figure 5.24 no improvements are apparent.

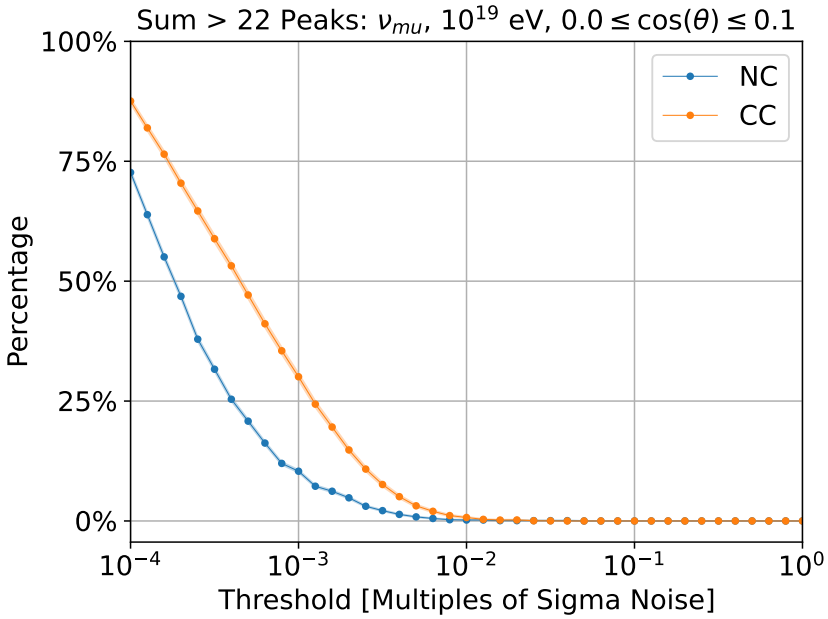

Figure 5.26: Amount of events, where the total number of found events with Strategy 3.3 in all traces is greater than 22. In blue the results of the NC events and in orange the results of the CC events are shown with their 1σ confidence band.

5.3.4 Strategy 3.4

Lastly in Strategy 3.4 the improvements of Strategy 3.2 and 3.3 are combined. The envelope of the convolution is normalized to its maximum. The maxima are obtained and a peak is still counted as one continuous peak even if one single maximum undercuts the threshold. Figure 5.27 shows the amount of events complying the requirement of more than 22 found peaks with Strategy 3.4 in all channels for noiseless traces. At large thresholds almost none of the NC events contain more than 22 peaks. In that range the amount of CC events with more than 22 found peaks rises steadily. The amount of NC events increases sharply for thresholds below 0.025. Here also the amount of CC events increases rapidly. Both data sets reach a maximum of 100% at a threshold of about 0.0025. At the lowest thresholds less and less individual peaks are identified, since most found maxima are above the threshold being interpreted as one wide peak.

In Table 5.2 the eight introduced strategies are summarized. In the next chapter the performance of the strategies will be analyzed and compared. The generalization of the strategies to be used on neutrinos with different parameters and the possibility of differentiation among different CC interacting neutrino flavors is investigated. The performance of the strategies on noisy traces is assessed as well.

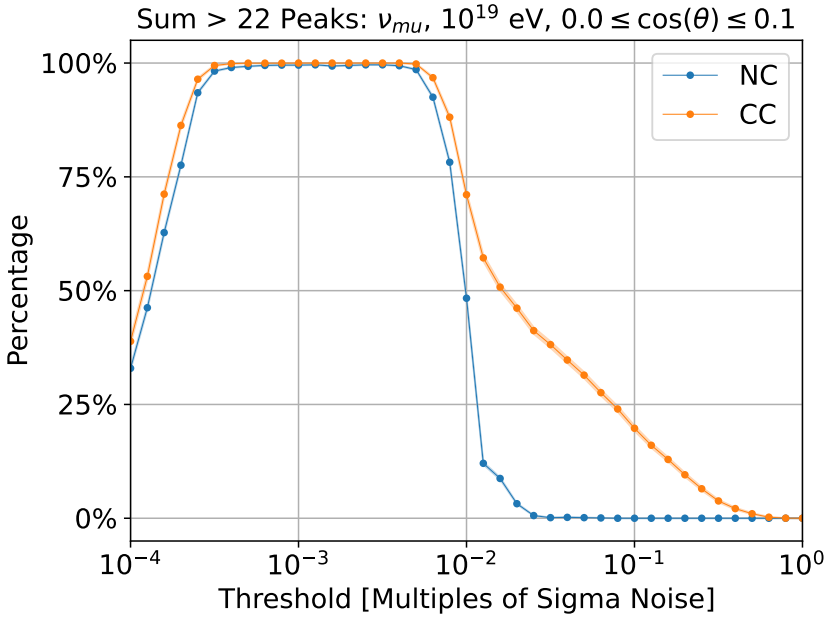

Figure 5.27: Amount of events, where the total number of found events with Strategy 3.4 in all traces is greater than 22. In blue the results of the NC events and in orange the results of the CC events are shown with their 1σ confidence band.

	Convolution	Hilbert Envelope	Normalization	Peak Recess
Strategy 1	✗	✗	✗	1
Strategy 2.1	✗	✓	✗	1
Strategy 2.2	✗	✓	✗	2
Strategy 2.3	✗	✓	✓	1
Strategy 3.1	✓	✓	✗	1
Strategy 3.2	✓	✓	✓	1
Strategy 3.3	✓	✓	✗	2
Strategy 3.4	✓	✓	✓	2

Table 5.2: Overview over the introduced Strategies. The first column indicates whether a convolution with the determined template was used. The second column indicates whether the maxima were searched on the trace directly or if the Hilbert envelope was used. Depending on whether the convolution was calculated or not the Hilbert envelope of the trace or of the convolution was calculated and the normalization was either performed on the trace before applying the Hilbert envelope or after the Convolution and Hilbert envelope were calculated. The peak recess indicates the number of peaks below the threshold are needed to initiate a new peak.

Chapter 6

Performance of Flavor Separation

6.1 Classification Metrics

To quantify the performance of a classifier a confusion matrix as shown in Table 6.1 can be used: The Positive P and Negative N is the amount of data the classifier was tested on. Here, P is the number of CC events and N the number of NC events. These values and the other investigated parameter combinations are listed in Table 3.2. When a certain strategy with a set threshold is applied to the two data sets, a certain amount of CC events will make the cut and have more than 22 found peaks. These are True Positive events TP, which are classified correctly as CC events. Some of the CC events will not make the cut and are misclassified as NC events. They make up the False Negatives FN. The NC events with 22 or less found peaks will be called True Negative events TN. Wrongly identified NC events are called False Positives FP. The Sum of True Positives and False Positives yields the Predicted Positives PP, i.e the total amount of CC classified events. Similarly, the Predicted Negatives PN are all predicted NC events combined [55].

To further analyze the results, it is necessary to take the difference in the number of positive and negative events into account. Thus, the true positive rate TPR is introduced as

$$TPR = \frac{TP}{P} \tag{6.1}$$

and the false positive rate FPR as

$$FPR = \frac{FP}{N}. \tag{6.2}$$

These values are independent of the ratio between positive events and negative events used for classification and can thus be compared without distorting the results. These measures have already been shown, for example in Figure 5.27, where the TPR is shown in orange and the FPR in blue for different thresholds. The TPR and the FPR can also be plotted against each other. For multiple different classifications, i.e due to varying thresholds, the resulting data points lie on a curve called Receiver Operating Characteristics (ROC) curve. ROC curves are also commonly used in Machine Learning to visualize the performance of a classifier. It visualizes the trade offs between the benefits of correctly classified events and costs of falsely classified events and will be used as one basis to judge the performance of a selection [55].

		True Class	
		Positive P	Negative N
Predicted Class	Predicted Positive PP	True Positive TP	False Positive FP
	Predicted Negative PN	False Negative FN	True Negative TN

Table 6.1: General depiction of a Confusion Matrix, which yields an overview of the performance of a classifier. From the entries in the Confusion Matrix further metrics can be deduced to quantify the goodness of a classification. The labeled groups of Positives P and Negatives N are classified and yield the Predicted Positives PP and Predicted Negatives PN. Correctly classified events are named True Positives TP or True Negatives TN depending on their origin class. Not all events are classified correctly and are called False Negatives FN if Positives are classified as Negatives and False Positives if Negatives are misclassified as Positives.

The TPR is a measure of the sensitivity of the classification, and holds information about how efficient the classification is in selecting the positives. It cannot tell how precise the classification is in selecting only the right events. If all events regardless of their initial interaction type are classified as CC events the TPR is one. Even though the combination of TPR and FPR gives and idea of the ideal parameters a more comprehensible depiction of the efficiency of the classification is the measure precision PRE. It can also be deduced from the confusion matrix: It indicates the fraction of the positive predicted events, that are actually positive:

$$PRE = \frac{TP}{TP + FP} = \frac{TP}{PP}. \tag{6.3}$$

It only takes the classification of Positives into account. If the majority of positive events are classified as negatives, the precision value is still high. If additionally the negative events were mainly correctly classified as true negatives, the TPR would be drastically decreased. Thus the classification may still be very inefficient if the precision value is high. Thus, one metric is not sufficient to quantify the performance of a classifier completely.

The goodness and applicability of a strategy with its resulting event selection depends on the necessary efficiency and precision of the subsequent analysis. High energetic neutrinos are very rare, such that a high efficiency is needed to not miss such a rare event. The precision however is equally important, since, due to the low rate, a high impurity would lead to a high total amount of false positives. The strategy and its parameters therefore need to be selected with regard to the subsequent physical analysis.

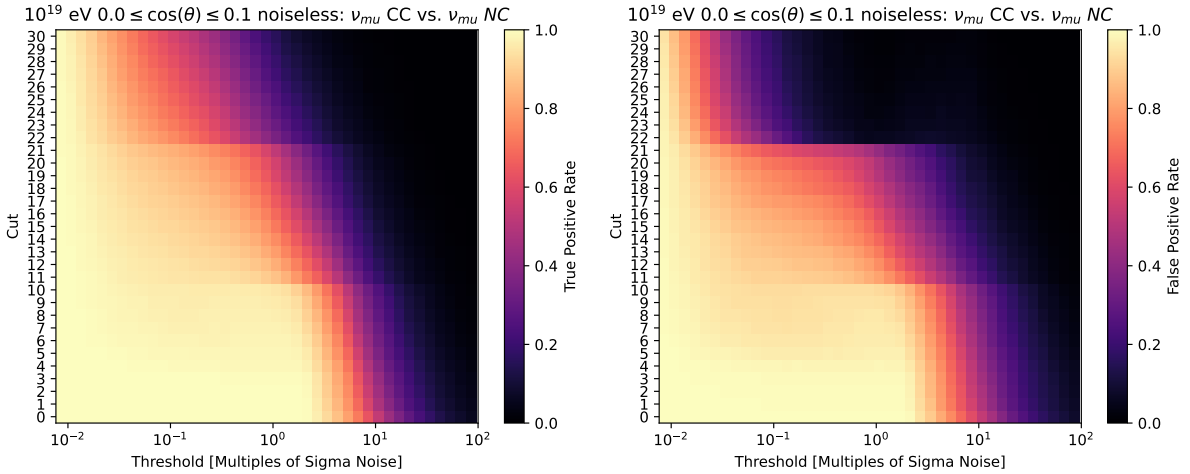

(a) (b)

Figure 6.1: Heat map of the true positive rate (6.1a) and false positive rate (6.1b) for a selection with Strategy 1 to separate muon neutrino CC from NC events at energies of 10^{19} eV and an inclination between 0.0 to 0.1 in dependence of the investigated thresholds on the x-axis on a logarithmic scale and cut value of total number of peaks in all eleven traces, that needs to be surpassed to qualify as a CC event.

6.2 Current Differentiation

In the following the performance of the previously introduces strategies on the task to differentiate between muon neutrino CC events and muon neutrino NC events at energies of 10^{19} eV and inclinations $\cos(\theta)$ between 0.0 and 0.1 will be quantified. To differentiate CC events from NC at a peak sum of 22 has been well justified in chapter 5, nevertheless it has never been proven to be the ideal cut value. Therefore the peak cut value will also be varied and investigated. Figure 6.1a shows a heat map of the true positive rate of Strategy 1. On the x-axis the investigated thresholds are shown on a logarithmic scale. On the y-axis the cut number of total found peaks in all eleven channels which needs to be surpassed to qualify as a CC event is shown. The color indicates the true positive rate value between zero in black and one in light yellow. A change in the TPR is always caused by a change in the amount of True Positive events, i.e the number of correctly selected CC events, as the number of positive events is the same for all investigated cut and threshold values since the number of CC events on which the strategy was tested on always stays the same. At high thresholds the TPR is zero, because the threshold is too high to find any peaks. For smaller thresholds the TPR increases. For small cut values it takes about one order of magnitude to arrive at a TPR of one. At cut values over 22 the transition happens at lower thresholds and spans over two orders of magnitude of thresholds. At the lowest thresholds the TPR is one for all investigated cut values, since the number of found peaks exceeds the plotted maximum of 30. In the transition regions, where the TPR is neither zero nor one, two apparent steps in the TPR values happen at cuts from ten to eleven and 21 to 22. The increase of the cut yields an immediate reduction in the TPR. This can be explained by the main share of CC events having the same amount of signals in all eleven traces. When only one signal is present in all of the channels, this event get excluded as soon as a total amount of more than eleven peaks is demanded. The equivalent explanation holds true for the step between more than 21 and 22 found peaks, where suddenly all events with exactly two signals in each channel

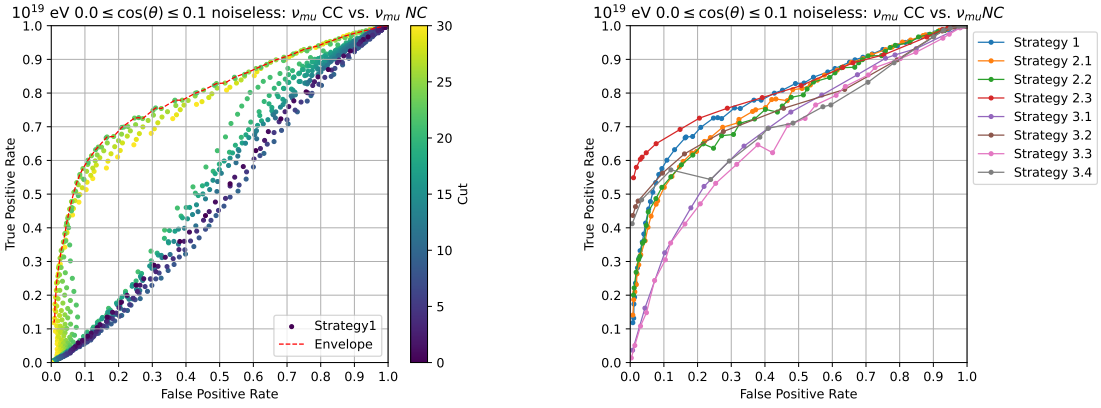

(a) (b)

Figure 6.2: Visualization of the performance of separating muon neutrino CC events from NC events at an energy of 10^{19} eV and inclinations between 0.0 to 0.1. Figure 6.2a shows the obtainable TPR and FPR values for the investigated parameters using Strategy 1. The color of the data points indicate the cut value. The maximum achievable TPRs are indicated by a red guidance line. Figure 6.2b shows the guidance lines indicating the maximum achievable performance for all eight investigated strategies for comparison.

get excluded. Due to the cumulative nature of the cut condition, the TPR will never increase with a higher cut value. Also in between the steps the TPR slightly decreases with a higher cut. While most of the time all channels have the same number of signals in their trace, sometimes the signals in the upper channels fuse together and are seen as one as shown in Figure 5.1 or the signal does not arrive at certain channels due to their relative positioning. Additionally not all signals might be found on the trace since the attenuation reduces the amplitude of single peaks in different channels, such that not all peaks from all channels are reliably counted at one threshold. This would not be the case for strategies where the traces are normalized.

Figure 6.1b shows the false positive rate in the same manner as Figure 6.1a the TPR. The overall shape looks similar: the FPR decreases with increasing cut values and thresholds as well. The apparent difference between the TPR and FPR lie at cut values above 22 at medium thresholds, where the FPR is zero for a wider range of thresholds. This area of strategy parameters is especially interesting, since the FPR should be minimized and the TPR maximized for an ideal event selection.

In Figure 6.2a the ROC-curve of Strategy 1 is shown. The color of the data points indicate the cut value. On the x-axis the FPR values, shown in Figure 6.1b, are shown and the TPR, shown in Figure 6.1a, on the y-axis. This representation is favored, since the trivial points where the TPR and FPR are both one or zero are condensed in two points and the values of interest can be compared easily visually. Unfortunately the information of the cut value and threshold can not simultaneously be encoded in this representation. An ideal classifier would have a TPR of one and a FPR of zero. The more to the upper left of the plot, the better the classifier. A random classifier would provide results with the same TPR and FPR, leading to points on the diagonal.

The data points are spread in a hollow wing shape. At the upper and lower tip where the TPR and FPR are zero and one respectively, they are densely scattered. In between the data points split in an upper and a lower band. The lower band consists of dark green, teal and blue points, indicating low cut values. They approximately lie on the diagonal of the plot. These parameter combinations are of no use, since a random classifier would yield similar results. The light green and yellow data points with high cut values forming the upper band stem from the area in Figure 6.1a and Figure 6.1b, where their values differ at medium thresholds and high cut values. The points most closely to (0,1) stem from a parameter combination with a cut value of 22. Only at lowest FPR values below 0.05 higher cut values outdo the achieved TPR.

Additionally a dashed red line is shown as a guidance line for the maximum achievable performance of Strategy 1. The algorithm used to obtain this line is explained in Appendix A. It is to note that not necessarily all values on this line can be achieved since the cut values are discrete values. In section 5.1 the determination of the statistical uncertainties on the FPR and TPR have been explained. In this chapter, the uncertainties are not further worked out due to limitations in their depiction in the heat map and scatter plots. The consideration of the uncertainties in the determination of the guidance line would have been excessive, with little to no gain. These guidance lines can be established for all eight investigated strategies as shown in Figure 6.2b.

The different colored lines show the maximum achievable relations between TPR and FPR. Additionally to the guidance lines the data points which were used to construct the lines are plotted as well. The normalization of the trace improves the performance drastically at low FPRs: at the lowest FPRs Strategy 2.3 (red), 3.2 (brown) and 3.4 (gray) all lie above a TPR of 0.4 while the TPRs of the other non-normalized strategies lie below 0.2. Increasing the distance between peaks to two maxima has a tendency to poorer results: For the convoluted Strategies the performance of Strategy 3.3 (pink) is same or worse than Strategy 3.1 (violet) at all FPRs. The same is the case when comparing Strategy 3.4 to 3.2, where Strategy 3.4 deviates from Strategy 3.2 above FPRs of 0.1. Strategy 2.2 yields a higher TPR to FPR relation at low FPRs than Strategy 2.1. Overall, for FPRs below 0.4 Strategy 2.3 yields the highest TPRs of values between 0.55 and 0.8. Above, Strategy 1 is a slight improvement. Figure 6.3a shows a heat map of the precision for Strategy 1. At the lowest threshold and below a cut of 22, the precision converges against 0.76 which is the ratio between CC and NC events. If all events are classified as CC or if the classification is as good as a random classifier a precision of this value is achieved. Since the amount of NC and CC events are unequal, the expected precision of a random classifier is $\frac{P}{P+N} = 0.76$. Above cut values of 22 a sudden increase of the precision happens due to a decrease of falsely identified NC events. At high thresholds and high cuts the precision can not be calculated, since the threshold is not low enough to find any peaks. The transition from undefined values to medium precision is unsteady, due to a low amount of classified events. If only one event satisfies the conditions, the precision is either one or zero.

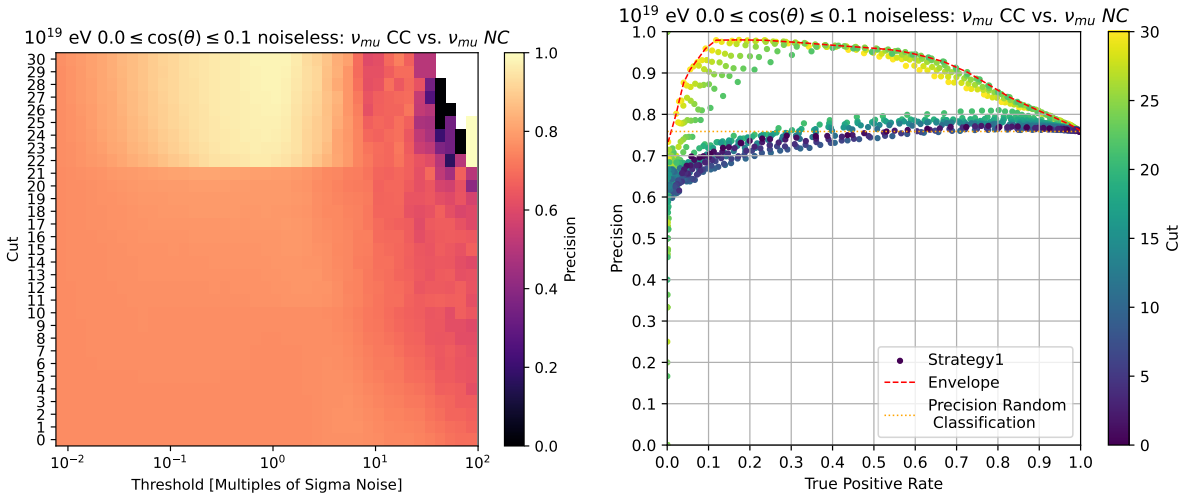

(a) (b)

Figure 6.3: Representation of the achievable precision for separating muon neutrino CC events from NC events at energies of 10^{19} eV and inclinations between 0.0 to 0.1. Figure 6.3a shows a heat map of the precision for Strategy 1 in dependence of the threshold and cut value. Figure 6.3b shows the precision in dependence of the TPR for Strategy 1, where the color of the data points indicate the used cut value. The maximum achievable precision is indicated by a red guidance line. The orange line indicates the precision of a random classifier.

Figure 6.3b shows the precision on the y-axis against the TPR on the x-Axis. The color of the data points again indicates the cut value. Just like the ROC-curve the TPR-precision plot is composed of two distinct bands of data points. The upper band resulting from classifiers with a cut value of 22 or more and a lower band originating from cut values below 22. The dotted orange line indicates the expected precision of a random classifier. At the highest TPR the both bands converges against this value. The highest precision is achieved at a TPR of 0.12 and the maximum investigated cut value. At this point only CC events with several signals in multiple channels are selected. Such a strict selection results in high precision at the cost of a low TPR since a lot of CC events are also ruled out. For a TPR between 0.4 and 1 the maximum precision is achieved by a cut value of 22. For some parameter combinations the precision lies below 0.76. This can happen if a higher fraction of NC events is classified as CC events than CC events themselves. This is the case for low cut values and high thresholds. As shown in Figure 5.13, NC events have a higher mean maximum amplitude. Thus, for high thresholds more peaks might be found in NC events. In the case of strategies where the trace was normalized, data points do not undercut the orange line.

The red line indicates the best achievable ratio between the TPR and precision. It will now be used to judge the performance of the introduces strategies on the task of differentiating NC from CC events. These results are depicted in Figure 6.4. The y-axis was chosen to only show the relevant precision range above 0.76. At the smallest TPRs the precision of Strategy 1 (blue) is small, but increases rapidly with the TPR. This coincides with the initial observations made in section 5.1, where the percentage share of NC events even surpasses the percentage of selected CC events and has a local maximum shown in Figure 5.6. This feature disappears for all following strategies, starting off with a pure CC event selection at lowest TPRs. The effect of normalization and increasing the minimum number of found maxima in between two peaks yield similar results as from the

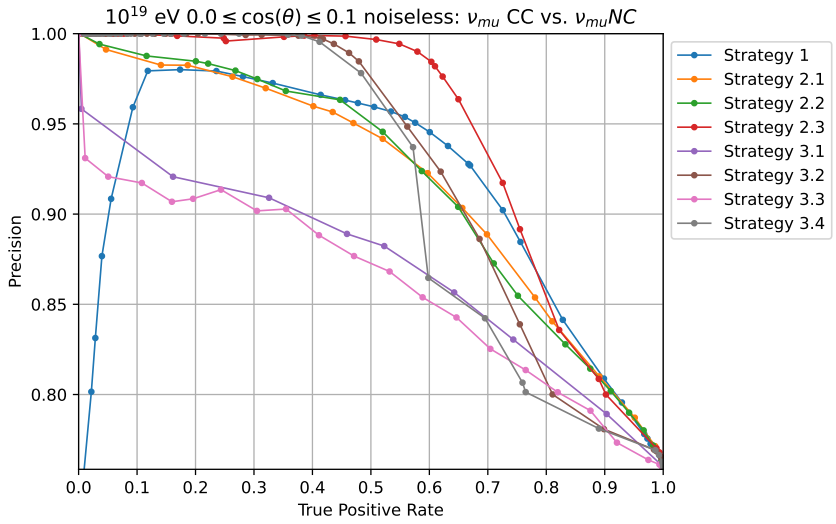

Figure 6.4: Comparison of the achievable precision for the investigated strategies in dependence of the true positive rate.

investigtion of the ROC-curve: Comparing Strategy 3.1 (violet) with 3.3 (pink) and 3.2 (brown) with 3.4 (gray), the strategies demanding at least two maxima in between peaks reduce the precision. Strategy 2.2 (green) demanding two maxima between two peaks exceeds Strategy 2.1 (orange) for low TPR values. The normalization of the trace improves the precision drastically for low and medium TPR. Only at a TPR of 0.74 Strategy 3.4 worsens compared to Strategy 3.2. Strategy 3.3 gets surpassed by Strategy 3.1 at a TPR of 0.78. At the highest TPR this changes again. In contrast, Strategy 2.3 is surpassed by the non-normalizes Strategy 2.1 at 0.82 and never surpasses it again. Strategy 3.2 and 3.4 have a precision of 1 at small TPRs and are therefore a good choice if a low sensitivity is sufficient. Strategy 2.3 also provides a very high precision staying above 0.99 until a TPR of 0.5. Even for higher TPRs Strategy 2.3 performs best up until 0.78 where the precision of Strategy 1 exceeds Strategy 2.3. Thus, depending on the required efficiency and precision Strategy 3.2, 2.3 or 1 should be chosen.

6.3 Energy Dependence

While the strategies introduced in chapter 5 have been developed on the ability to differentiate between CC and NC interacting muon neutrinos at energies of 10^{19} eV, they can also be used to separate neutrinos with other properties. It is worth investigating the performance on other energies and inclinations as well, to determine the generality of these classifications. Due to the variety in strategies and possible values for the cut and threshold, there is still a reasonable amount of free parameters to optimize for certain energies and inclinations, which can be determined independently from the flavor [56] [57]. Figure 6.5a shows the ROC-curve for the selection of CC events from NC events of muon neutrinos with an inclination between 0.0 to 0.1 at a reduced energy of 10^{18} eV. The colored lines show again the maximum achievable TPR in dependence of the FPR for the different introduced strategies. The difference in the strategies with a peak distance of one against two maxima does neither show an improvement nor a deterioration. The normalization is an improvement at small FPRs, where the strategies 2.3 (red), 3.2 (brown) and 3.4 (gray), using normalization, exceeded their non-normalized counterpart, namely strat-

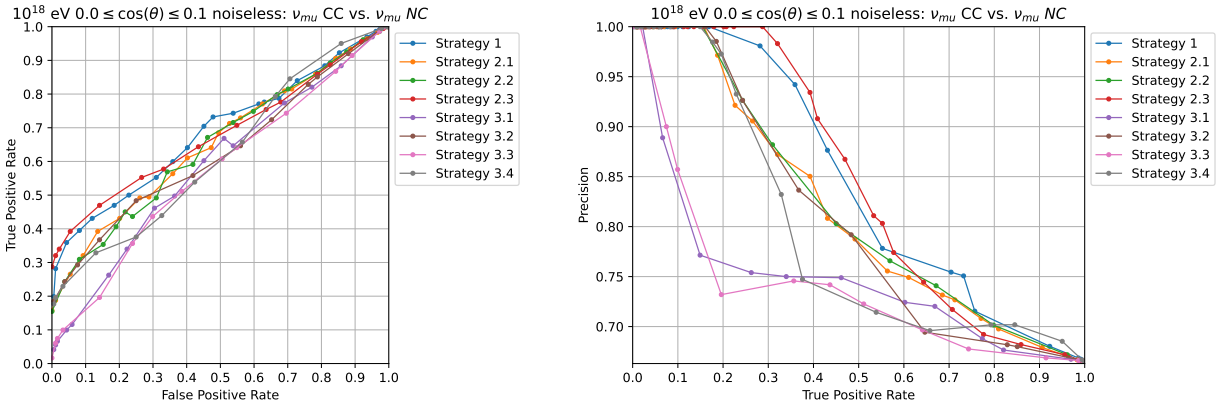

(a) (b)

Figure 6.5: ROC-Curve and performance plot of differentiating CC muon neutrinos from NC muon neutrinos at an energy of 10^{18} eV and an inclination between 0.0 to 0.1. Figure 6.5a shows the ROC-curve of the different classification strategies. Figure 6.5b shows the achievable precision at lower energies

egy 2.1 (orange), 3.1 (violet) and 3.3 (pink). For FPRs below 0.35 Strategy 2.3 performs best. From there, Strategy 1 performs best up to a FPR of 0.6, where it gets surpassed by Strategy 3.4. The guidance lines lie closer to the diagonal than for events with a higher energy, meaning that the separation of CC and NC events is more difficult for lower energies.

In Figure 6.5b the precision in dependence of the TPR is shown for an energy of 10^{18} eV. With Strategy 2.3 a perfectly pure selection can be achieved with a TPR of up to 0.29 which is a reduction compared to the value of about 0.4 at an energy of 10^{19} eV. For higher TPRs the precision drops more steeply. It is to note, that the absolute values of the precision can not be compared due to different baselines depending on the ratio between investigated CC and NC events. Other measures, similar to the precision could have been used, e.g an adjustment of the precision to a range of $[0, 1]$ where 0 corresponds to a precision of the fraction of investigated events $\frac{P}{N}$. However, the value of the precision was decided to be more vivid and the trend of the precision can be visually compared between investigated neutrino parameters due to the adjusted y-axis range.

Compared to an energy of 10^{19} eV the relative performance of the strategies is similar at small FPRs and dominated by Strategy 2.3 and 1. With reduced energy of the incoming neutrino, the individual showers also obtain less energy, as shown in section 4.1. Thus, each shower contains less particles and the charge excess is reduced. This leads to a reduction of the amplitude of the emitted radio signal and finally to less measured events. Thus, the difference in the number of signals between NC and CC events is reduced and the selection becomes more difficult.

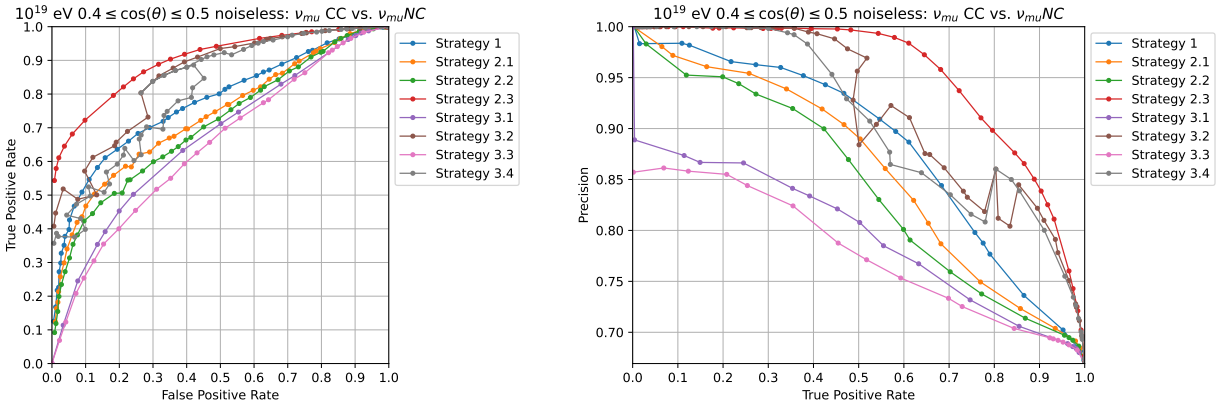

(a) (b)

Figure 6.6: ROC-curve and TPR-precision plot for the separation of CC muon neutrinos from NC muon neutrinos at an energy of 10^{19} eV and an inclination range from 0.1 to 0.5. Figure 6.6a shows the ROC-curve, with the guidance lines of the highest achievable performance for all eight strategies. Figure 6.6b shows the achievable precision in dependence of the True positive rate for the different investigated strategies.

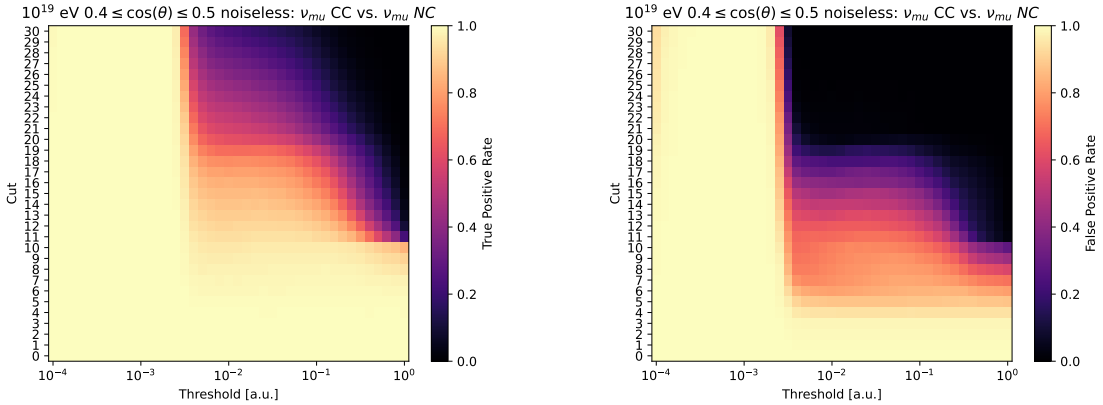

(a) (b)

Figure 6.7: Heat map of the true positive rate (6.7a) and false positive rate (6.7a) for Strategy 2.3 in dependence of the threshold on the x-axis and the cut value on the y-axis determining the number of found peaks that needs to be surpassed to qualify as a CC event.

6.4 Inclination Dependence

As a second parameter the inclination was varied and an inclination range between 0.4 to 0.5 was simulated. Figure 6.6a shows the maximum TPR in dependence on the FPR of differentiating CC muon neutrinos from NC muon neutrinos at an energy of 10^{19} eV for this inclination range. Strategy 2.3 leads the highest TPR at all FPRs. Except for Strategy 3.2 (brown) and 3.4 (gray) the shape of the maximum TPR is quite smooth. Due to the steeper inclination angle, the higher channels do not necessarily also measure signals from the same shower which triggered the deepest channel. The assumption, that in each channel the same amount of signals are found is not longer true for steeper inclinations. However, the event separation is quite successful.

Figure 6.7a shows the TPR in dependence of the threshold and cut value for Strategy 2.3. Figure 6.7b shows the FPR. Strategy 2.3 normalizes the traces to their maximum value before applying the Hilbert envelope. Thus, one would expect at least one found peak in each channel for thresholds smaller than one. Apparently, this is not the case, since at a cut value of ten, the false positive rate is quite reduced. Due to the higher incoming inclination, and following tilted Cerenkov cone a ray tracing solution to higher channels can not be guaranteed, if Channel 0 has been triggered. In the highest Channel this happens for about three quarters of NC events at this inclination, but only in about 15 % of CC events, since in that case the upper channel sees signals from other showers. This opens the possibility to use cut values lower than 22 for classifications. At high thresholds, the range of possible thresholds and cut values above four, lead to potentially different TPRs and FPRs. At the smallest thresholds, the number of detected peaks exceeds the maximum investigated cut value. Thresholds of these small values are of no use to differentiate the interaction current of neutrinos.

The plotted guidance lines in Figure 6.6a of Strategy 3.2 (brown) and 3.4 (gray) are not as smooth as the other guidance lines and contain sharp angles. In the case of Strategy 3.2, at a FPR of 0.26, a steep increase in the TPR is present. For Strategy 3.4, in the FPR range from 0.25 and 0.45 the guidance line first follows some lower TPR data points, instead of jumping to higher date points as in the case of Strategy 3.2 the line turns and follows some upper TPR values. The data points with a high TPR stem from cut values smaller than eleven, where the TPR is high since in most of the traces in each channel a signal is present. The FPR is smaller, since there are less events where at least one signal is present in every channel as explained above. While Strategy 2.3 also uses normalized traces, these sharp edges are not present. The reason for this is that due to the steeper inclination of the incoming neutrino, the path length of the direct and indirect path of the radio signal is shorter and the signals tend to lie closer together on the measured trace. The convolution template has a certain length and if the signals are closer together the convolution blurs the two signals into one peak.

Figure 6.6b shows the achievable precision for the steeper inclination. The maximum TPR for a perfectly pure selection with Strategy 2.3 is similar to the one of a more horizontal inclination, but falls less steeply at higher TPRs.

In conclusion, a selection of muon neutrino CC events from NC events is possible, however, this might not be the case for all other inclinations and while the findings might be interpolated between the investigated inclination ranges, a straightforward extrapolation to higher or smaller inclinations is not possible due to the complex relation between inclination, radio wave propagation in an inhomogeneous medium and detectability of the signals. A cut value of 22 is not always the optimal parameter and needs to be adjusted in dependence of the inclination.

6.5 Charged Current Flavor Differentiation

In section 4.2 it was shown, that a muon neutrino creates more showers in the simulated volume as electron neutrinos and also tau neutrinos. While the difference in number of events is smaller, the approach of counting signals on the trace to conclude back to the number of showers and primary neutrino flavor are now investigated.

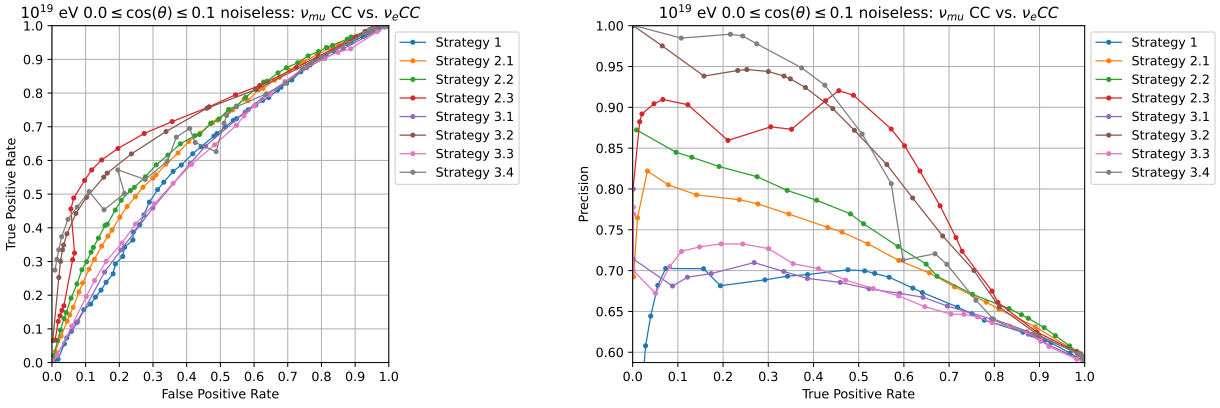

(a) (b)

Figure 6.8: ROC-curve (6.8a) and TPR-precision plot (6.8b) for the investigated strategies on the task to separate CC muon neutrino events from CC electron neutrino events at energies of 10^{19} eV and inclinations between 0.0 and 0.1

6.5.1 ν_e

Figure 6.8a shows the performance comparison for the different strategies on the task of separating CC interacting muon neutrinos from CC interacting electron neutrinos at an inclination range of 0.0 to 0.1 and energies of 10^{19} eV. While in the previous cases, the TPR usually has positive values for a FPR of zero, in the case of electron neutrino muon neutrino separation the TPR starts at zero. Over its course the curve shape bends towards (0,1) for all investigated strategies. At FPRs < 0.05, Strategy 3.4 yields the best TPR, before it gets outperformed by Strategy 2.3. At highest FPRs Strategy 2.2 performs best. In all three cases a high cut value larger than 22 is needed to achieve these highest TPRs. Figure 6.8b shows the precision, where clear differences in the Strategies are visible, but except for minimal TPRs the precision is never 1. This means a perfectly pure selection of muon neutrinos from electron neutrinos is not possible with these techniques.

6.5.2 ν_{tau}

The TPR and FPR for a selection of CC interacting muon neutrinos from Cc interacting tau neutrinos can be determined as shown in Figure 6.8b. Strategy 1 yields the highest TPR at FPRs larger than 0.05. Below a FPR of 0.05 Strategy 2.1 seems to be the best choice, but at such low FPRs reliable conclusion can not be made due to limited amount of invesitgated strategy parameters. Figure 6.9b shows the precision of this classification. Already at small TPRs the precision drops and approaches the precision base line about linearly. While all investigated strategies yield a better classification than a random classifier, these methods are not sophisticated enough to perform sensible analyses on the resulting selection. While this conclusion is quite disenchanting it is to note, that for this analysis only one station was used. Combining the measurements of several stations might improve the selection in the future.

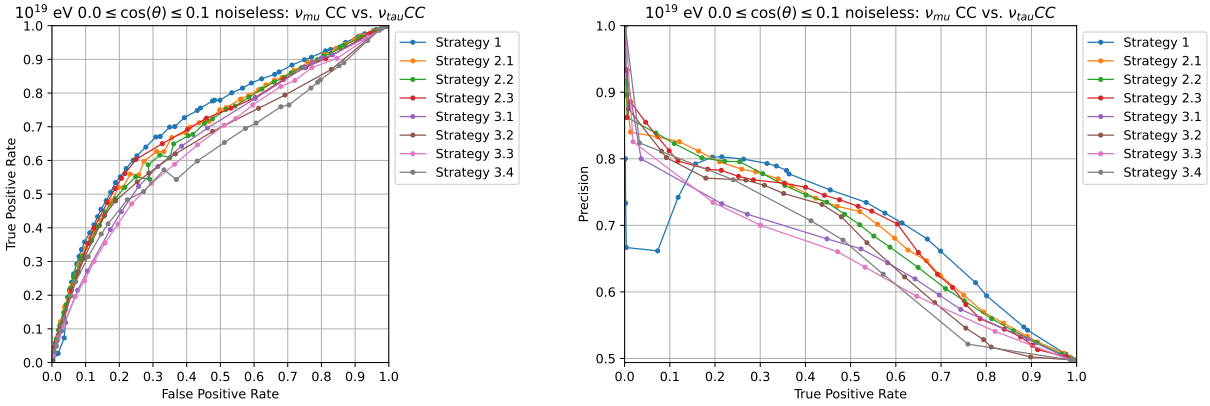

(a) (b)

Figure 6.9: ROC-curve (6.9a) and TPR-precision plot (6.9b) for the investigated strategies on the task to separate CC muon neutrino events from CC tau neutrino events at energies of 10^{19} eV and inclinations between 0.0 and 0.1

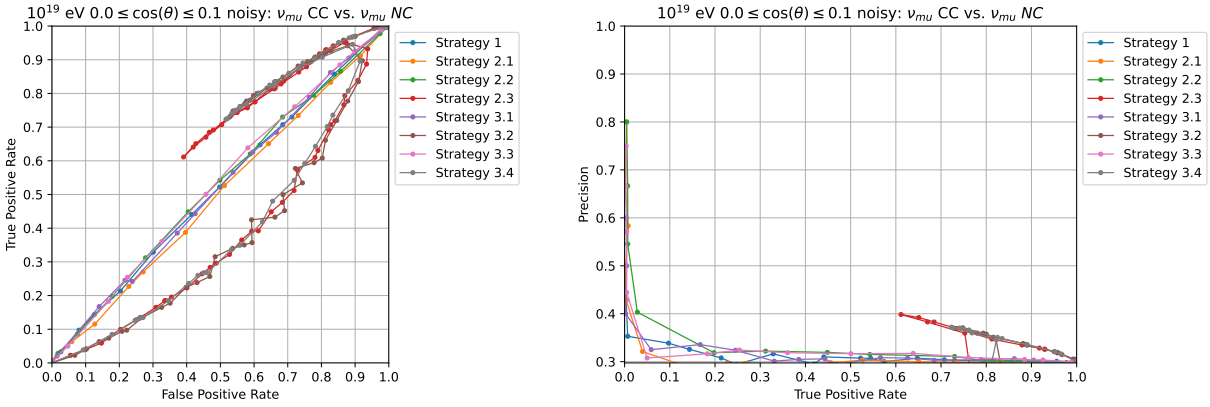

(a) (b)

Figure 6.10: ROC-curve (6.10a) and TPR-precision plot (6.10b) for the investigated strategies for separating CC muon neutrino events with added noise on the trace from noisy NC muon neutrino events. A separation of the performance of normalized strategies (red, brown, gray) and non-normalized strategies, which lie on the diagonal and do not lead to a useful separation is apparent. The separation of noise CC and NC muon neutrino events does not lead to useful results due to the method of event production.

6.6 Influence of Noise

The third type of strategies were developed with the ulterior motive of improving the performance on traces with thermal noise by using the convolution of a template in a trace as explained in section 5.3. This claim was attempted to confirm by applying the developed strategies on traces with noise. However, the comparison of noisy NC and CC events is not as trivial as it is for noiseless traces. While the investigation of noisy trace did not lead to quantitative result, they shall be briefly discussed for further studies.

6.6.1 NC vs. CC

The performance of the strategies on the task to separate noisy traces of muon neutrino CC interaction events from muon neutrino NC interaction is shown in Figure 6.10a. A clear distinction of strategies in normalized strategies non-normalized strategies is visible.

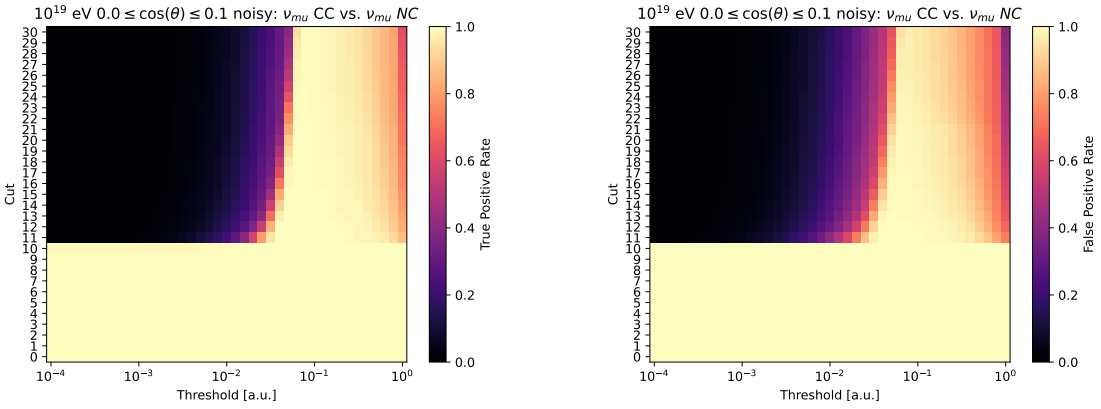

(a) (b)

Figure 6.11: Heat map of the true positive rate (6.11a) and false positive rate (6.11b) for Strategy 2.3 in dependence of the threshold on the x-axis and the cut value on the y-axis on the task of differentiating NC muon neutrinos from CC muon neutrinos with noise on the measured traces.

In the case of normalized strategies the guidance line consists of a part above the diagonal, where the TPR is larger than the FPR and a lower part, where the FPR is smaller than the TPR. The scatter plot of all investigated threshold and cut parameters for Strategy 3.2 is shown as an example in Figure A.1. To understand the two parts of the guidance line, a closer investigation of the TPR and FPR in dependence of the used parameters is useful as shown in Figure 6.11. Due to the normalization at least one peak is detected in each of the eleven traces for all investigated thresholds. In both heat maps two regions, where the rates are unequal one or zero are present: for the highest investigated thresholds, in some of the events more than eleven peaks are found. This is the case for a larger fraction of CC events than NC events. Thus, cut values above eleven and a high threshold lead to the upper part of the guidance line in Figure 6.10a. Decreasing the threshold leads to a multiple of found peaks from the noise. In all events more than the plotted thirty peaks are found and the TPR and FPR are one in this region. By decreasing the threshold further only single maxima still undercut the threshold an the whole trace is counted as one peak at the lowest thresholds. During this transition rates between one and zero are obtained as well. This unification of peaks happens at slightly higher thresholds for CC events, resulting in high FPR values and small TPR values leading to the lower part of the guidance line. This second region does not lead to a proper selection of CC events and the difference in number of peaks in NC and CC events can not be motivated physically. In contrast to the noiseless events the range of useful thresholds is rather slim. To obtain comparable results a finer sampling of thresholds between 0.3 and 1 is needed.

The guidance lines of the non-normalized strategies all lie on the diagonal in Figure 6.10a. This is conspicuous, since the strategies lead to a selection as good as a random classification. This can not be explained with a too noisy data set, since the classification of the samples was possible by using normalized traces to some degree. Also, the guidance line is only made up of a few data points, which would not be the case if all data points would lie on the diagonal as in the case of a random classifier. To trace the origin of this suspicious behaviour, the distribution of the maximum amplitudes of the simulated traces with noise applied to it are shown in Figure 6.12. In blue the amplitudes of the NC events and in orange the amplitudes of the CC events are shown. The vertical lines indicate the mean maximum amplitude. In all eleven channels the mean maximum amplitude of the

CC events is smaller than for NC events. By comparing the maximum amplitudes of noisy traces in Figure 6.12 with the maximum amplitudes of noiseless traces in Figure 5.13 the difference of the mean maximum amplitudes for NC and CC events increases for noisy events. While the distribution of the noisy traces have a hard cut of the maximum amplitude at low values due to the noise exceeding the amplitude of previous maxima, this does not explain the increased difference in maximum amplitudes. The addition of noise should not affect NC and CC events differently.

The origin of this change lies in the simulation of the events. A simulated shower might not be recorded in the detector, if the signal amplitude is to low to surpass the trigger. When noise is added to the trace the trigger might be surpassed by the noise, resulting in a counted event. This happens more often for CC events, since the mean shower energy and thus the radio signal is smaller as shown in section 4.1. This explanations is further supported by investigating the increase of number of events for NC and CC events from noiseless to noisy events. While the number of NC events increased by a factor of 1.3 the number of CC events increased by a factor of 2.4. Consequently, the simulation set is not only contaminated with noisy traces where not a single signal can be identified by the trigger, they are also contaminated by a different extent, making further comparisons of non normalized events invalid. Additionally more events have been simulated due to the expansion of the simulated detector volume for CC events enhancing this effect.

To obtain a more reliable investigation only events that also triggered the detector in the noiseless case could be chosen. This is possible to an extent by comparing the event numbers. Also an increase of the trigger value would avoid events triggered by noise, but also rejects more actual events. For completeness, the precision for separation of noisy traces is shown in Figure 6.10b.

6.6.2 Pure Noise

Nevertheless, a lower limit of the separation capabilities between muon neutrino CC events and pure noise traces without simulated particles showers can be obtained while using an impure muon neutrino CC event set. Figure 6.13a shows the TPR and the FPR for the ability to differentiate noisy CC interaction muon neutrino events with an energy of 10^{19} eV and an inclination between 0.0 to 0.1 from purely noisy traces. On the noiseless traces, the results of the strategies normalizing the trace, namely Strategy 2.3, 3.2 and 3.4 are not reasonable. If there is no signal present, the trace is still normalized to its maximum, which is just the maximum peak of the noise. Indeed, while Strategy 2.3 always performed quite good on noiseless traces, it leads to the lowest TPRs on the noisy traces. Strategy 3.3 and 3.1 perform best, since they use the convolution of the template with the trace, without normalizing it.

The data points yielding the guidance line shown in Figure 6.13a are relatively far apart from each other. Figure 6.14a shows the TPR and Figure 6.14b the FPR in dependence of the parameters for Strategy 3.1. For a wide range of high thresholds both, TPR and FPR, are zero. Below a threshold of 1, the number of counted events drastically increases due to random noise being counted as events. At lower thresholds the number of events increases, since most of the found maxima lie above the threshold and at the smallest investigated thresholds all found maxima lie above the threshold and each channel contains exactly one

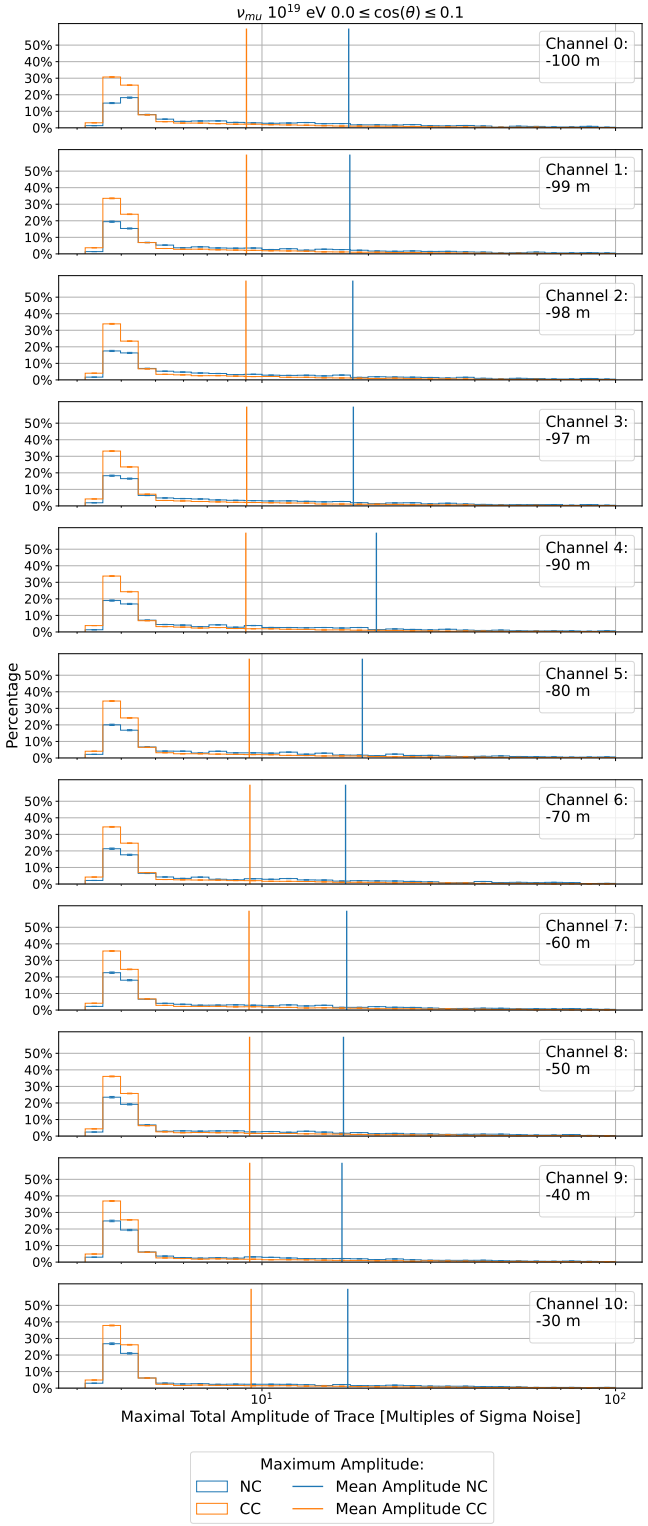

Figure 6.12: Histogram of the maximum amplitude value in the traces with simulated noise for each channel. In blue the distribution for NC events and in orange the one for CC events are shown. The two vertical lines indicate the mean maximum amplitude for NC events in blue and for CC events in orange.

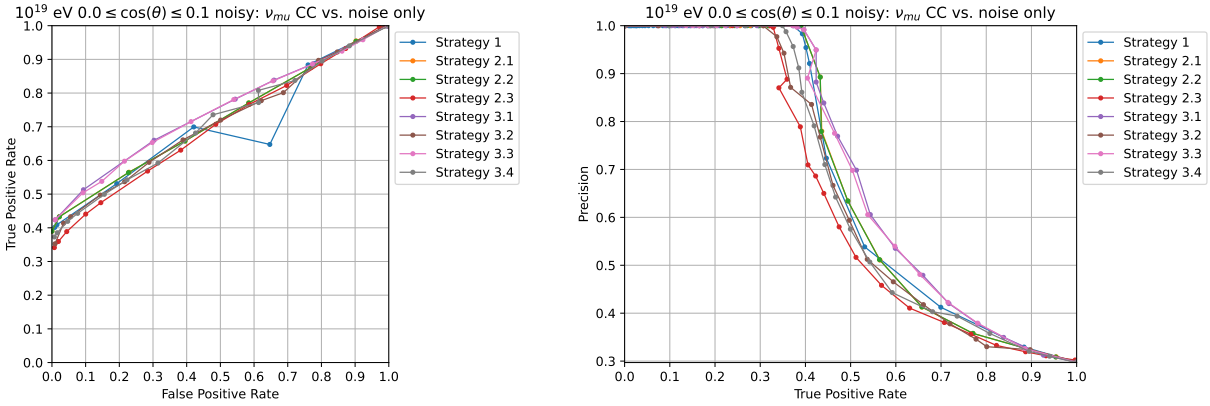

(a) (b)

Figure 6.13: lower limit of the ROC-curve (6.13a) and TPR-precision plot (6.13b) for the investigated strategies for separating CC muon neutrino events with added noise from traces which only contain noise without any shower signals.

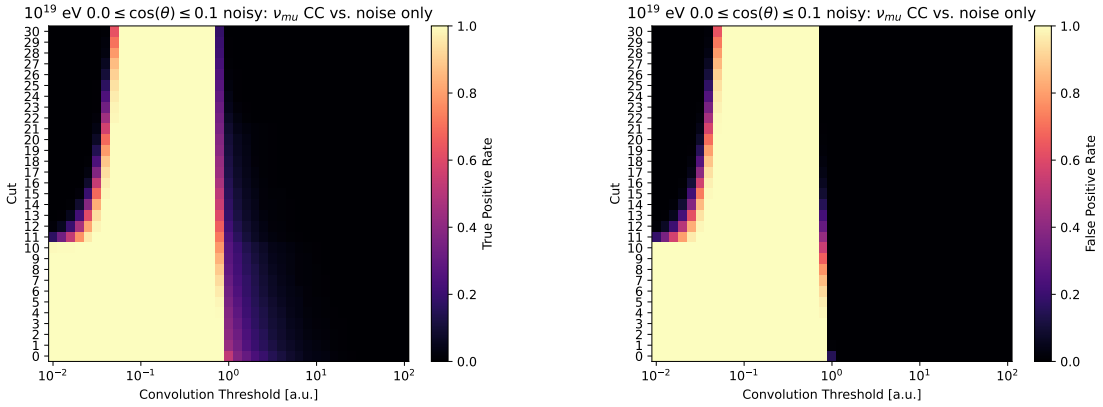

(a) (b)

Figure 6.14: Heat map of the true positive rate (6.14a) and false positive rate (6.14a) for Strategy 3.1 in dependence of the threshold on the x-axis and the cut value on the y-axis on differentiating CC muon neutrino events from pure noise.

peak on the plateau at 11 peaks is obtained. The interesting range of strategy parameters are thresholds slightly above 1 and low cut values or just below a threshold of one and higher cut values. This is a slim range of parameters and should be investigated in more detail. Hence, the data points making up the guidance line in Figure 6.13a are spaced out.

The achievable precision is shown in Figure 6.13b. With Strategy 3.3 a perfectly pure identification of CC events versus noise a TPR of 0.4 can be achieved. For higher TPR the precision declines steeply and levels off at the precision base line. The maximum achievable TPR for a pure selection is 0.38 with Strategy 3.3 which yields a lower performance limit.

Chapter 7

Station Multiplicity

An additional method to separate muon neutrino events is by investigating how many showers of an event are detected by how many stations of a radio neutrino detector. If showers are produced along an elongated path, that comes past multiple stations, several stations are triggered, also not necessarily by the same shower. Figure 7.1 shows an example event in the proposed IceCube-Gen2 Radio detector introduced in 3.4 from a muon neutrino at an energy of 10^{18} eV and an inclination of 0.087. The hybrid stations are shown in faded red and the shallow stations are shown in gray. The triggered stations are indicated in red, blue and green. The position of the simulated showers that have triggered the respective channels are shown in the equivalent colors. The position of the initial neutrino interaction is shown as a yellow star, indicating the direction of flight of the neutrino and propagation direction of the showers.

For the multiplicity of triggered station the surface and deep component were treated as individual stations. If both components fire their corresponding trigger, they would be counted as two triggering stations. An event is saved for each trigger, therefore the same event number appears several times in this data set. Subsequently, the number of events with the same event number was determined corresponding to the number of stations triggered by this event. This was done for all data sets mentioned in section 3.4. The key findings will be discussed in the following with regard to the muon neutrino selection.

7.1 Energy Dependence

Figure 7.2 shows a histogram of the number of triggered stations for initial muon neutrinos with inclinations in the range of 0.0 to 0.1. The different colored histograms show the different investigated initial energies between 10^{17} eV and $3.16 \cdot 10^{18}$ eV. The left plot shows the multiplicities for CC events and the right plot for NC events. The error bars show the 1σ uncertainty on the bar height that has been calculated using 5.1. where N_j is substituted by the total amount of investigated events N_{tot} and $\frac{N_{j,>2}}{N_j}$ by the probability to have triggered this amount of stations p_i. In both NC and CC events the distributions are shifted to lower number of triggered stations for lower energies. Due to the lower shower energy the produced radio signals are less powerful than those originating from high energetic showers and a trigger would not be set off for a lower energetic shower reducing the number of triggered stations. In the case of NC events usually less stations are triggered as for an CC events, since only one shower is present.

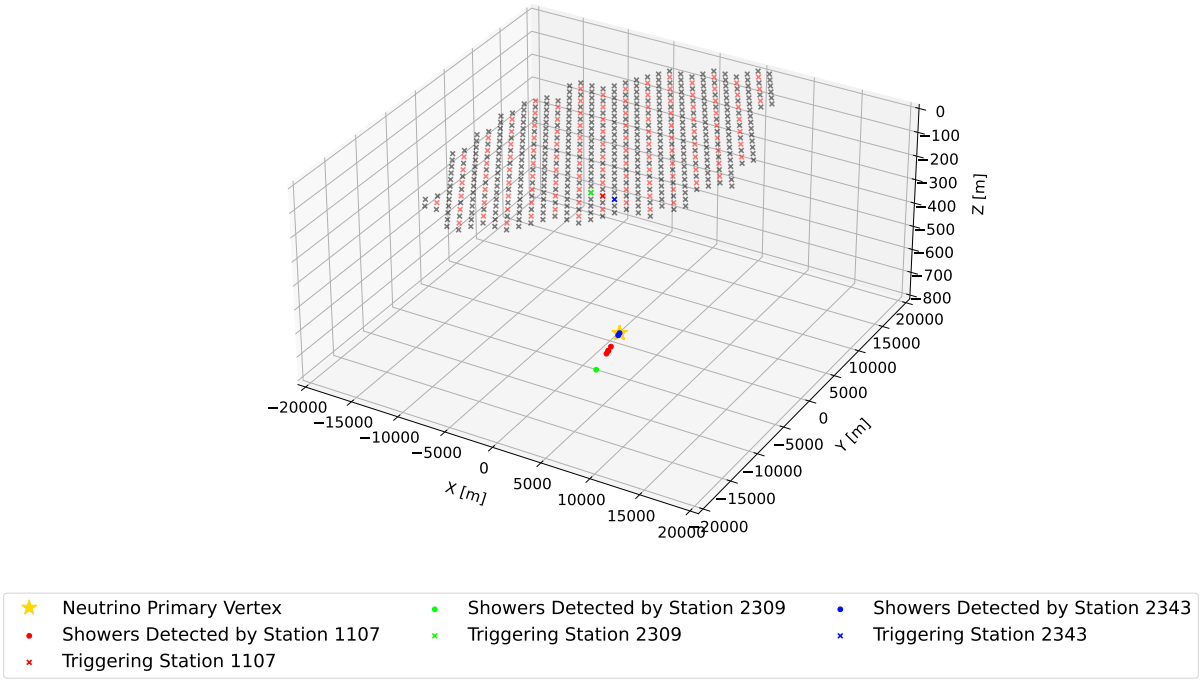

Figure 7.1: Example event, where multiple stations have been triggered. The detector consists of shallow (gray crosses) and hybrid stations (red). An initial muon neutrino interacts with the ice, indicated by the yellow star. From there, the created muon passes through the ice creating secondary showers, that can be detected by the stations. The three stations that have been triggered are shown in red, green and blue. The showers producing signals in the stations are shown in the corresponding colors.

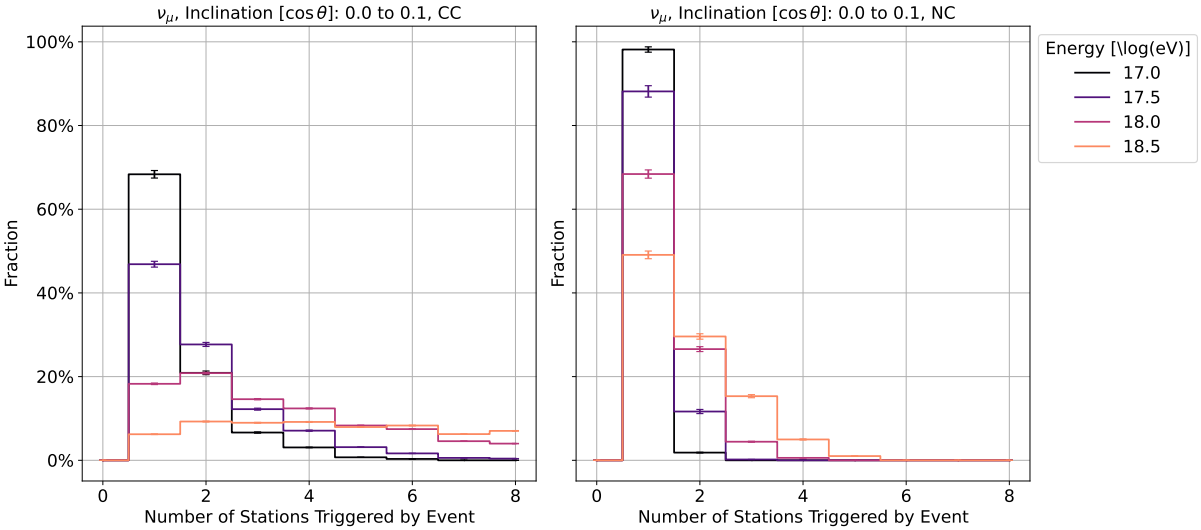

Figure 7.2: Multiplicity histogram of different initial neutrino energies for muon neutrinos at inclinations between 0.0 and 0.1. The left plot shows the distribution for CC events and the right one for NC events.

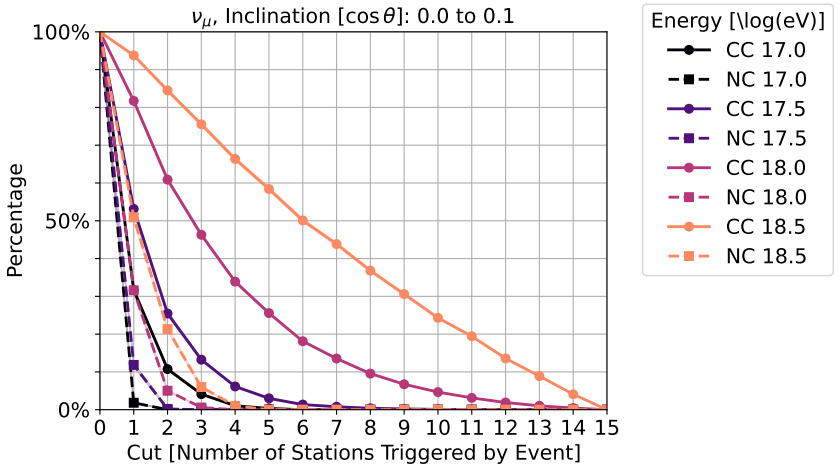

Figure 7.3: Percentage of events with more triggered stations than the cut value on the x-axis for different energies. The solid lines show the percentage of the CC events and the dashed lines for NC events.

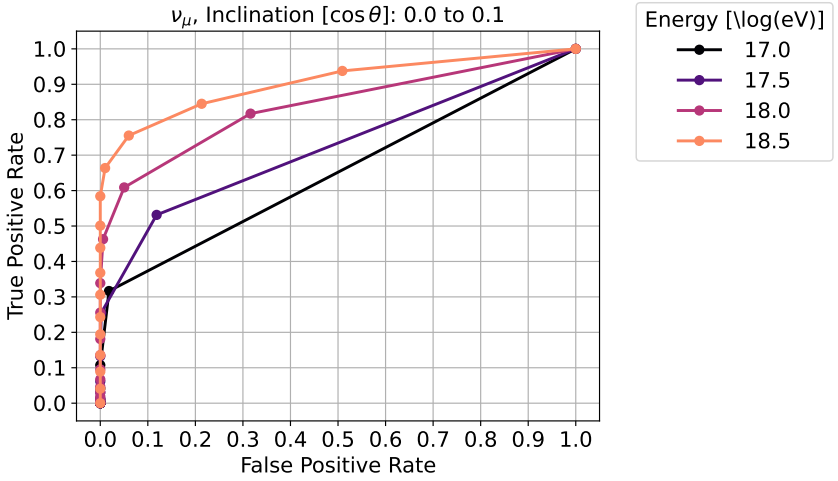

Figure 7.4: ROC-curve for the separation of CC interacting muon neutrinos from NC interacting muon neutrinos by the number of triggered stations for different energies.

To differentiate between an CC and a NC event by the number of triggered events one can define a cut value of number of station and check if the event has been triggered in more stations than the cut value. If that is the case, the events gets classified as a CC event. This method might not be perfect and there might exist NC events with a larger amount of triggered stations as well. Figure 7.3 shows the cut value on the x-axis and the percentage of events with more triggered stations than the cut value on the y-axis. The different colors indicate the energy. The results of the CC events are shown as circles and the results of the NC events as squares. For higher the energies, the the shape of the curve gets less curved. For CC events at an energy of $10^{18.5}$eV the number of events making the cut is approximately linear, since the distribution in Figure 7.2 is spread evenly. At a cut of zero the percentage is at 100 %, since an investigated event needs to be registered by at least one station. Beside this constraint, for the NC events, in general less events make the cut and their curve drops more steeply than for the NC events, since the main amount of NC events is registered in only a few stations. To separate CC from NC events as many CC events as possible should be selected correctly while at the same time only few NC

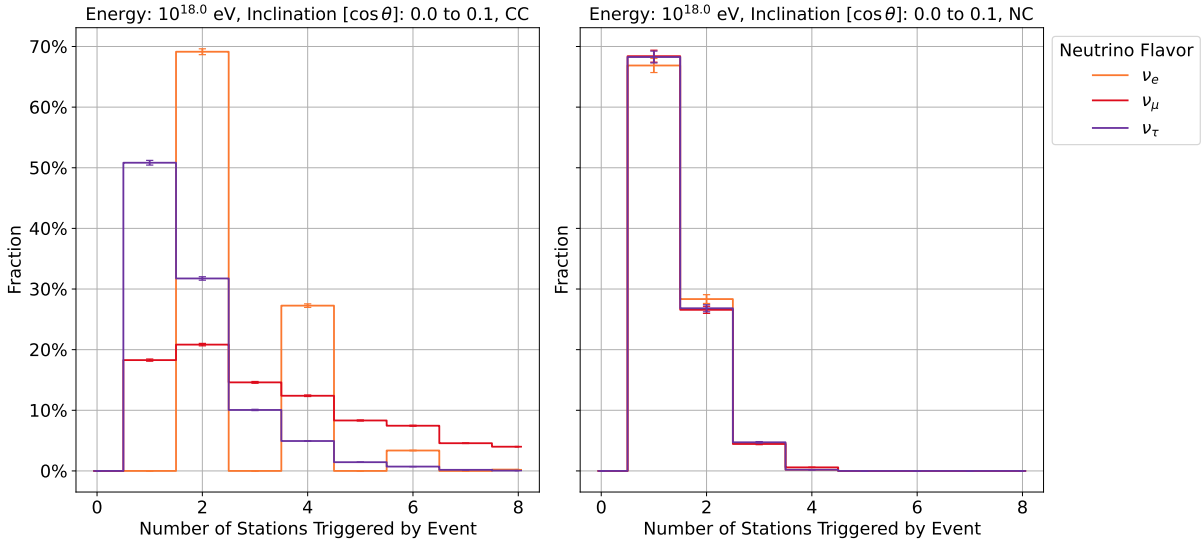

Figure 7.5: Multiplicity histogram for different neutrino flavors at inclinations between 0.0 and 0.1 and an initial energy of 10^{18} eV. The left plot shows the distribution for CC events and right one for NC events.

events should be selected. For the same parameters, these values are fixedly related. The shown percentage for CC events is in the following denoted as true positive rate and the percentage of NC events making the cut as false positive rate. One can again use the false positive rate and true positive rate as a measure of the performance of the classification. Figure 7.4 shown the true positive rate plotted against the false positive rate. The color of the point indicates the energy. While the points are connected for easier differentiation of the energies, there are no values in between the points possible, since the cut value is integer. In a lot of cases, the false positive rate is zero, where a perfectly pure CC event selection is possible. For muon neutrinos with an energy of 10^{17} eV a pure selection can be reaches with a cut value of 2. The resulting true positive rate is 10.8 %. A muon neutrino with an energy of $10^{17.5}$eV a pure selection can be achieved with a cut value of 3. Even tho the cut value is increased, the resulting True Positive value is increased as well to 13.2 %, since the distribution shown in Figure 7.2 shifts more to higher numbers of triggered station for CC events than NC events when the energy is increased. This trend continues for muon neutrinos at higher energies: At energies of 10^{18} eV a pure selection can be achieved with a cut value of 4 where 33.9 % of CC events are identified correctly. At $10^{18.5}$eV a cut of 5 leads to 50.1 % of correctly identified CC events without any selected NC events. The ability to identify muon neutrino events from neutral current interactions depends on the initial energy. The initial energy can be determined as shown in [56] and a cut value chosen accordingly. For higher energetic muon neutrinos the selection with this method improves.

7.2 Neutrino Flavors

Comparing different neutrino flavors at an energy of 10^{18} eV and an inclination in a range of 0.0 to 0.1 yields the plots shown in Figure 7.5. Where the charged current events are shown on the left and the NC events on the right. For the neutral current, the distributions for the three flavors look the same, since the simulation of NC events does not take the flavor into account.

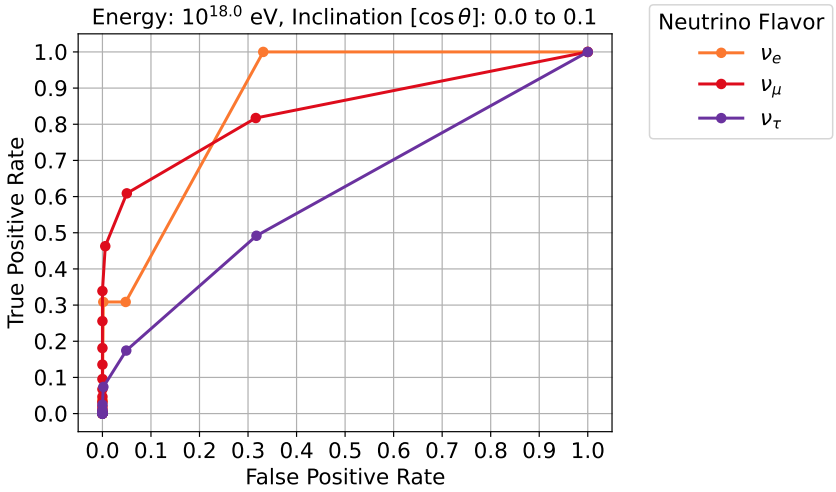

Figure 7.6: ROC-curve for the separation of CC events from NC events for each neutrino flavor t an energy of 10^{18} eV and inclinations between 0.0 and 0.1. The separation for electron neutrinos is not viable due to the superposition of the signals of their two simulated showers. The selection of CC interacting muon neutrinos from NC muon neutrinos yields overall higher TPR values than the separation of tau neutrinos.

For the CC events the distribution of electron neutrinos is striking, since it only takes even values of numbers of triggered stations. This can be explained, by the fact, that always the hadronic and electromagnetic showers are simulated. Since their position is at the same point, the ray tracing solution will always find a solution of none or both of them. If they are recognized by a second station or both the surface and deep component the number is increased by two. In reality the showers would overlap resulting in one signal measured by the detector, thus, the results of electon neutrinos interaction have to be treated with care and do not depict the physical reality.

For tau neutrinos shown in purple and muon neutrinos shown in red can be detected in an uneven number of stations was well. tau neutrinos tend to be detected by less stations than muon neutrinos. This can be explained by, the increased cross-sections for muon interactions and the overall longer lifetime of the muon as the secondary particle. Instead of differentiating muon neutrinos from NC events, this can also be done for electron and tau neutrinos. The results of the determined true positive rate in dependence of the false positive rate is shown in Figure 7.6. To obtain a perfectly pure selection of CC events in all three cases a cut value of at least four needs to be used in the case of electron neutrino selection 3.6 % of all CC events are correctly selected. In the case of muon neutrinos as sown before there are 33.9 % left and in the case of tau neutrinos 2.4 %. Instead of this rigorous selection more than three triggered stations could be demanded. In that case the amount of correctly identified events increases to 30.9 %, 46.3 % and 7.4 % for electron, muon and tau neutrinos respectively. In doing so the selection becomes contaminated and a fraction of the NC events are also considered CC events. Thats the case for 0.2 %, 0.6 % and 0.2 % of the NC events. On the application of real events additionally, the fraction between NC and CC events needs to be considered to conclude to the percentual contamination. With respect to the subsequent analysis a final decision on the cut can be made. Since the distributions of the number of triggered stations are still quite different for CC interactions of different flavors, the separation of muon neutrinos

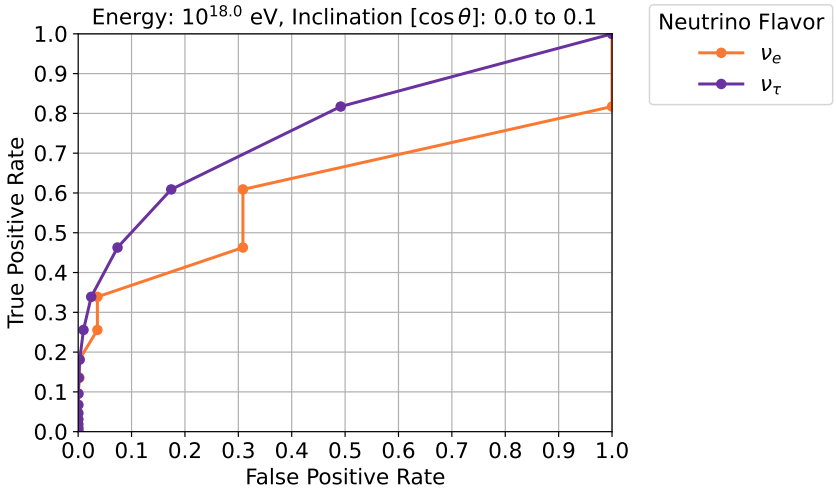

Figure 7.7: ROC-curve for separating CC muon neutrinos from CC electron neutrinos (orange) and tau neutrinos (purple) based on the station multiplicity.

from electron and tau neutrinos can be investigated by the same approach of selecting events with several stations triggered by one event. Figure 7.7 shows the true positive rate on the y-axis, i.e the amount of muon neutrinos correctly selected. On the y-axis the false positive rate is shown, which in this context, is the amount of CC electron or tau events, that make the cut. In the shape of the selection against the electron neutrino CC events steps are visible. Since only every second bin contains nonzero entries, an increase of the cut from an event to an uneven number leads to the same false positive rate. The curve describing the selection against tau neutrinos shown in purple is smoother. Its true positive rate is always higher than for the selection against electron neutrinos.

7.3 Inclination Dependence

In the following we will focus on the impact of the inclination of the incoming neutrino. As shown in section 4.3 the field of view decreases for steeper inclinations, thus the number of triggered stations should decrease as well. For this investigation four inclinations ranges are investigated. The distribution for muon neutrinos with an energy of 10^{18} eV is shown in Figure 7.8. Neutrinos with an inclination below 0 are surpassing the earth and are from the view of the detector up going. As an example an inclination range from -0.4 to -0.3 is investigated in blue. Inclinations in a range from 0.0 to 0.1 are quite horizontal but always coming from above and have not surpassed the earth. Additionally the inclination ranges from 0.4 to 0.5 and 0.8 to 0.9 are investigated. The former inclination was also used for the simulation for the Lonely String Detector and the second one provides an additional investigated value in a reasonable inclination range.

By investigating the number of events that a NC event triggers, conclusion on the behavior of a single shower can be drawn, since only one shower is present to trigger several stations. Showers with the highest investigated inclination are only seen in one station. For smaller angle values the distribution shifts towards more triggered stations. To explain this, a qualitative estimate can be considered: Considering the station setup as shown on 4.3, it can be assumed that the majority of the showers are produced at a lower point than the position of the station at a depth of only 100 m. Neglecting the bending of the rays,

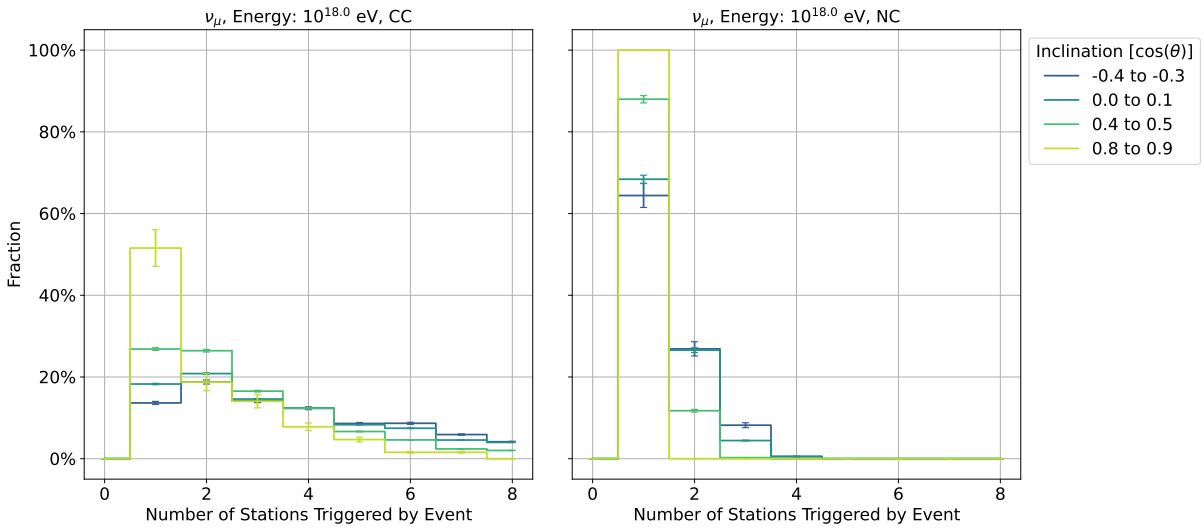

Figure 7.8: Multiplicity histogram for different inclinations and an initial energy of 10^{18} eV. The shown distributions originate from muon neutrino interactions. The left plot shows the distribution for CC events and right one for NC events.

the Cherenkov cone should face in upwards direction to be able to create a signal. At an inclination of more than 0.57 corresponding to an inclination of 55° the whole Cherenkov cone is facing downwards. This is the case for the inclinations of 0.8 to 0.9. Only in rare cases, where the interaction happens above the antenna, an event is detected. By increasing the inclination a larger part of the Cherenkov cone is facing upwards. One can imagine a conical section parallel to the ices surface through the interaction point. radio waves emitted in the upper part of the Cherenkov cone have, leaving ray bending and attenuation aside, a chance to be detected. At an inclination of 0 this is the case for half of the cone. For neutrinos with an inclination of less than -0.57 the whole cone is facing upwards. In theory this would lead to a maximization of triggered stations. In reality this scenario is suppressed by the attenuation of the earth. Ray bending and attenuation lead to an additional reduction in the number of triggered stations.

For the CC interactions at different inclinations in principle the same argumentation holds true, but several showers are produced, shifting the distribution to a higher number of triggered stations. Two effects increase the number of triggered stations: Is the inclination is more horizontal the resulting muon travels a longer path through the ice and has more chances for energy losses, triggering stations along its way. If the inclination is more vertical, the path through the volume is shorter, but for smaller inclinations the number of triggered stations per shower is larger, increasing the number of triggered stations as well. The capability to select muon neutrinos interacting via a CC interaction from NC interactions by the number of triggered stations is investigated depending on the inclination angle again with regards to the true positive rate and false positive rate. The results are shown in 7.9. For all investigated inclinations a perfectly pure selection can be obtained. At the largest investigated inclination range of 0.8 to 0.9 demanding at least two triggered stations is sufficient to clearly identify a CC event. At this cut 48.4 % of CC events are correctly identified. For the more shallow inclination range of 0.4 to 0.5 at a cut value of three 30.2 % of the CC events are correctly identified as such. For the negative inclinations between -0.4 and -0.3 a cut value of 4 yields a perfect selection of 41.1 %.

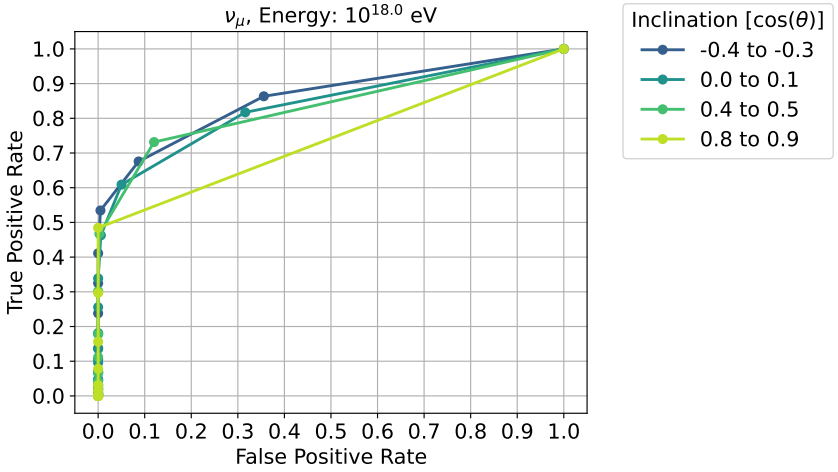

Figure 7.9: ROC-curve for separating CC muon neutrinos from CC muon neutrinos from NC muon neutrinos based on the station multiplicity for different inclinations.

Chapter 8

Conclusion

This thesis provides first insights in the identification of neutrino flavors in radio neutrino detectors and the influence of various parameters. Therefor, neutrino events were simulated using NuRadioMC [36] and PROPOSAL [38] was used for the simulation of secondary muons and taus.

By examining the shower energy distribution of the simulated neutrinos, it could be observed that showers from neutral current (NC) events tend to have higher energies than the showers from charged current (CC) muon and tau neutrinos which are mainly produced by energy losses of the leptons along their path. The shapes of the simulated energy spectra have been interpreted and explained. A reduction of the initial neutrino energy leads to a reduction of the mean shower energy. The number of showers per event is always one for NC events but increases for CC interacting muon and tau neutrinos, due to the interaction of the charged secondary leptons in the ice. Concluding, the CC muon neutrino interactions yield the highest mean number of showers per event. This feature is exploited to separate CC muon neutrino interactions from NC neutrino interactions.

Following, the response of these events in a simplified detector station similar to the RNO-G power string was simulated for multiple neutrino parameters. The signatures of different flavoured neutrinos with varied parameters as seen in a single antenna was investigated with regard to the spatial sensitivity. Three main reasons have been determined that limit the field of view of the detector: If the energy of a shower is too low the recorded signal does not exceed the trigger. Additional attenuation in the ice and signal reduction due to a long path length reduces the detectability at large distances for showers with smaller energies stemming from neutrinos with lower energy. The signal amplitude is also reduced and spread out if the signal path is too far off the Cherenkov cone. This is more often the case for steeper initial neutrino inclinations, leading to a reduction in the viewing angle of the antenna. Lastly, showers happening in the shadow zone of the antenna are not seen due to the changing index of refraction no possible path to the antenna is found by the ray-tracer.

To actually differentiate CC muon neutrinos from NC neutrinos two methods were introduced. The first approach is based on shower signal identification on the measured traces in a single station. Eight different strategies were developed in order to identify the shower signals. If more peaks are found on the combined traces than a set cut value the event is classified as a CC muon neutrino event.

The performance of the strategies was investigated in dependence of the threshold and cut value. The best performing strategy is dependent on the precision and efficiency that is supposed to be achieved. Generalized, Strategy 2.3 and 1 yielded the highest precision at reasonably high true positive rates. For the separation of CC muon neutrinos from NC neutrinos at an energy of 10^{19} eV and inclinations between 0.0 and 0.1 a precision above 0.99 can be achieved with Strategy 2.3 up to a true positive rate of 0.5. The normalization of the trace before the determination of the maxima improves the performance in both precision and effectiveness. The increase of the number of found maxima between two peaks from one to two downgrades the performance. The use of the convolution of the template with the trace does not yield the best results in CC from NC muon neutrino event separation on noiseless traces. The approach of a one-fits-all template might not have been the optimal approach, as suggested by the large range of determined fit parameters. The method could be improved by using several templates on the trace to obtain differently shaped signals more reliably.

For an inclination between 0.4 and 0.5 a precision above 0.99 can be achieved for true positive rates of up to 0.5 with Strategy 2.3, which is an improvement compared to the more shallow inclination range. In order to achieve this, a cut value of at least 5 found peaks on all traces needs to be chosen, since the upper channels record less peaks for higher inclinations. In general the cut value should be chosen in dependence of the inclination angle of the neutrino. To improve the method further for high inclinations, only the deepest channels could be taken into account, since the upper channels do not contribute substantial to the total amount of measured signals. Using these strategies to differentiate CC muon neutrinos from CC electron or tau neutrinos only gave mediocre results: in both cases a perfectly pure selection is not possible for any of the investigated thresholds and cut values due to the uneven contamination of the CC and NC events caused by triggering noise. The differentiation between noisy CC muon neutrino events and noise only events yields a lower limit of a true positive rate of 0.38 for perfectly pure selection using Strategy 3.3. A more reasonable comparison between CC and NC events could be obtained by comparing the event ID of the triggered events in the noisy data set with the noiseless data set and selecting only the events that would have fired the trigger by themselves as input data sets of the classifier.

The performance of this differentiation technique is limited by the amount of CC events that do show more than two shower signals on the trace. Since this is not mandatory in a second approach the multiplicity of triggered stations in the proposed IceCube-Gen2 Radio array was used as a classification method. Especially for the energy of 10^{18} eV the classification improved drastically: By separating CC muon neutrino events from NC events based on the recorded traces a perfectly pure selection, in the scope of the amount of investigated events, can be achieved with a selection of up to 29 % of the CC events, while the selection based on the multiplicity yields a selection of 33.9 %.

The two investigated methods are not yet sophisticated enough to acquire quantitative knowledge of the astrophysical flavor composition of high and ultra high energetic neutrinos by themselves. Due to the expected rareness of detected neutrinos a more certain method for the flavor differentiation is required. The approach of counting the number of produced showers has been shown to be feasible to differentiate CC muon neutrinos

from NC events. To obtain an applicable method in the future the evident next step is the combination of the two approaches: A combination of the detected signals on the traces of multiple stations is expected to yield an overall improvement of the ability of neutrino flavor differentiation. When quantifying the performance of a further developed classifier, as a basis a spectrum should be used, where the ratio of neutrino inclinations and energies is realistic. Ultimately the impact of background events like muons needs to be taken into account as well.

Appendix A

Shrink Wrap Algorithm

To visually compare the results in chapter 6 an algorithm is needed to connect the edge points of a point cluster. The algorithm to obtain these guidance lines is explained in this chapter.

The convex hull of a set of points can be obtained by using the Jarvis March algorithms also called gift wrapping algorithm [58, p. 1037]. Therefor the lowest point of the set is selected as the first point of the hull. The angles between the x-axis and the connecting line between the first selected point and any other point are calculated. The point which leads to the smallest angle is selected as second point on the hull. By always choosing the next point with the smallest angle compared to the direction of the last two connected points, the hull is determined. When the first point is selected again, the convex hull has been found. This method can be imagined like wrapping gift wrap around the points, hence the name gift wrapping algorithm. This is implemented in the python package SciPy as scipy.spatial.ConvexHull [52]. In Figure A.1 the achieved ture positive rates (TPR) and false positive rates (FPR) on differentiating muon neutrinos interacting via charged current from the ones interacting via neutral current at energies of 10^{19} eV and inclinations of 0.0 to 0.1 are shown as an example. The resulting convex hull is displayed in blue. The convex hull is not suited to approximate the upper limit of the TPR: in between FPRs of 0 and 0.5 the TPR along the blue line cannot be achieved. This algorithm does not suit the needs of determining a guidance line, since the guidance line is not necessarily convex. Nevertheless it was used as an inspiration.

The python code of the Shrink Wrap Algorithm, which adapts closer to the point cloud is shown in Listing A.1. The Shrink Wrap Function takes three parameters. The first parameter is a numpy array DATA, containing the data points of which the hull should be found. It has a dimension of two with a size of (2,N), where the first dimension contains the X and Y position of the points and the second dimension has the length of the amount of points N. The values of X and Y are supposed to be positive. The second parameter is the maximum distance between two points on the hull. The `min_angle` defines the minimum angle spanned by three consecutive points on the hull.

At first the point closest to the origin at (0,0) is chosen. It makes the first point on hull. `angle1` is set to zero. This can be done, since the first point is the closest to the origin, thus in the angle area from 2π to $\frac{3\pi}{2}$ around the first point no other points can be. In the variable i the amount of already found points is stored. After the first point

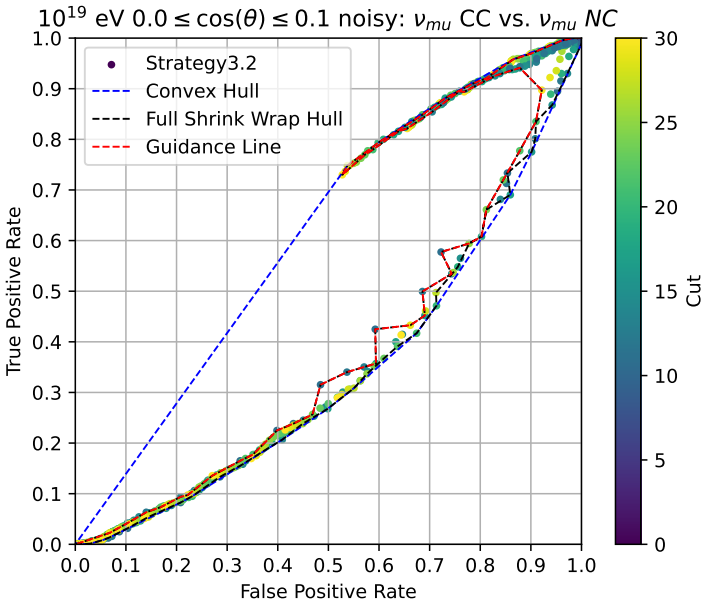

Figure A.1: Example of the determined hull around the TPR and FPR points of muon neutrino noisy events at an energy of 10^{19} eV and an inclination between 0.0 to 0.1. In blue the convex hull around the data points is shown, which does not follow the shape of the point cloud in the upper half of the hull at small FPRs. In black the hull determined with the Shrink Wrap Algorithm is shown which often overlaps with the convex hull in the lower part of the hull. The upper part of the determined Shrink Wrap Hull is shown in red. This part is plotted as a visual guidance line in the plots in chapter 6.

is selected, the other points are added repeatedly to the list of hull points. First, a mask is defined where points are selected that are closer to the last selected point than the `max_distance` but cannot lie at the same position as the already selected point. Else, two points at the same position would always select the other one at the same position and the hull would not enhance.

If there are no points found that fulfill this condition, the distance from the last hull point to all the points is calculated. If the distance of the last selected point to another is zero, the value is set to 'not a number' (nan) to exclude them in the next step. The index of the first minimum of the distances is determined while ignoring all nans. Thus, the position of the nearest point, that is not at the same position is the only index saved in the mask array. This special treatment of large distances between points is helpful, in the case of determining the guidance line in the plots where the precision is plotted against the TPR as shown for example in Figure 6.3b. The distance between the first point and the second point on the y-axis can be quite large relative to the scattered points in the upper part of the plot. Thus increasing the `max_distance` to a value large enough to cross this distance would lead to shortcuts in the path around the points. Since these large distances often occur between the first points, this special case is considered. If at one point a distance closer than the `max_distance` is found, one will always have a point close enough, namely the previous one.

In the next step the angles between the last added hull point and all points that are selected by the masking are calculated relative to the x-axis in the array `angle2`. In Figure A.2 the previously added point P_2 and another example point P_3 are shown. The

angle between the X-direction and their connecting line `angle2` is shown in red as α_2. The angle between the second last point P_1 and P_2 is denoted as α_1. In the case of P_2 being the first selected point of the hull, α_1 was defined to have a value of 0. Next, the angle `tot_angle` between three consecutive points on the hull shown in violet is calculated: the line between the point P_1 and P_2 can be extended beyond P_2 indicated as a green arrow. The angle around P_2 between these two lines, shown in green is always π. To obtain the `tot_angle` additionally the orange angle between the green line and the line connecting P_2 and P_3 needs to be determined, which is the difference of `angle1` and `angle2`. Finally it holds

$$\text{tot\_angle} = \pi + \alpha_2 - \alpha_1. \tag{A.1}$$

To stay in the domain of $[0,2\pi)$, the modulo of 2π is used.

Before the point with the minimum angle is chosen as the next hull point, we need to account for one edge case, where this technique leads to undesired results. This edge case is shown in Figure A.3. From the first point P_1, only the points P_2 and P_4 can be reached since the point P_3 is too far away and would not be selected in the mask. Consequently, P_2 would be added as the second point. In the next iteration P_3 would be added and from P_3 the point P_4 would be added to the hull, since this leads to the smallest angle at P_3 and P_1 is too far away. This results in a path with a crossing. Such hulls shall be avoided.

For this reason a minimal angle `min_angle` is used. If `tot_angle` is smaller than this angle 2π will be added to `tot_angle` to exclude it to be selected next. If afterwards the minimum angle is selected it will be the one closest but bigger than the `min_angle`. In the case of the example it would be the point P_5. In all the determined guidance lines in this thesis a `min_angle` of $\frac{\pi}{2.5}$ was used. To be certain that a crossing is not possible, a minimum angle of $\frac{\pi}{2}$ is required. Then again, this also restricts possible sharp indentations in the hull, where the hull does not necessarily crosses. The value of $\frac{\pi}{2.5}$ leads to reasonable results in all investigated cases. After the 2π are added to `tot_angle` smaller than the `min_angle`, the point with the then smallest `tot_angle` is appended to the array of hull points. `angle1` is updated with `angle2`, such, that in the next iteration `tot_angle` can be calculated correctly for the next point.

The termination condition is split in three conditions for better comprehension. At first, it is checked if the newest hull point is already present in the list of hull points excluding the last six. This gives a minimal number of points making up a hull. It is assumed that a sufficient amount of points is present and that the points are far enough spread that a hull of this size can be created. Next, it is checked if the second to last point is present in the hull except for the last seven points. If the hull arrives at a point, that has been visited before, it can arrive in a different angle, leading to another following hull point. This can be imagined, having a look at Figure A.1. If there would be less points in the tip of the hull, at a FPR of 0.52, the hull would take the same points to the tip as back to higher FPRs. Thus, the order of the points on the hull is important. In the last condition this is checked: the indices of the points, that correspond to the last selected point are determined in the list of already determined hull points and checked if the index one before them is in the list of indices corresponding to the second to last point. If this is the case both points have been selected in a row. This fixes the `angle1` and a further determination of hull

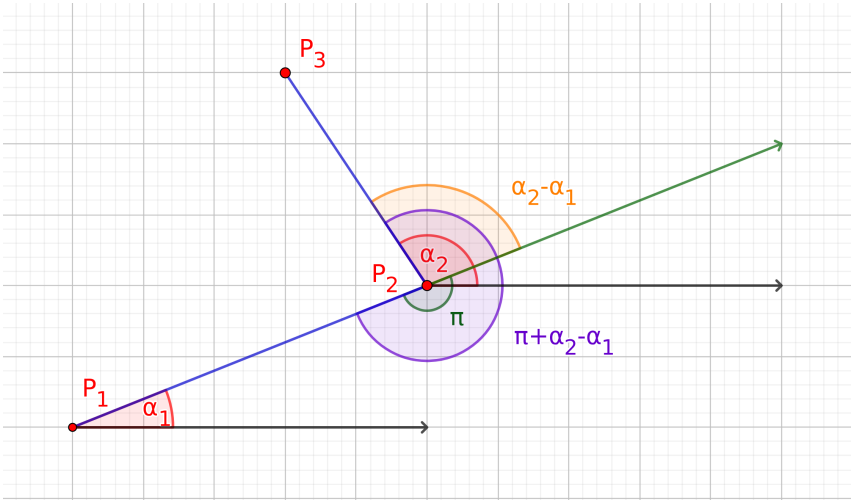

Figure A.2: Depiction of the calculation of `tot_angle` (violet) spanned by three points P_1, P_2 and P_3. The angles between the x-axis and two connected points are shown in red. By dividing the `tot_angle` by the extension of the connecting line of P_1 and P_2 `tot_angle` can be composed by an angle of π (green) and $\alpha_2 - \alpha_1$ (orange).

points would lead to the same lap of points. At this point the hull points are returned by the function. If the termination condition is not fulfilled, i is increased by one, since another point has been found and the next point is searched. The path of the determined hull points is shown in Figure A.1 in black. In the lower part of the determined hull, it often overlaps with the results of the convex hull, since the determined hull is mainly convex. For a visual comparison of the strategies only the maximal achievable True positive rates for each FPR is of interest. Thus, only the upper part of the hull is shown in red.

To select this part, a minimum and maximum index of the returned hull points is defined in the plotting script:

```
hull_min=np.argwhere(hull[:,0] == np.max(hull[:,0]))[np.argmax(hull[np.argwhere(hull[:,0] ==
    np.max(hull[:,0])),1])][0]
hull_max=np.where(hull[hull_min:,0]<0.01,hull[hull_min:,1],-1).argmax()+hull_min+1
```

`hull_min` is the index of the point at the most upper top of the hull. The index of the points most to the right are selected. Since the points are clustered there, it can be assumed, that there are several points with the same maximum FPR value. From these points the uppermost point is chosen as a start point. This procedure is feasible, since in the case of the points in Figure 6.3b the point one would like to start with it not necessarily the one furthest from the origin. To obtain `hull_max` only the points found after `hull_min` are considered. From these, the points with an x-value smaller 0.01 are chosen. Of these the position the maximum y-value is selected. Additionally, the index `hull_min` has to be added again, to obtain the correct value with respect to the length of the hull point array. An additional point further along the hull line is plotted to get closer to the y-axis, yielding the red dotted line in A.1.

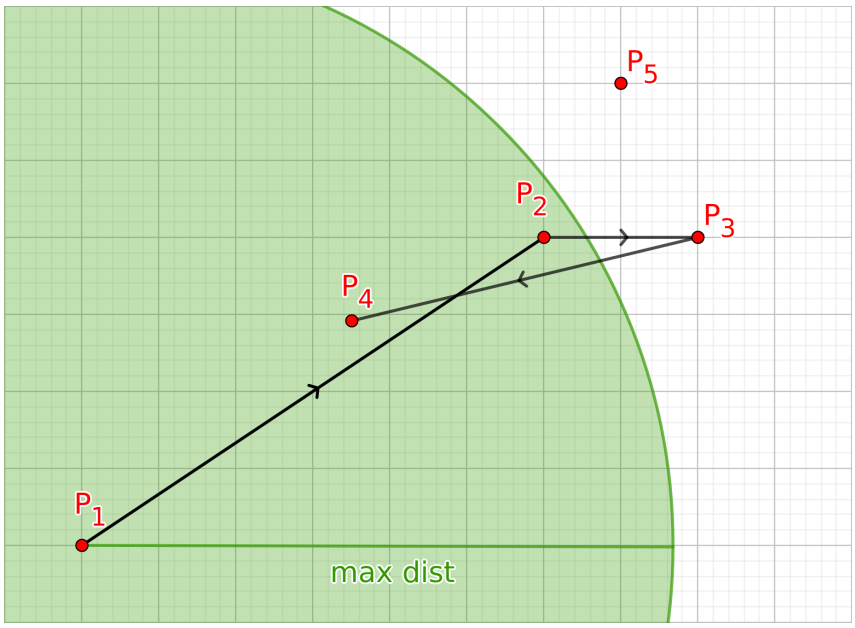

Figure A.3: Depiction of an edge case, where the hull would cross itself if the `tot_angle` is not checked for a minimal value. The green circle shows the range of the maximum distance around P_1

```
import numpy as np

def shrink_wrap(DATA,max_dist,min_angle):
    hull=np.array([DATA[:,np.nanargmin(np.sqrt(DATA[0,:]**2+DATA[1,:]**2))]])
    angle1=0.0
    i=1
    while True:
        mask=np.where((np.sqrt((DATA[0,:]-hull[i-1,0])**2+(DATA[1,:]-hull[i-1,1])**2)<max_dist
            ) & (np.sqrt((DATA[0,:]-hull[i-1,0])**2+(DATA[1,:]-hull[i-1,1])**2)>0))[0]
        if len(mask)==0:
            dists=np.sqrt((DATA[0,:]-hull[i-1,0])**2+(DATA[1,:]-hull[i-1,1])**2)
            dists=np.where(dists==0,np.nan,dists)
            mask=[np.nanargmin(dists)]
        angle2=np.arctan2([DATA[1,mask]]-hull[i-1,1],[DATA[0,mask]-hull[i-1,0]])[0]
        tot_angle=(np.pi+angle2-angle1)%(2*np.pi)
        tot_angle=np.where(tot_angle <= min_angle,tot_angle+2*np.pi,tot_angle)
        hull=np.append(hull,[DATA[:,mask][:,np.nanargmin(tot_angle)]],axis=0)
        angle1=angle2[np.nanargmin(tot_angle)]
        if np.any(np.all(hull[i] == hull[:-6], axis=1)):
            if np.any(np.all(hull[i-1] == hull[:-7], axis=1)):
                if np.any(np.in1d(np.array(np.where(np.all(hull[i] == hull[:-6], axis=1)))-1,
                    np.array((np.where(np.all(hull[i-1] == hull[:-7], axis=1))))):
                        return hull
        i=i+1
```

Listing A.1: Shrink Wrap Algorithm

Appendix B

Supplementary Plots

Complementary to section 4.1 the energy spectra for muon neutrinos (B.1) and tau neutrinos (B.2) are broken down into the interaction types used by PROPOSAL.

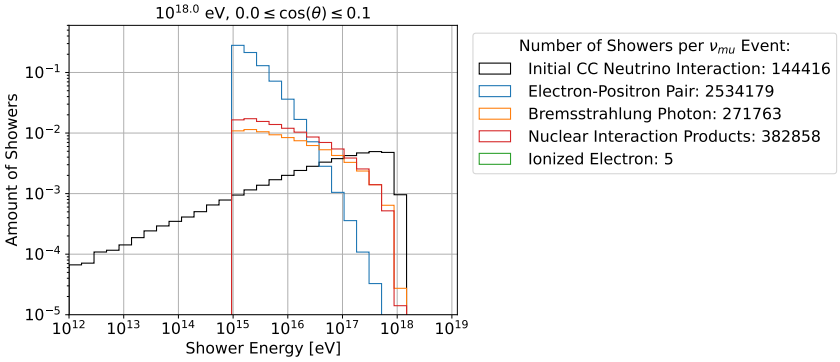

(a)

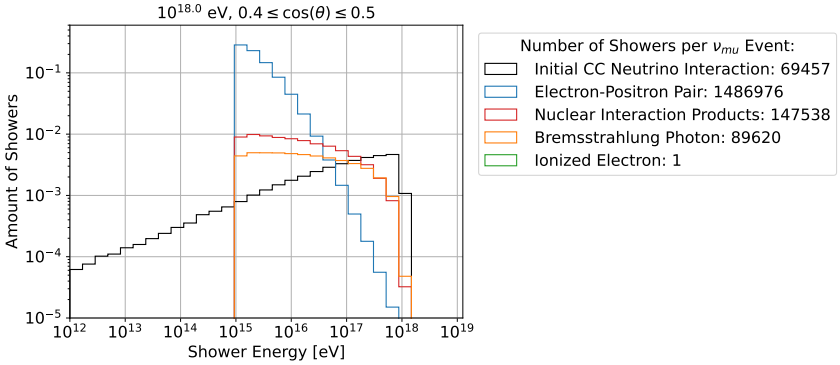

(b)

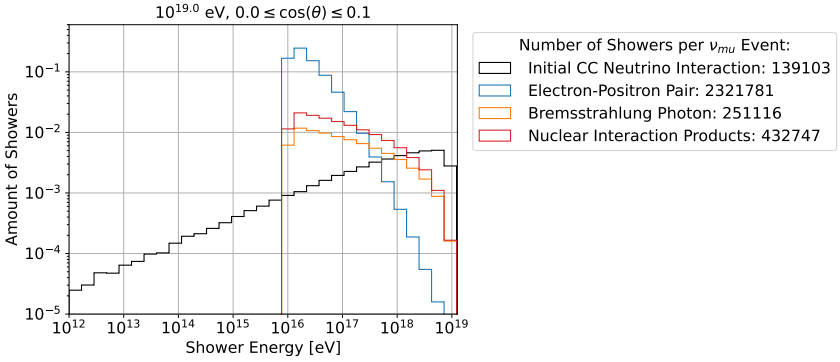

(c)

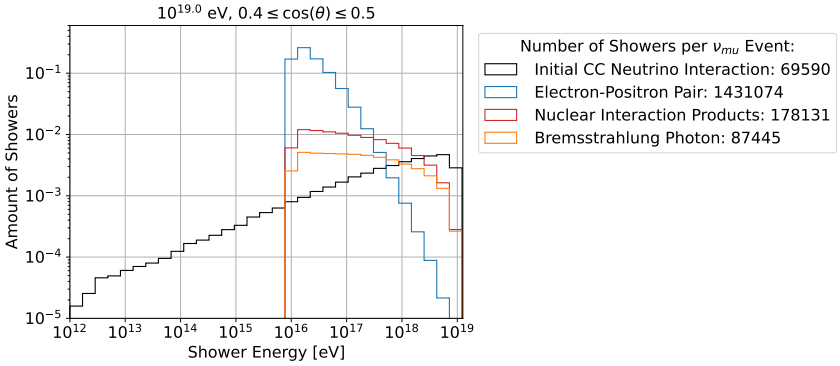

(d)

Figure B.1: Energy spectrum of muon neutrino interactions split into the PROPOSAL interaction types. The neutrino energy and inclination is given in the plot title. Ionized Electrons are not shows due to the y-axis plot range.

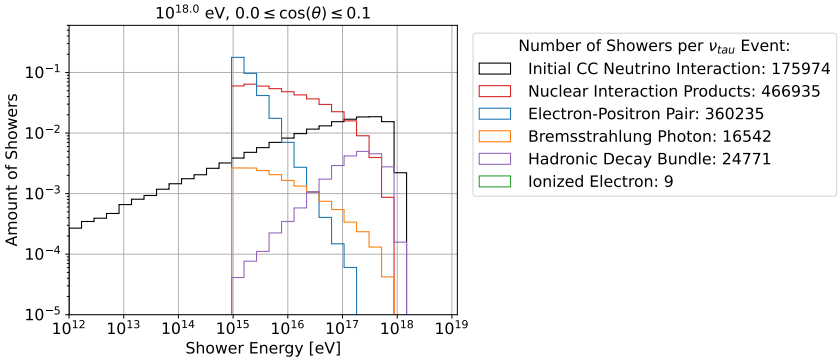

(a)

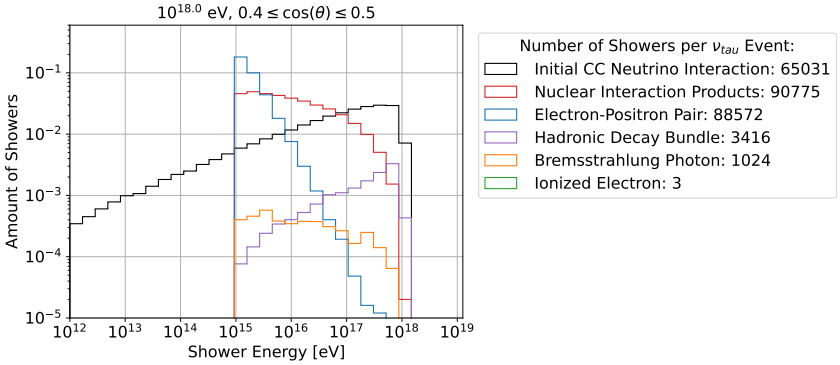

(b)

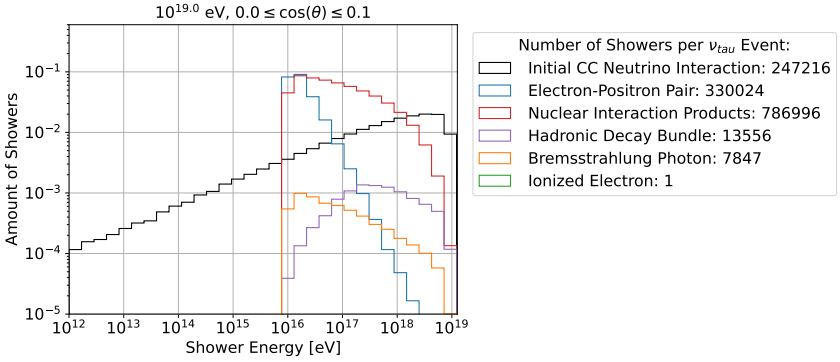

(c)

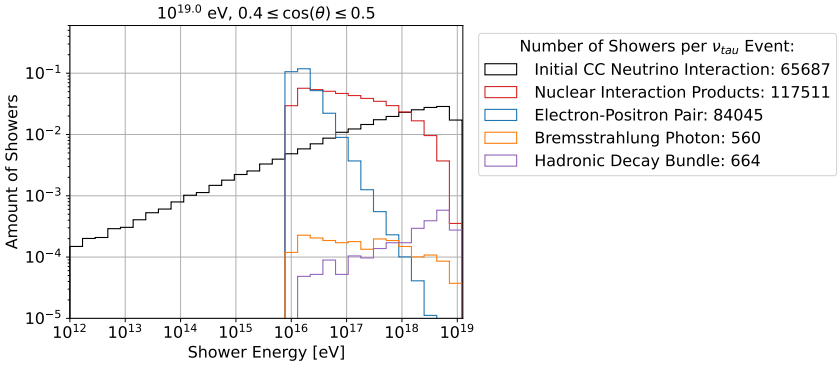

(d)

Figure B.2: Energy spectrum of tau neutrino interactions split into the PROPOSAL interaction types. The neutrino energy and inclination is given in the plot title. Ionized Electrons are not shows due to the y-axis plot range.

Bibliography

[1] M. Ackermann et al. 'High-Energy and Ultra-High-Energy Neutrinos', 2022. doi: 10.48550/arXiv.2203.08096. 2203.08096

[2] R. Bousso et al. 'Snowmass White Paper: Quantum Aspects of Black Holes and the Emergence of Spacetime', 2022. doi:10.48550/arXiv.2201.03096. 2201.03096

[3] G. Decerprit et al. 'Constraints on the origin of ultra-high-energy cosmic rays from cosmogenic neutrinos and photons'. Astronomy & Astrophysics, volume 535:p. A66, 2011. ISSN 0004-6361, 1432-0746. doi:10.1051/0004-6361/201117673. 1107.3722

[4] S. Barwick et al. 'Radio Detection of High Energy Neutrinos in Ice', 2023. doi: 10.48550/arXiv.2208.04971. 2208.04971

[5] M. Ackermann et al. 'Neutrino emission from the direction of the blazar TXS 0506+056 prior to the IceCube-170922A alert'. Science, volume 361(6398):pp. 147–151, 2018. ISSN 0036-8075, 1095-9203. doi:10.1126/science.aat2890. 1807.08794

[6] J. Stettner. 'Measurement of the Diffuse Astrophysical Muon-Neutrino Spectrum with Ten Years of IceCube Data', 2019. doi:10.48550/arXiv.1908.09551. 1908.09551

[7] A. Coleman et al. 'Nu_e Flavor Fraction Sensitivity Using In-Ice Radio', Presentation, 2023

[8] P. Allison et al. 'A low-threshold ultrahigh-energy neutrino search with the Askaryan Radio Array'. Physical Review D, volume 105(12):p. 122006, 2022. ISSN 2470-0010, 2470-0029. doi:10.1103/PhysRevD.105.122006. 2202.07080

[9] A. Anker et al. 'White Paper: ARIANNA-200 high energy neutrino telescope', 2020. doi:10.48550/arXiv.2004.09841. 2004.09841

[10] J. A. Aguilar et al. 'Design and Sensitivity of the Radio Neutrino Observatory in Greenland (RNO-G)'. Journal of Instrumentation, volume 16(03):p. P03025, 2021. ISSN 1748-0221. doi:10.1088/1748-0221/16/03/P03025. 2010.12279

[11] A. Nelles. 'Towards IceCube-Gen2: Plans for the in-ice radio array'. In 'Proceedings of 9th International Workshop on Acoustic and Radio EeV Neutrino Detection Activities — PoS(ARENA2022)', (p. 057). Sissa Medialab, Santiago de Compostela, Spain, 2023. doi:10.22323/1.424.0057

[12] N. Schmitz. Neutrinophysik. Teubner Studienbücher Physik. Vieweg+Teubner Verlag, Wiesbaden, 1997. ISBN 978-3-519-03236-6 978-3-322-80114-2. doi:10.1007/978-3-322-80114-2

[13] R. L. Workman et al. 'Review of Particle Physics'. Progress of Theoretical and Experimental Physics, volume 2022(8):p. 083C01, 2022. ISSN 2050-3911. doi:10.1093/ptep/ptac097

[14] K. Hirata et al. 'Observation of a neutrino burst from the supernova SN1987A'. Physical Review Letters, volume 58(14):pp. 1490–1493, 1987. ISSN 0031-9007. doi:10.1103/PhysRevLett.58.1490

[15] K. Zuber. Neutrino Physics. Series in High Energy Physics, Cosmology and Gravitation. Taylor and Francis Group, 1 edition, 2004. ISBN 0-7503-0750-1

[16] A. Müller. 'GZK-cutoff'. https://www.spektrum.de/lexikon/astronomie/gzk-cutoff/163, 2023

[17] U. F. Katz et al. 'High-Energy Neutrino Astrophysics: Status and Perspectives'. Progress in Particle and Nuclear Physics, volume 67(3):pp. 651–704, 2012. ISSN 01466410. doi:10.1016/j.ppnp.2011.12.001. 1111.0507

[18] J. A. Formaggio et al. 'From eV to EeV: Neutrino Cross Sections Across Energy Scales'. Reviews of Modern Physics, volume 84(3):pp. 1307–1341, 2012. ISSN 0034-6861, 1539-0756. doi:10.1103/RevModPhys.84.1307. 1305.7513

[19] D. Groom. 'Critical energy for electrons and positrons'. https://pdg.lbl.gov/2022/AtomicNuclearProperties/critical_energy.html, 2021

[20] S. R. Klein et al. 'A measurement of the LPM effect'. In 'AIP Conference Proceedings', volume 302, (pp. 172–197). AIP, Ithaca, New York (USA), 1994. ISSN 0094243X. doi:10.1063/1.45475

[21] V. Baier et al. 'Concept of formation length in radiation theory'. Physics Reports, volume 409(5):pp. 261–359, 2005. ISSN 03701573. doi:10.1016/j.physrep.2004.11.003

[22] W. Lohmann et al. 'Energy loss of muons in the energy range 1-10000 GeV', 1985

[23] D. García-Fernández et al. 'The signatures of secondary leptons in radio-neutrino detectors in ice'. Physical Review D, volume 102(8):p. 083011, 2020. ISSN 2470-0010, 2470-0029. doi:10.1103/PhysRevD.102.083011. 2003.13442

[24] G. A. Askar'Yan. 'Excess negative charge of an electron-photon shower and its coherent radio emission'. 1961

[25] A. Albert et al. 'All-flavor Search for a Diffuse Flux of Cosmic Neutrinos with Nine Years of ANTARES Data'. The Astrophysical Journal Letters, volume 853(1):p. L7, 2018. ISSN 2041-8205. doi:10.3847/2041-8213/aaa4f6

[26] S. Adrián-Martínez et al. 'Letter of intent for KM3NeT 2.0'. Journal of Physics G: Nuclear and Particle Physics, volume 43(8):p. 084001, 2016. ISSN 0954-3899. doi:10.1088/0954-3899/43/8/084001

[27] M. Agostini et al. 'The Pacific Ocean Neutrino Experiment'. Nature Astronomy, volume 4(10):pp. 913–915, 2020. ISSN 2397-3366. doi:10.1038/s41550-020-1182-4. 2005.09493

[28] 'In Depth | Earth'. https://solarsystem.nasa.gov/planets/earth/in-depth

[29] 'Earth Fact Sheet'. https://nssdc.gsfc.nasa.gov/planetary/factsheet/earthfact.html

[30] C. Glaser. 'Results from the ARIANNA high-energy neutrino detector', 2023. doi: 10.48550/arXiv.2304.07179. 2304.07179

[31] A. Coleman. 'Wiki for the Greenland radio detector collaboration'

[32] J. A. Aguilar et al. 'Reconstructing the neutrino energy for in-ice radio detectors'. The European Physical Journal C, volume 82(2):p. 147, 2022. ISSN 1434-6044, 1434-6052. doi:10.1140/epjc/s10052-022-10034-4. 2107.02604

[33] N. Heyer. 'Wind Turbines Performance and Development', Presentation, 2022

[34] P. Allison et al. 'Design and Performance of an Interferometric Trigger Array for Radio Detection of High-Energy Neutrinos'. Nuclear Instruments and Methods in Physics Research Section A: Accelerators, Spectrometers, Detectors and Associated Equipment, volume 930:pp. 112–125, 2019. ISSN 01689002. doi:10.1016/j.nima.2019.01.067. 1809.04573

[35] S. Hallmann et al. 'Sensitivity studies for the IceCube-Gen2 radio array', 2021. 2107.08910

[36] C. Glaser et al. 'NuRadioMC: Simulating the radio emission of neutrinos from interaction to detector'. The European Physical Journal C, volume 80(2):p. 77, 2020. ISSN 1434-6044, 1434-6052. doi:10.1140/epjc/s10052-020-7612-8. 1906.01670

[37] C. Glaser et al. 'NuRadioReco: A reconstruction framework for radio neutrino detectors'. The European Physical Journal C, volume 79(6):p. 464, 2019. ISSN 1434-6044, 1434-6052. doi:10.1140/epjc/s10052-019-6971-5. 1903.07023

[38] J.-H. Koehne et al. 'PROPOSAL: A tool for propagation of charged leptons'. Computer Physics Communications, volume 184(9):pp. 2070–2090, 2013. ISSN 00104655. doi:10.1016/j.cpc.2013.04.001

[39] S. Hallmann. 'Proposal minimum shower energy', Presentation, 2021

[40] T. N. Group. 'Event Generation'. https://nu-radio.github.io/NuRadioMC/NuRadioMC/pages/Manuals/event_generation.html, 2023

[41] S. Hallmann et al. 'NuRadioMC Workshop Part 1: Installation, general usage examples & how to contribute', Presentation, 2022

[42] 'Antenna Models — NuRadio 2.2.0-dev documentation'. https://nu-radio.github.io/NuRadioMC/NuRadioReco/pages/detector/antennamodels.html

[43] 'Properties of Detector Description — NuRadio 2.2.0-dev documentation'. https://nu-radio.github.io/NuRadioMC/NuRadioReco/pages/detector/detector_database_fields.html

[44] R. L. Hawley et al. 'Rapid techniques for determining annual accumulation applied at Summit, Greenland'. Journal of Glaciology, volume 54(188):pp. 839–845, 2008. ISSN 0022-1430, 1727-5652. doi:10.3189/002214308787779951

[45] J. Avva et al. 'An in situ measurement of the radio-frequency attenuation in ice at Summit Station, Greenland'. Journal of Glaciology, volume 61(229):pp. 1005–1011, 2015. ISSN 0022-1430, 1727-5652. doi:10.3189/2015JoG15J057

[46] T. N. Group. 'NuRadioMC.utilities.attenuation module'. https://nu-radio.github.io/NuRadioMC/NuRadioMC/apidoc/NuRadioMC.utilities.attenuation.html#NuRadioMC.utilities.attenuation.fit_GL1, Code Documentation, 2023

[47] T. N. Group. 'Signal Propagation '. https://nu-radio.github.io/NuRadioMC/NuRadioMC/pages/Manuals/signal_propagation.html#propagation-module, Manual, 2023

[48] MIT Department of Physics. 'Ohnson Noise and Shot Noise: The Determination of the Boltzmann Constant, Absolute Zero Temperature and the Charge of the Electron', 2013

[49] R. Lahmann. 'Data acquisition and digital processing of analog signals', Lecture, 2023

[50] A. A. Kochanov et al. 'Energy loss of muons and taus through inelastic scattering on nuclei', 2005. hep-ph/0508306

[51] K. Terveer. Radio Propagation in Non-Homogenous Ice for Radio Neutrino Experiments. Master's thesis, 2022

[52] P. Virtanen et al. 'SciPy 1.0: Fundamental algorithms for scientific computing in Python'. Nature Methods, volume 17(3):pp. 261–272, 2020. ISSN 1548-7105. doi:10.1038/s41592-019-0686-2

[53] V. Blobel et al. Statistische und numerische Methoden der Datenanalyse. Teubner Studienbücher Physik. Vieweg+Teubner Verlag, Wiesbaden, 1998. ISBN 978-3-519-03243-4 978-3-663-05690-4. doi:10.1007/978-3-663-05690-4

[54] The NuRadio Group. 'Signal Generation (electric field)'. https://nu-radio.github.io/NuRadioMC/NuRadioMC/pages/Manuals/signal_generation.html, 2023

[55] T. Fawcett. 'An introduction to ROC analysis'. Pattern Recognition Letters, volume 27(8):pp. 861–874, 2006. ISSN 01678655. doi:10.1016/j.patrec.2005.10.010

[56] C. Welling et al. 'Reconstructing the cosmic-ray energy from the radio signal measured in one single station'. Journal of Cosmology and Astroparticle Physics, volume 2019(10):pp. 075–075, 2019. ISSN 1475-7516. doi:10.1088/1475-7516/2019/10/075. 1905.11185

[57] I. Plaisier. Reconstructing the Arrival Direction of Cosmic Neutrinos with the Radio Neutrino Observatory Greenland (RNO-G). Ph.D. thesis, 2022

[58] T. Cormen et al. Introduction To Algorithms. 3 edition, 2009

List of Figures

Statutory Declaration

I hereby declare that I have developed and written the enclosed Master's thesis completely by myself, and have not used sources or means without declaration in the text. Any thoughts from others or literal quotations are clearly marked. The Master's thesis was not used in the same or in a similar version to achieve an academic grading or is being published elsewhere.

Erlangen, July 27, 2023

Janna Zoe Vischer